Evaluation of Novel Metal-Organic Framework Materials for Adsorptive Post-Combustion CO_2 Capture

by

Johan Duane Baboolal

A thesis submitted in partial fulfillment of the requirements for the degree of

Master of Science

in

Chemical Engineering

Department of Chemical and Materials Engineering
University of Alberta

Abstract

The mitigation of CO_2 emissions from large anthropogenic sources such as coal-fired power plants by CO_2 capture is a challenging engineering problem. Due to the large scale of energy generation, post-combustion CO_2 capture processes must be very low-cost for practical implementation. The current industry standard technology for CO_2 capture, absorption, separates CO_2 from post-combustion flue gas by scrubbing with a liquid amine solvent, and is very energy intensive. Pressure swing adsorption (PSA) uses a porous, solid adsorbent material to separate CO_2 and N_2, and is a potentially lower energy alternative to absorption, due to the regeneration simply requiring a reduction in pressure.

The benchmark or standard adsorbent which has been considered and evaluated in literature for post-combustion CO_2 capture is zeolite 13X. Recently, several novel metal-organic framework (MOF) materials have been reported in literature to have potential as alternatives to zeolite 13X, however evaluation of these MOFs in a PSA process has not been done. This research will be focused on the evaluation of two types of MOFs in a PSA process using simulated flue gas as a feed, and comparing their performance to zeolite 13X.

The first type of MOF evaluated, called SiF_6 or SIFSIX, was reported in literature to not be significantly affected by the presence of water. Zeolite 13X, however, has a significantly reduced CO_2 capacity when water vapor is present in flue gas. Two types of SIFSIX materials were investigated, SIFSIX-2-Cu-i and SIFSIX-3-Zn. The experimental adsorption isotherms of these materials were fitted to a Langmuir model, and this was incorporated into a full PSA model. Optimization of the SIFSIX adsorbents and zeolite 13X under feed of 15% CO_2 and 85% N_2 showed that both SIFSIX adsorbents have similar purity and recovery performance when compared to 13X. An energy and productivity analysis was also performed, and SIFSIX-2-Cu-i had a similar energy requirement compared to Zeolite 13X, with a minimum energy of 155 kWh/t CO_2 captured. The minimum energy for SIFSIX-3-Zn was 140 kWh/t CO_2, however the very sharp isotherm of SIFSIX-3-Zn results in a productivity of 0.18 mol/m^3 adsorbent/s, which is significantly lower than that for 13X, at 0.42 mol/m^3 adsorbent/s and SIFSIX-2-Cu-i at 0.75 mol/m^3 adsorbent/s. These

results indicate that in a dry case, Zeolite 13X is a better adsorbent than SIFSIX-3-Zn, and SIFSIX-2-Cu-i has performance which is only marginably better.

The second type of MOF evaluated for post-combustion capture is a diamine-appended MOF, mmen-Fe_2. This type of adsorbent was reported in the literature to have an S shaped or type V adsorption isotherm. A quadratic-langmuir isotherm model was employed to fit the adsorption isotherm of mmen-Fe_2 at a temperature of $30°C$. The performance of mmen-Fe_2 and Zeolite 13X was then compared by an optimization study, which revealed that the minimum energy for the mmen-Fe_2 adsorbent was 110kWh/t CO_2, compared to that of 13X which was 135 kWh/t CO_2. The reduction in energy was due to a higher blowdown pressure being possible in the mmen-Fe_2 adsorbent due to its capacity for N_2 being significantly less than Zeolite 13X. The S-shaped CO_2 isotherm was also beneficial, as the increased working capacity of CO_2 resulted in a productivity for mmen-Fe_2 which was 1 mol/m^3 adsorbent/s, almost twice that of Zeolite 13X, at 0.55 mol/m^3 adsorbent/s. Therefore, the mmen-Fe_2 adsorbent is a good candidate for CO_2 capture by VSA considering its better performance than zeolite 13X in terms of both energy and productivity.

Acknowledgements

In this section, I would like to acknowledge the many people who have contributed to the various aspects of this research project. My supervisor, Dr. Arvind Rajendran, for his advice and guidance throughout the 2 year duration of this project. The support provided by him regarding various problems in the project were invaluable, and without his input this would not have been possible. I would also like to thank Dr. Dave Sharp, who contributed his time and efforts towards our weekly discussions. Additionally, many thanks are extended to the present and former members research group at the Laboratory for Advanced Separation Processes at the University of Alberta. The discussions we had were very important in many aspects of this work.I am also very grateful to my family, for their patience, emotional support and encouragement through the years. This project is funded by NSERC discovery grant.

Contents

List of Tables

List of Figures

Chapter 1

Introduction

1.1 Greenhouse Gases and Environmental Regulations

The greenhouse effect is a naturally occurring phenomenon whereby certain gases absorb infrared radiation from the sun, effectively trapping a portion of the irradiated heat in the earth's atmosphere. These gases are called greenhouse gases (GHGs) include CO_2, H_2O, CH_4, NO_x and ozone. Since the dawn of the industrial era, anthropogenic CO_2 emissions have increased drastically, raising concerns of global warming due to enhanced greenhouse effect. This trend is clear based on the data in Figure 1.1, which shows a very sharp increase in the CO_2 atmospheric concentration from the year 1900 onwards. This time period coincides with the increased usage of fossil fuels as the primary source of energy, which releases CO_2 into the atmosphere. Climate change is one of the potential long-term effects of increased concentrations of greenhouse gases, primarily CO_2, in the earth's atmosphere.

There are several options available for mitigating CO_2 emissions, from using renewable energy sources to switching to fossil fuels that produce less CO_2 such as natural gas. Carbon capture and storage (CCS) is one such technique for the reduction of GHG emissions which can be implemented alongside the usage of traditional fossil fuel energy sources such as coal which are still necessary in order to meet global energy demands. A CCS schematic is shown in Figure 1.2 [2] , which consists of capture from the point source, pressurization and transport of CO_2, and finally storage of the pressurized CO_2 in geological formations or the ocean.

The primary challenges in designing CO_2 capture processes are the scale of emissions and the energy cost associated with the separation of CO_2 from flue gas. In the overall scheme of CO_2 capture and sequestration, the estimated energy cost related to CO_2 capture is the most expensive at 60-70%, followed by compression at 20% with transportation accounting

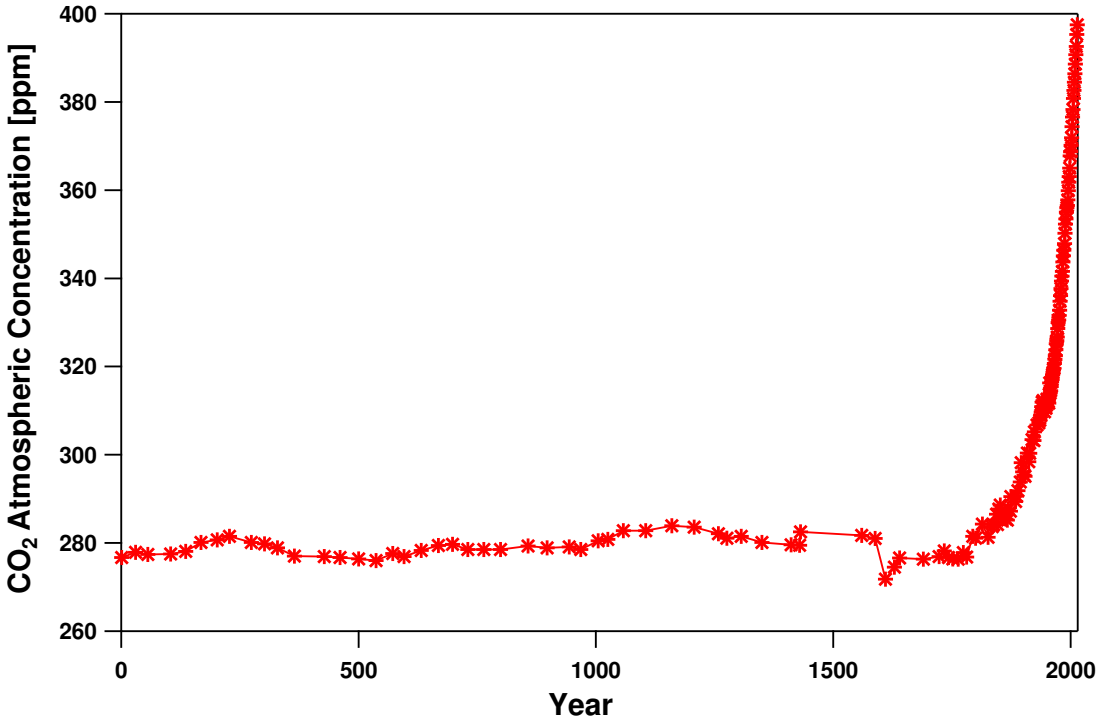

Figure 1.1: Average Atmospheric CO_2 Concentration per year [1]

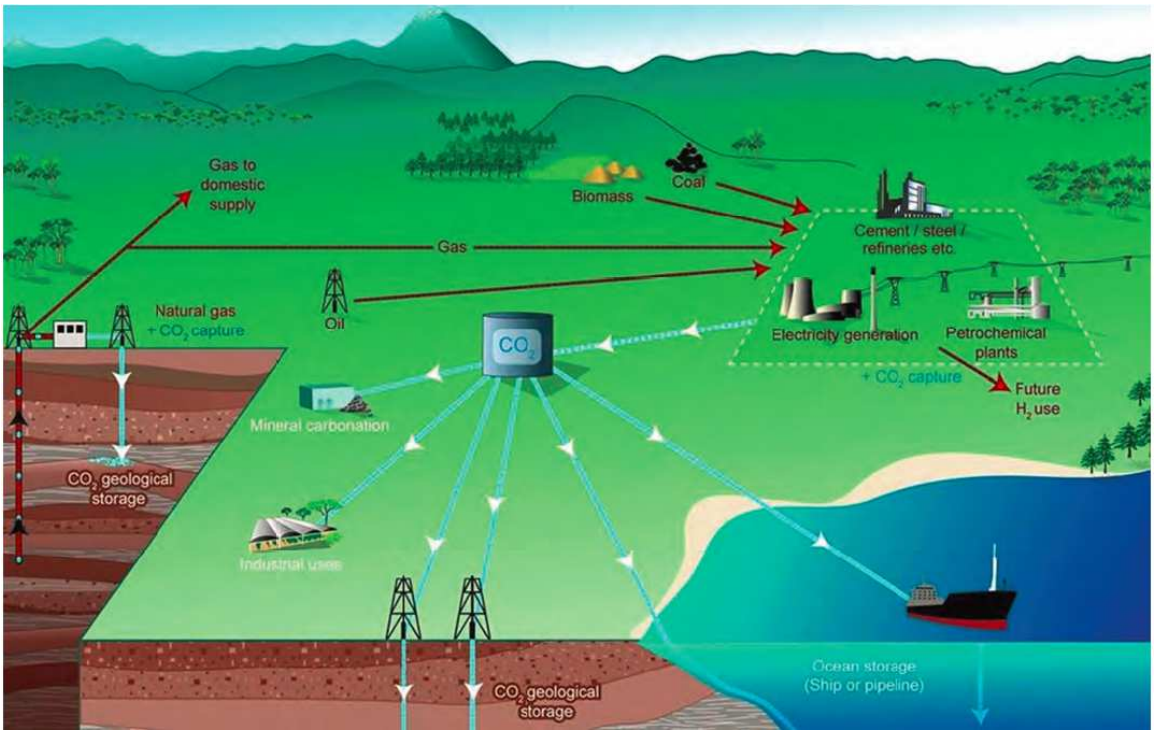

Figure 1.2: Schematic of Carbon Capture and Storage (CCS) [2]

for the remaining costs [11]. Therefore, focusing on reducing the costs directly related to CO_2 capture technology is the most effective way of reducing overall CCS costs on the large scale that is required.

1.2 Carbon capture Technologies

There are three main types of CO_2 capture processes, classified depending on the type of power plant and energy source: pre-combustion, post-combustion and oxyfuel capture. A block diagram of pre-combustion capture is shown in Figure 1.3. Usually, coal is gasified by heating to high temperatures in limited oxygen to form syngas, which is primarily composed of CO and H_2. After gasification the syngas undergoes a water-gas shift reaction where CO is reacted with water vapour in the presence of a catalyst to form CO_2 and H_2. The molar compositions of CO_2 and H_2 coming out of the water-gas shift reaction are 40% and 60% respectively. The main advantage of pre-combustion capture is the elevated CO_2 composition compared to post-combustion flue gas, making the separation much easier. The disadvantage is that the hydrogen fuel cell is not economically viable for large-scale power generation so the CO_2 capture potential is limited to smaller scale operations [12].

Post-combustion CO_2 capture processes are applied to traditional fossil fuel power plants in which the fuel is burnt in the presence of air to produce steam which is used to drive gas turbines, as illustrated in Figure 1.3. The flue gas from a coal-fired power plant, for instance, is sent through a flue gas desulphurisation (FGD) unit, which removes SO_x and NO_x gases, and cools the flue gas stream. The output of the FGD process is the feed stream to the carbon capture process, which is composed of roughly 3-4% H_2O, 12-15% CO_2 and the 80-85% N_2 at atmospheric pressure and 25°C. The obvious advantage to post-combustion capture is that power plants can be retrofitted with the additional process equipment. However, due to the low CO_2 partial pressure of 10-15 kPa, there is the additional challenge of the separation itself compared to pre-combustion capture as well as minimizing the separation energy costs on a large scale.

The oxyfuel combustion process is shown in Figure 1.3. The fuel is burnt in concentrated (95% pure) oxygen, which results in flue gases primarily composed of CO_2 and water vapour, with concentrations of CO_2 of around 80% by volume [12]. The advantage to oxyfuel carbon dioxide capture is that the resulting flue gas is a mixture of CO_2 and water vapour, meaning that elaborate carbon capture processes are not necessary depending on the oxyfuel process. The drawback however is that the separation of O_2 from air, which is usually done by cryogenic processes, incurs a large energy cost.

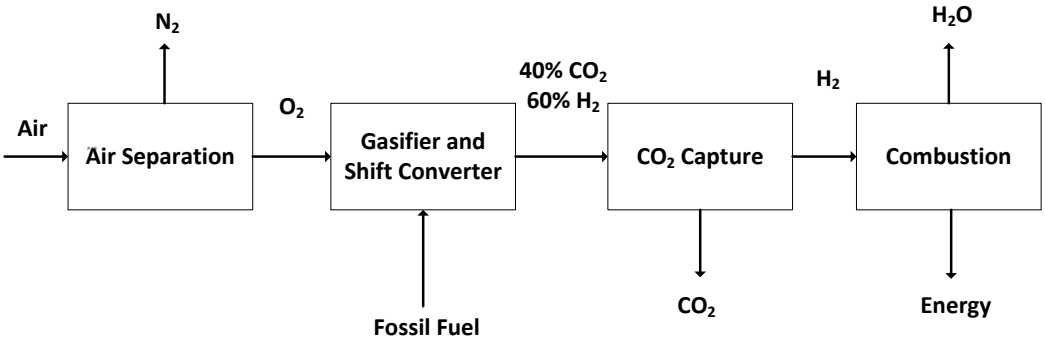

(a)

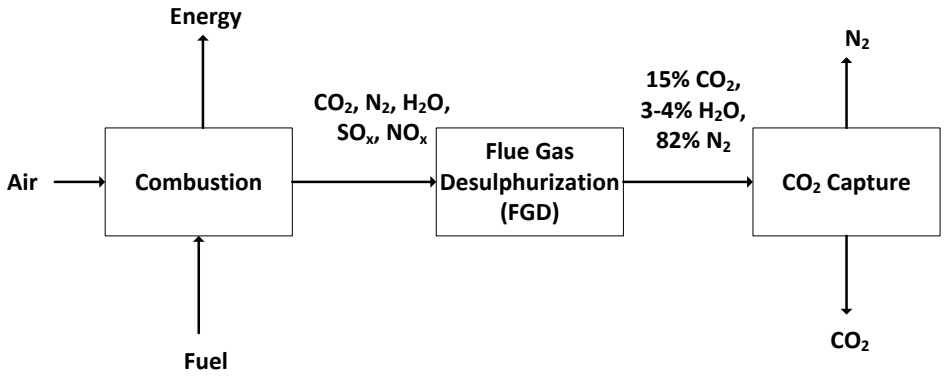

(b)

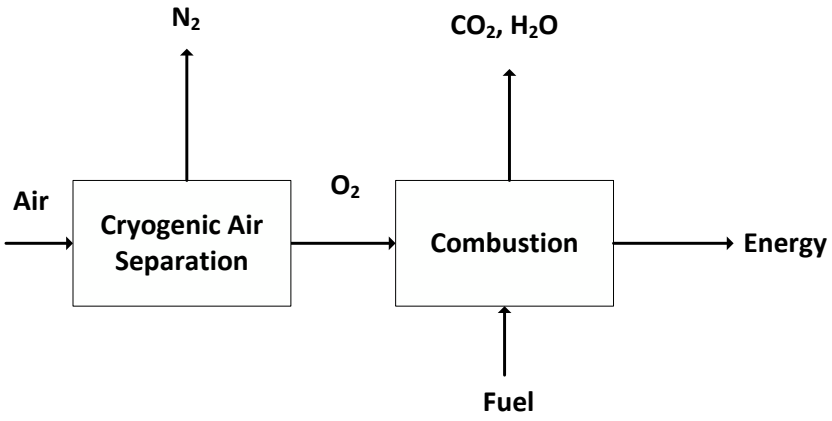

(c)

Figure 1.3: Schematic overview of carbon capture processes for a.) Pre-combustion, b.)Post-combustion and c.)Oxyfuel capture

This research is focused on post-combustion CO_2 capture from coal-fired power plants, due to power generation being one of the largest sources of anthropogenic CO_2 emissions [11].

The basis is a 500MW power plant emitting 10,000 tonnes of CO_2 per day. The flue gas is considered to be composed of 15% CO_2 and 85% N_2 by volume. The CO_2 capture process should have a CO_2 product purity and recovery $\geq 90\%$, in compliance with U.S. Department of Energy targets for carbon capture technology [13].

There are several options for post-combustion CO_2 capture which are currently in development and/or being used in commercial applications. Table 1.1 lists and summarizes the current status of these technologies.

Table 1.1: Status of Current Carbon Capture Technologies

Separation Process	**Status**
Absorption	Mature technology. Standard commercial choice for CO_2 capture currently. Expensive regeneration costs, degradation of scrubbing solvent.
Adsorption	Commercially used for natural gas sweetening and H_2 production. Post-combustion capture on pilot scale <2t CO_2/day [14].
Membrane	Used for natural gas sweetening commercially. Post-combustion still under development, 1t CO_2/day. [14]
Chemical Looping	Excellent performance for gaseous fossil fuels. 100% CO_2 capture possible. Under development for coal as energy source.

1.2.1 Membrane

Commercial gas separation processes using polymeric membranes exploits the selective permeability of the membrane by allowing certain gas molecules to freely pass through, while preventing others. Membranes therefore selectively separate gas mixtures based on the size and relative diffusivities of the component species. In terms of CO_2 capture applications, several polymeric membranes which selectively separate CO_2 over H_2 and N_2 have been manufactured. One disadvantage is that prolonged and continuous exposure to CO_2 and other gases causes permanent changes in morphology, which negatively impacts the performance of the membrane assembly [15].

1.2.2 Chemical Looping

Chemical looping is an emerging technology for CO_2 capture, which inherently separates CO_2 from N_2 during energy generation. A schematic of chemical looping combustion is given in Figure 1.4 . Chemical looping circumvents the direct contact between the fuel and

combustion air by using an oxygen carrier - a metal oxide. This metal oxide is oxidized in the air reactor as in Equation (1.1), and undergoes a combustion reaction in the fuel reactor, as in Equation (1.2). Chemical looping results in separate streams of N_2 and CO_2, meaning the only separation required is that of carbon dioxide and water vapour.

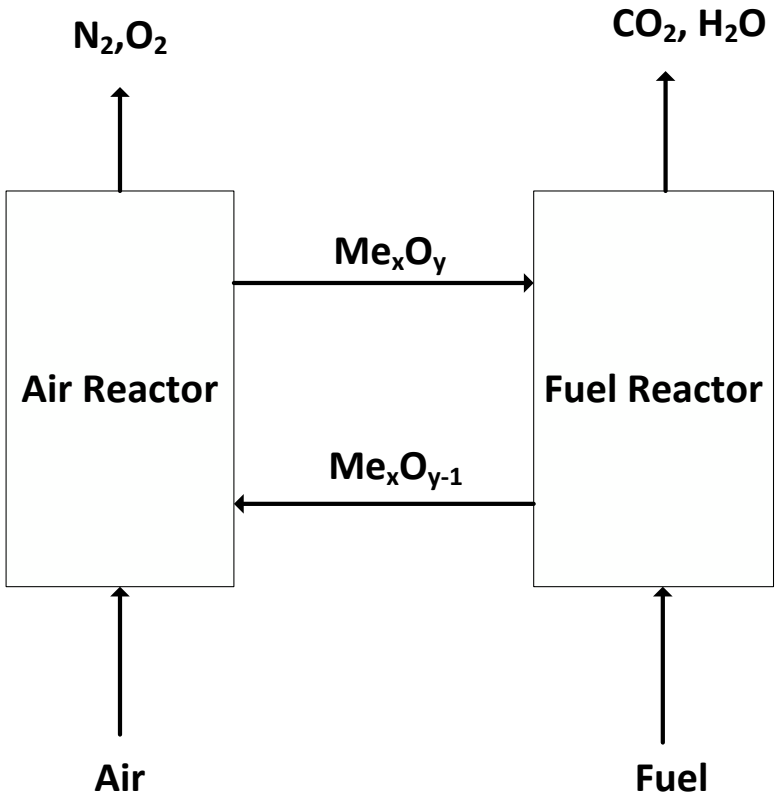

Figure 1.4: Block Diagram Schematic of a Chemical Looping Process

$$Me_xO_{y-1} + \frac{1}{2}O_2 \longrightarrow Me_xO_y \tag{1.1}$$

$$(2n+m)Me_xO_y + C_nH_{2m} \longrightarrow (2n+m)Me_xO_{y-1} + mH_2O + nCO_2 \tag{1.2}$$

In terms of performance, chemical looping can recover 100% of the CO_2 generated in the fuel reactor with $\geq$ 99% fuel conversion [14]. This performance applies to gaseous fossil fuels such as natural gas. For solid fuels such as coal, no such high performance is recorded due to additional design being required for proper contact between the metal oxide and the coal mass. Furthermore, fouling and degradation of the metal oxide occurs when solid fuel is used due to the formation and subsequent deposition of ash. The advantage of chemical

looping is that no additional gas separation equipment is required for the removal of CO_2, and H_2O can be easily separated by condensation. Therefore, this form of carbon capture for gaseous fuel has very low energy requirements and is relatively low cost, depending on the cost of the metal oxide and how often it must be replaced. For solid fuel, chemical looping is still in the research and development phase [14].

1.2.3 Absorption

Absorption is the mature and current preferred technology used in the chemical industry for the purpose of CO_2 removal. Examples of this include the removal of CO_2 from CH_4 in the sweetening of natural gas and ammonia manufacturing processes. The absorbent used in these cases is usually an alkanol amine compound such as monoethanolamine (MEA) [15]. The liquid absorbent is reacted with CO_2 in a scrubbing column, then pumped to a second column for thermal regeneration.

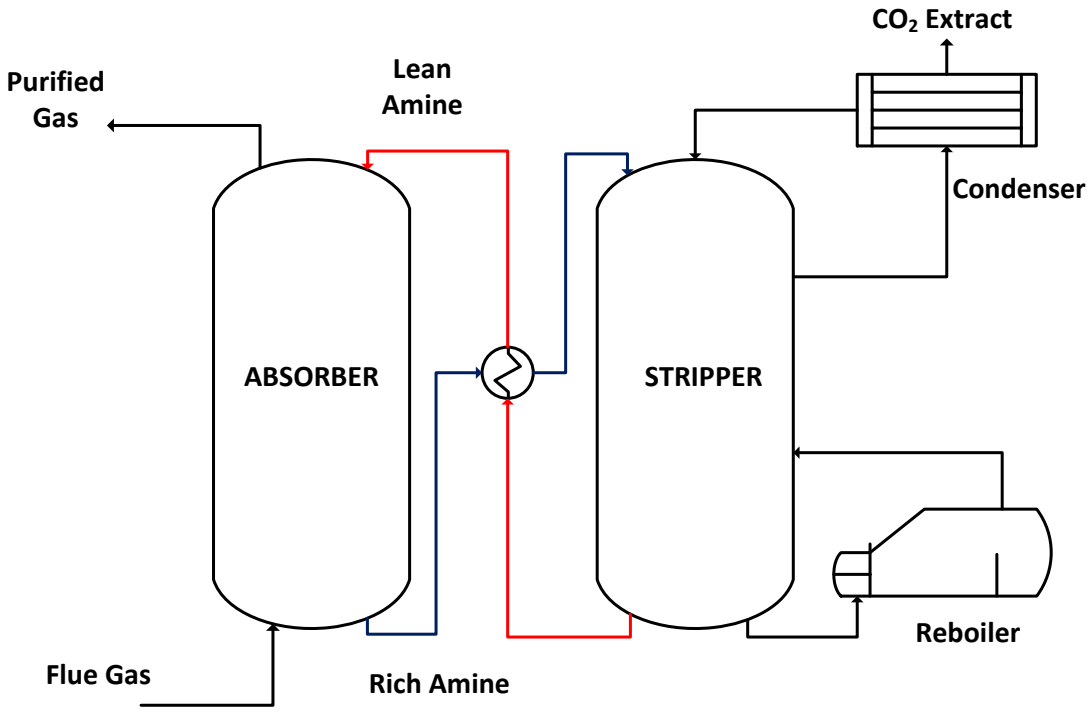

Figure 1.5: Schematic diagram of an absorption process using MEA solvent. The blue lines indicate CO_2 rich amine solvent, and the red lines indicate CO_2 lean solvent.

The advantages of absorptive scrubbing in CO_2 capture are that purity and recovery in excess of 90% are attainable, and heat integration with the power plant can be facilitated easily as steam can be used for the thermal regeneration of the scrubbing solvent. However,

there are several major drawbacks to absorptive CO_2 processes that prevent their usage for post-combustion CO_2 capture. The absorbent is recovered by heating to temperatures of 120°C, which comes with a high energy cost per tonne of CO_2 captured. Many of the amine solvents, primarily MEA, react irreversibly with CO_2, COS and CS_2 resulting in several chemical products causing slow degradation of the amine over many continuous absorption and regeneration cycles. The energy of regeneration is reported in literature to be 2-4 MJ/kg CO_2 captured [11], though this will change based on the specifics of the process and the scrubbing solvent used. This corresponds to a power plant energy penalty of 25-30% which is not economically viable for large scale CO_2 separation from post-combustion flue gas.

1.2.4 Adsorption

Adsorption, is a mass transfer phenomena whereby gaseous molecules, adsorbates, become bound to the surface of a porous solid adsorbent. The type of adsorption is determined by the strength and type of adsorbate-adsorbent bond. Physisorption is usually characterized by weaker van der Waal's interactions between the gas molecules and solid surface. Chemisorption involves stronger covalent bonds between sorbate and sorbent and is usually associted with high energy. CO_2 capture works on the basic principle that CO_2 is selectively adsorbed over the N_2, the most common component of flue gas. Therefore, for an adsorptive post-combustion process to be successful, the adsorbent must have the properties of:High CO_2 capacity;High CO_2 selectivity over N_2.

Gas separation by adsorption occurs by several different mechanisms [16]. The steric or molecular sieve mechanism is separation where certain gas molecules can diffuse into the pores and others are excluded by their size, shape or a combination of both. Kinetic separation is another adsorption mechanism which achieves separation due to the different diffusion rates of species in mixture. The dominant separation mechanism exploited in the majority of adsorptive processes is theromodynamic equilibrium effects. This refer to adsorption by molecular interactions between the adsorbate and the adsorbent.

The type of adsorptive process can be classified based on the method in which the adsorption and regeneration is done. Pressure swing adsorption (PSA) works based on the principle that if a bulk gas mixture is in equilibrium with the solid or adsorbed phase at higher pressure, more of the strongly adsorbed component will be present in the solid phase. The less strongly adsorbed component will break through the adsorption column since it is less likely to bind to active sites on the adsorbent surface. Reducing the pressure then causes

the more strongly adsorbed component to be released from the adsorbent surface and back into the bulk gas phase to be removed. Adsorption and desorption can then be cycled in a pressure swing process in order to separate gas mixtures, namely CO_2 and N_2 in this case. Pressure swing adsorption is defined as an adsorption process in which the adsorption pressure is higher than atmospheric pressure and the desorption pressure is atmospheric or higher. Vacuum swing adsorption (VSA) is a pressure swing adsorption process where the adsorption pressure is at 1 atmosphere and the desorption pressure is at sub-atmospheric pressure levels. Pressure vacuum swing adsorption (PVSA) is a pressure swing where the adsorption pressure is greater than atmospheric pressure and the desorption pressure is at vacuum levels.

Temperature swing adsorption (TSA) works based on the principle that equilibrium loadings of different adsorbate species are higher at lower temperatures and vice versa. Therefore a TSA process will consist of an adsorption step at a low temperature, followed by a desorption step at a higher temperature. The reason for this is that at lower temperatures, more active sites are available on the adsorbent surface for binding than at higher temperatures. The deciding criterion in whether PSA or TSA cycles are used in the context of this study is the cycle time. In TSA, working capacities are larger dependent on $\triangle T$ between the adsorption and desorption temperatures, but the drawback is that the cycle time is limited by the rate of heat transfer throughout the bed. PSA cycles only depend on the pressure in the bed which is much more rapidly changed for a variety of adsorbents and the rate of change of bed pressure usually doesn't depend on the bed dimensions or specific heat capacity of the adsorbent as is the case with TSA.

The current status of PSA is that it is not as widely implemented for gas separations as absorption. It is currently a mature technology for light product separations, such as air purification. Adsorptive CO_2 capture processes by PSA/VSA show great promise due to the heat of adsorption being of the order of 40kJ/mol adsorbent captured, meaning that theoretically the energy required to regenerate the adsorbent should be much less than that of the industry-standard technique of absorption. This has positive implications for both capital and operating costs of retrofitting coal-fired power plants with adsorption-based CO_2 capture processes.

1.3 Outline and Scope of Thesis

The objective of this study is the evaluation of novel adsorbents for the purpose of post-combustion CO_2 capture by PSA. The performance of these adsorbents will be compared

to that of a benchmark adsorbent, Zeolite 13X. The process must have CO_2 product purity and recovery in excess of 90%, with the constraint of minimizing the energy penalty in extracting 1 tonne of CO_2, while maximizing productivity, defined as the mass of CO_2 which can be captured per m^3 adsorbent per day. Chapter 2 of this thesis focuses on the previous contributions in post-combustion PSA. It will cover the properties of different classes of adsorbents, namely their physical properties and adsorption equilibrium data for CO_2 and N_2. This chapter will also cover an overview of PSA cycle configurations, as well as the reported performance of these configurations in literature, both experimentally and in simulations. Chapter 3 is primarily focused on the development and modeling of PSA cycles in this study,i.e., going from modeling adsorption equilibrium data via isotherms to a full non-isothermal, non-isobaric PSA model that captures the column dynamics. This chapter will also cover the methodology of the multiobjective optimization done in this research project. In Chapter 4, the performance of two novel metal organic framework (MOF) adsorbents will be evaluated. This chapter covers the extraction of experimental data from literature for both CO_2 and N_2 and modeling of the adsorption isotherms. Using this data, the adsorbents are optimized and compared to Zeolite 13X in terms of their process performance. Chapter 5 is a similar evaluation of the performance of another metal organic framework for post-combustion CO_2 capture. Experimentally determined isotherms for this family of MOFs have 'S' shaped or type V isotherms, which in principle have massive potential for CO_2 capture by VSA. The issue discussed in this chapter is the modeling and optimized performance of this MOF compared to the benchmark, Zeolite 13X. The main contributions, conclusions and recommendations for further study are summarized in chapter 6.

Chapter 2

Literature Review

This chapter will cover the major aspects of adsorptive post-combustion CO_2 capture in literature. In the first part of this chapter, different classes of adsorbents considered for CO_2 capture will be reviewed, their basic properties discussed and the adsorption isotherms of CO_2 and N_2 presented, where available. The second part of the chapter will deal with the PSA cycles previously used in literature for post-combustion CO_2 capture, descriptions of the steps in these cycles and summarizing their performance.

2.1 Adsorbents used for Post-combustion CO2 Capture

2.1.1 Zeolites

Zeolites are porous, crystalline aluminosilicates with tetrahedral unit cells. That is, SiO_4 and AlO_4 tetrahedra are regularly arranged with bridging oxygen atoms to form the crystal structure. The negatively charged aluminium atoms in the zeolite framework allow for the addition of metal cations at the surface [17, 18]. These metal cations then act as the active sites for the selective adsorption of gas molecules, such as CO_2. The ratio of Si/Al in the zeolite framework then becomes important, with more Si making the zeolite more thermally and mechanically stable and more Al increasing the number of active sites. For the purpose of adsorption this ratio is slightly above 1 [17]. Zeolite 13X is mechanically stable at the operating temperature and pressure range of post-combustion CO_2 capture. The pore size or diameter of this class of adsorbent is uniform and ranges from 3-10Å, with zeolite 13X at 7.5Å [19]. The main components of flue gas, N_2,CO_2 and H_2O, have sizes of 3.8Å, 3.4Å and 2.75Å respectively, meaning that all of these species can enter the pores of Zeolite 13X particles and adsorb onto the surface.

The single component adsorption isotherms of CO_2 and N_2 are shown in Figure 2.1. The experimental adsorption equilibrium data was extracted from Cavenati et al [3]. These

isotherms of carbon dioxide and nitrogen on 13X were obtained gravimetrically, carrying out adsorption in a magnetic suspension microbalance with each of the pure gases at temperatures of 25, 35 and 50°C. Each data point on the isotherm represents the equilibrium loading, which is the moles of CO_2 or N_2 adsorbed per gram of adsorbent, at a specific pressure and temperature. In the case of 13X, it can be observed that the loading of CO_2 is an order of magnitude higher than the loading of N_2 which indicates a high selectivity. The selectivity of two arbitrary components, A and B is defined as in Equation 2.1, with x_i representing the mole fraction of the component in the solid phase and y_i the mole fraction in the gas phase.

$$S_{A/B} = \frac{x_A y_B}{x_B y_A} \tag{2.1}$$

Generally, the higher the selectivity of one component over another in binary adsorption, the easier the separation can be done. Furthermore, the isosteric heat of adsorption for carbon dioxide and nitrogen was estimated to be 37.2 kJ/mol and 12.7 kJ/mol respectively in the low coverage region of the isotherm [3]. This low coverage region of the isotherm, also called the Henry region is the low pressure-low loading region of the isotherm where it is approximately linear. The relatively high heat of adsorption of carbon dioxide shows the strength of its interaction with 13X is stronger than nitrogen.

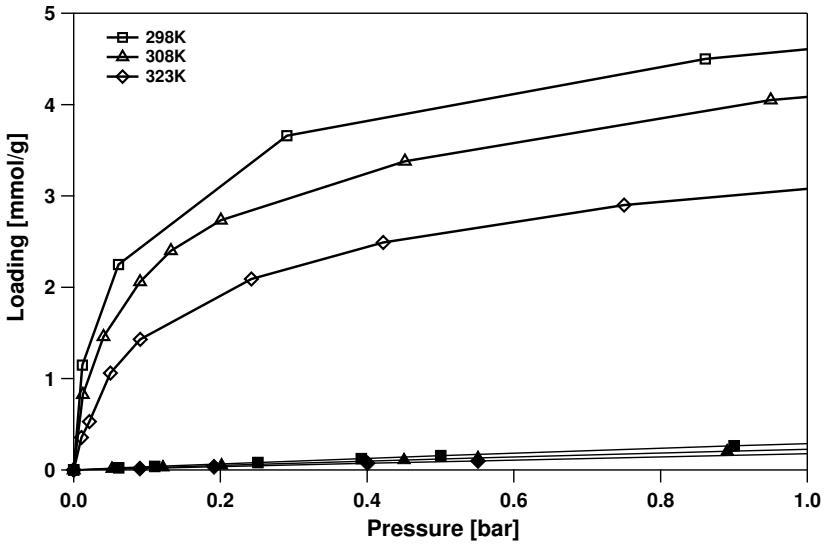

Figure 2.1: Experimental adsorption isotherms of CO_2 and N_2 on Zeolite 13X. Open symbols represent CO_2 isotherms and closed symbols represent N_2 isotherms. Markers represent the experimental adsorption isotherm data and lines are guides for the eyes. [3]

Zeolite 13X has been a benchmark adsorbent for CO_2 capture, due to its ease of man-

ufacture, low cost, mechanical stability and high selectivity for CO_2 in the atmospheric to sub-atmospheric pressure range required for vacuum swing adsorption. The disadvantage is that regeneration requires low vacuum pressures, which comes with an energy cost. Furthermore, 13X has significantly reduced CO_2 capacity in moist conditions [20].

2.1.2 Activated Carbon

Activated carbons are microporous or mesoporous adsorbents, which may be manufactured from coal, wood, byproducts from industry or other sources of biomass [21]. Unlike Zeolites, the pore size of activated carbons varies in the range of 3-100Å. The pore size distribution for a specific activated carbon adsorbent depends on the source of the carbon as well as the method used to produce the adsorbent. The preparation of activated carbon involves two steps - carbonization and activation. In carbonization the raw material undergoes pyrolysis at a temperature of 700-1100°C to form char, after which it is physically or chemically activated which alters the pore size [18]. The surface of activated carbon adsorbent consists of hydrophobic and hydrophilic active sites [4]. CO_2 can bind to both the hydrophobic and hydrophilic active sites, however water vapour can only bind on to the hydrophilic sites. This means that water does not affect the CO_2 adsorption capacity onto activated carbon as much as with zeolites.

Experimental adsorption isotherms of CO_2 and N_2 in the temperature range of 20 to 60°C on activated carbon are given on Figure 2.2. The adsorbent was activated at 350°C at low vacuum to ensure that the adsorbent was clean before the adsorption isotherm measurements. The adsorption isotherms of carbon dioxide and nitrogen were then measured using a volumetric method [4]. While CO_2 is more strongly adsorbed than N_2, a qualitative comparison between this isotherm and the same for Zeolite 13X shows that the loading of CO_2 at 15kPa is about half of that for 13X while the N_2 loading is approximately similar. This means that the selectivity of activated carbon is much less than that for 13X.

The advantage of activated carbon as an adsorbent is the low cost of raw materials. Activated carbons are also more tolerant to humid feed to a PSA or TSA process. The main disadvantage of activated carbon is the very low CO_2/N_2 selectivity [4,18], which results in worse absolute CO_2 capture performance in a VSA process [4].

2.1.3 Metal Organic Frameworks (MOFs)

Metal-organic frameworks are a relatively new class of adsorbents being synthesized for the purpose of CO_2 capture. In general, MOFs are composed of three-dimensional organic-

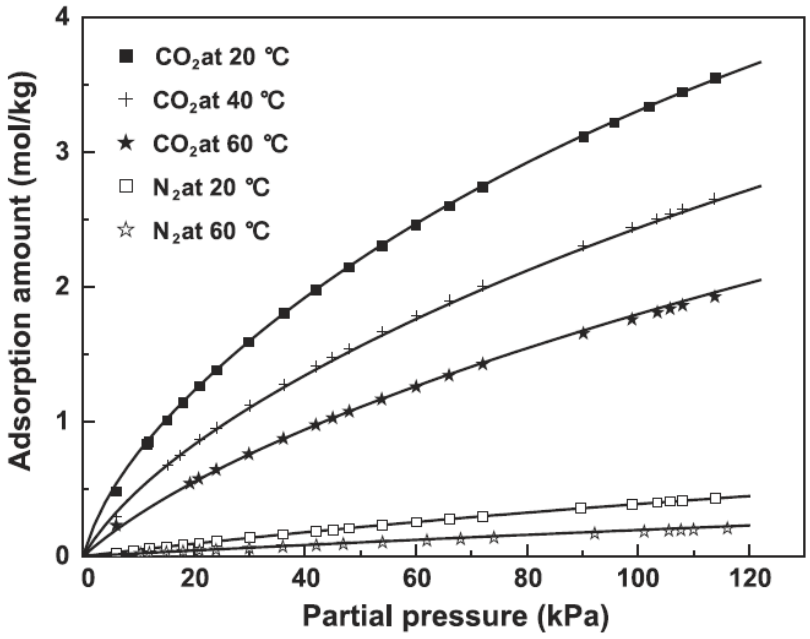

Figure 2.2: Experimental adsorption isotherms of CO_2 and N_2 on Activated Carbon, reproduced from Xu et al. [4].Reprinted by permission from Elsevier Ltd: Chemical Engineering Journal, [4],Copyright 2013

inorganic networks of metal-ligand bonds. In the structure of these adsorbents, the metal ions are bridged by organic ligands by coordination bonds [19]. One key feature of metal-organic frameworks is that they can be designed by careful selection of the metal and organic linkers that comprise the crystal structure, unlike tetrahedral silicates such as Zeolites which are limited to SiO_2 and AlO_2. This feature results in properties of the metal-organic frameworks such as pore size being easily tunable. As a result, thousands of MOFs have been synthesized, of which hundreds have been tested for their adsorption capacity [19]. However, there are limited pilot-scale post-combustion VSA processes in literature which have evaluated the performance of these MOFs in a cycle.

Several metal-organic frameworks have shown promising characteristics for post-combustion CO_2 capture, such as retention of CO_2 adsorption capacity and mechanical strength in the presence of water vapour [5]. McDonald et al have shown experimental isotherm data for several MOFs with S-shaped isotherms for CO_2 [6, 22]. These S-shaped isotherms display a very sharp increase in CO_2 loading at a threshold or step pressure. Some of the isotherms presented display this step change within the post-combustion range of CO_2 partial pressures, indicating tremendous potential for low-energy VSA separations. The adsorption isotherms of a several MOFs are illustrated in Figure 2.3.

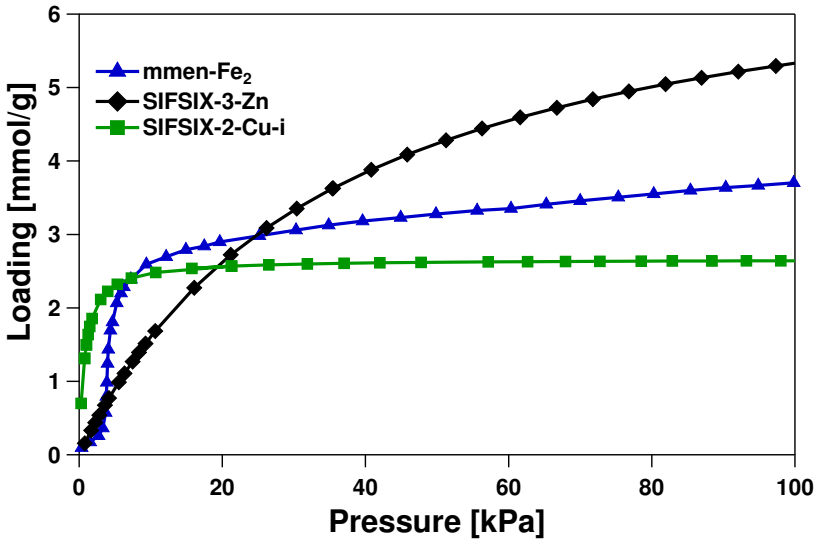

Figure 2.3: Experimental adsorption isotherms of CO_2 on SiF_6 and Diamine appended metal-organic frameworks at 25°C [5, 6]

The disadvantage to these MOFs is that they are still largely in the research and development phase meaning additional capital costs due to the cost of materials and manufacturing. In addition, publications of simulation or pilot-plant scale evaluation of these adsorbents in PSA/TSA cyclic processes are limited. Therefore, it is not known whether the process advantages of using certain MOFs for CO_2 capture offsets their increased cost compared to standard adsorbents such as Zeolite 13X.

2.2 Pressure Swing Adsorption Cycles

Gas separation by PSA involves the two basic steps of adsorption at high pressure and desorption at a low pressure. The difference between the strength of interaction of the different gas species and the adsorbent allows for certain gases to be selectively adsorbed and separated. The first basic PSA cycle was the 2-column, 4-step Skarstrom cycle, used to separate oxygen from nitrogen in air with Zeolite 5A as the adsorbent material [23]. This cycle is illustrated in Figure 2.4. The table provided in Figure 2.4 shows which of the valves are opened during the steps comprising the cycle. The four steps consisting this cycle are feed, blowdown, purge and pressurization. Air is fed into the adsorption column at higher than atmospheric pressure in the feed step. In this step, N_2 enters the solid phase and O_2 leaves through the outlet as a raffinate. In the next step, blowdown, the flow is reversed and part of the nitrogen is desorbed from the solid phase to the bulk gas phase by reducing the column to atmospheric pressure. The purge step removes more nitrogen by recycling some

of the purified air from the second column to maximise removal of nitrogen from the first column. In the final pressurization step, a feed stream of air is then used to re-pressurize the column to the high pressure at which the feed step is performed. Adsorption is an unsteady state process, however, the cycles are run until cyclic steady state (CSS) is reached, at which point the performance of each subsequent PSA cycle is constant [23]. The CSS is defined as the point at which all of the state variables of a particular step remains constant for all subsequent cycles.

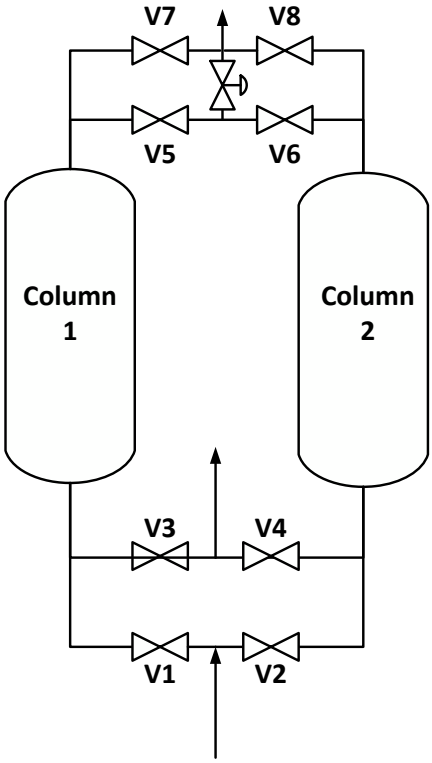

	Feed	Blow	Purge	Press
Column 1	V1,V7	V3	V5,V3	V1
	Purge	Press	Feed	Blow
Column 2	V6,V4	V2	V2,V8	V4

Figure 2.4: Skarstrom PSA Cycle

Since the development of the Skarstrom cycle, many improvements on the original Skarstrom PSA cycle configuration have been designed for a variety of gas separations. Several of these cycle configurations will be discussed in this section. Ko et al. performed a simulation study of a basic 4-step PSA and PVSA cycle using zeolite 13X as an adsorbent [7]. An illustration of the basic 4-step PVSA cycle can be found in Figure 2.5. The steps of the PVSA cycle in Figure 2.5a are (1) pressurization with feed gas at high pressure, (2) adsorption step with feed gas at high pressure, with N_2 as the weakly adsorbed component being collected at the outlet, (3) co-current blowdown, reducing pressure from high pressure to an intermediate pressure to maximize N_2 removal from the bed and (4) counter-current blowdown or evacu-

ation, where pressure is further reduced from the intermediate pressure to the low pressure, and CO_2 being the more strongly adsorbed component is desorbed and collected as the product from this step. The PSA cycle in Figure 2.5b is composed of (1) feed pressurization at high pressure (greater than 1 bar), (2) adsorption with feed gas at high pressure with N_2 being obtained at the column outlet, (3) depressurization via a counter-current blowdown step to approximately 1 bar in order to desorb and regenerate CO_2, collecting it at the bottom of the bed and (4) purge step using a counter-current flow of pure N_2 gas at 1 bar pressure, for the purpose of CO_2 regeneration. It is evident that in the PSA cycle, the purge step will result in reduced purity of the CO_2 product due to the introduction of pure N_2 to the column during the purge step. Ko et al. optimized the VPSA cycle and determined that a maximum CO_2 purity of 90% and recovery of 93.8% was attainable at a feed temperature of 97°C, a feed pressure of 6.82 bar, intermediate pressure of 0.7 bar and an evacuation pressure of 0.15 bar [7]. This PVSA cycle was not evaluated at lower temperatures in this particular study. The PSA cycle, however, was optimized at 50°C and gave maximum CO_2 purity of 56% and recovery of 97%, at a high pressure of 14 bar, and a purge pressure of 0.9 bar.

Wang et al. proposed a 2-stage PVSA cycle using zeolite 13XAPG for CO_2 capture from dry flue gas [8]. The proposed cycle is presented in Figure 2.6, consisting of a 3-bed, 5 step PSA cycle in the first stage which concentrates the CO_2 from the feed concentration at 15% to 60%. The second stage, which runs in series with the first, is a 2-bed 6-step cycle. This second stage uses the 60% concentrated CO_2 stream from the first stage as a feed and concentrates the CO_2 up to a final purity of over 95%. The first stage is composed of five steps. Pressurization with feed gas is the first step, followed by a feed or adsorption step in which CO_2 is adsorbed preferentially. The rinse step follows, in which part of the heavy product is recycled to the bottom end of the column, which causes the N_2 front to be pushed to the outlet end of the column. A counter-current blowdown step follows, in which the outlet end of the column is shut and the pressure is reduced, allowing CO_2 to be partially desorbed as an extract stream. This is followed by a purge step in which a portion of the light product from the feed step is used to push the CO_2 front further towards the inlet end of the column. This step will maximize the recovery of CO_2 at the expense of purity. The second stage is a two-bed, six step VSA cycle, consisting of the steps of feed pressurization, adsorption/feed, pressure equalization, blowdown and purge. The purpose of the pressure equalization steps are to reduce the energy required in reducing the pressure from that at the feed/adsorption step to that at the blowdown step. It should be noted

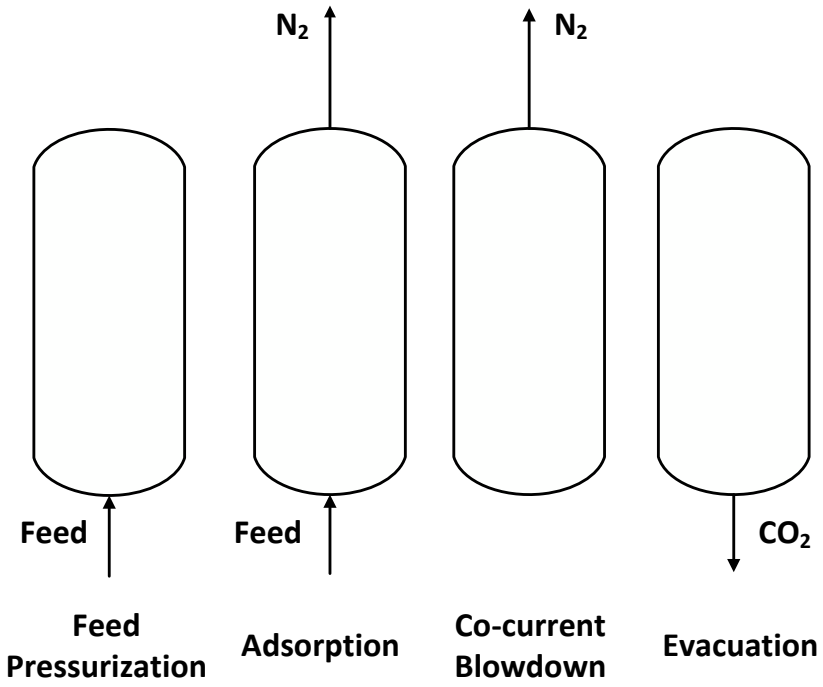

(a)

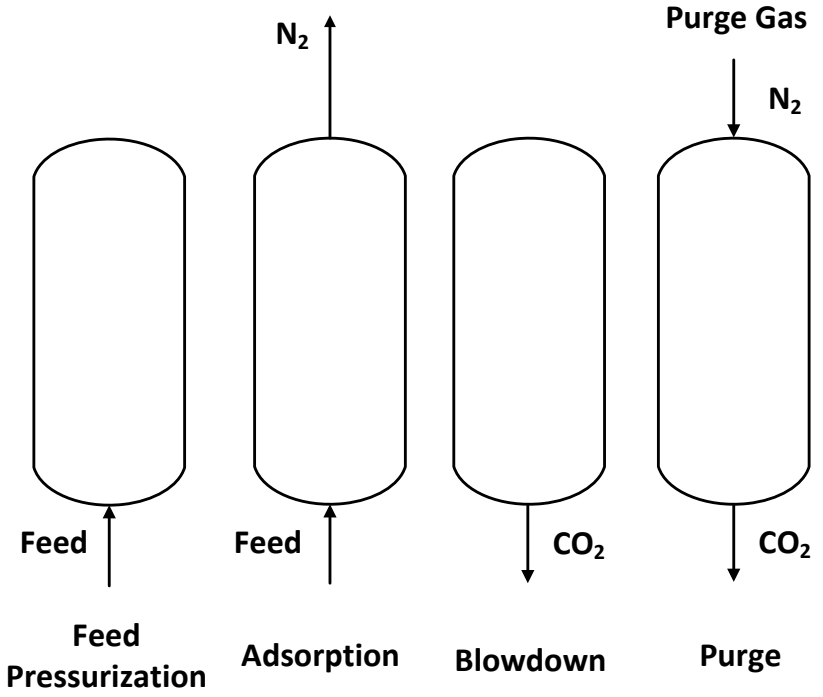

(b)

Figure 2.5: Basic 4-step a.) PVSA and b.) PSA cycles studied by Ko et al. [7]

here that the feed into the second step is the heavy product from the first step. Simulations of this 2-stage PVSA cycle resulted in a purity of 96.54% and a recovery of 93.35%, with a high pressure and low pressure of 150kPa and 10kPa respectively, in the second stage of the process.

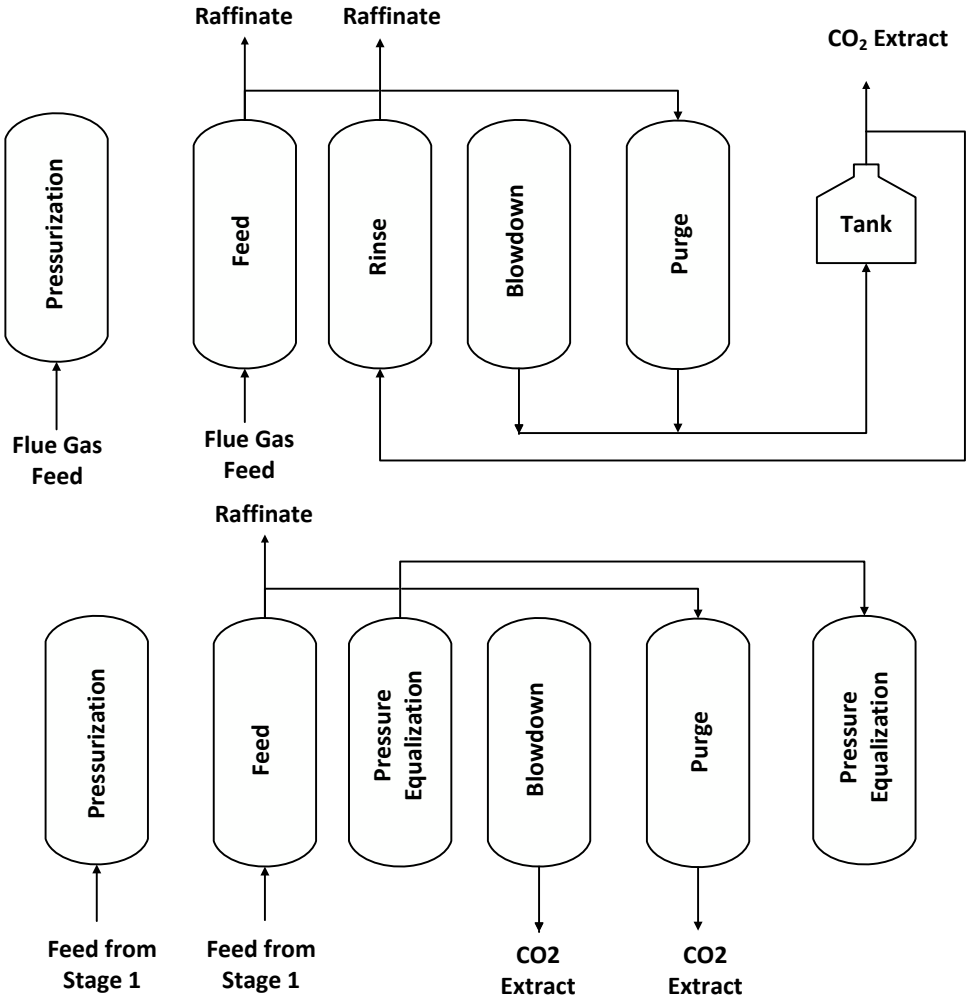

Figure 2.6: 2-stage PVSA cycle for post-combustion CO_2 capture studied by Wang et al. [8]

Haghpanah et al. performed a cycle synthesis and optimization study, wherein several different VSA cycles were considered for post-combustion CO_2 capture, and each cycle was optimized in order to evaluate the performance of all of these cycles [24]. For all cases, the feed gas was considered to be 15% CO_2 and 85% N_2, and the adsorbent was zeolite 13X. The most basic of the cycles evaluated was the 4-step VSA cycle, which is similar to the cycle proposed by Ko et al. shown in Figure 2.5a. Haghpanah et al. demonstrated that this cycle is able to achieve CO_2 purity of 95% and recovery of 90% in a previous study [25]. An

improvement to the basic 4-step PSA cycle is a 4-step cycle with light product pressurization (LPP), shown in Figure 2.7. The first step of this cycle is adsorption. Feed gas enters the column at a high pressure at 1 bar and the more strongly adsorbed component enters the solid phase, while the less strongly adsorbed component leaves through the exit end of the column. In the blowdown step the feed end of the column is closed, and the pressure reduced from P_H to an intermediate pressure, P_{INT}. The direction of flow of the blowdown step is co-current to the direction of flow in the adsorption step, so the more weakly adsorbed component in the gas mixture is desorbed, concentrated in the top end of the adsorption column then removed. In the evacuation step, the outlet or top end of the column is shut and the inlet end opened. The pressure is further reduced from the intermediate pressure,P_{INT}, to the evacuation pressure, P_L, in order to desorb and remove the more strongly adsorbed component. In the final light product pressurization step, a portion of the light product from the adsorption step is used to re-pressurize the column after the evacuation step. This is done by closing the feed/bottom end and feeding the light product from the outlet end. Pressurizing with the light product is advantageous because the front of the more strongly adsorbed component is concentrated more towards the inlet of the column, so as not to be lost in the adsorption step.

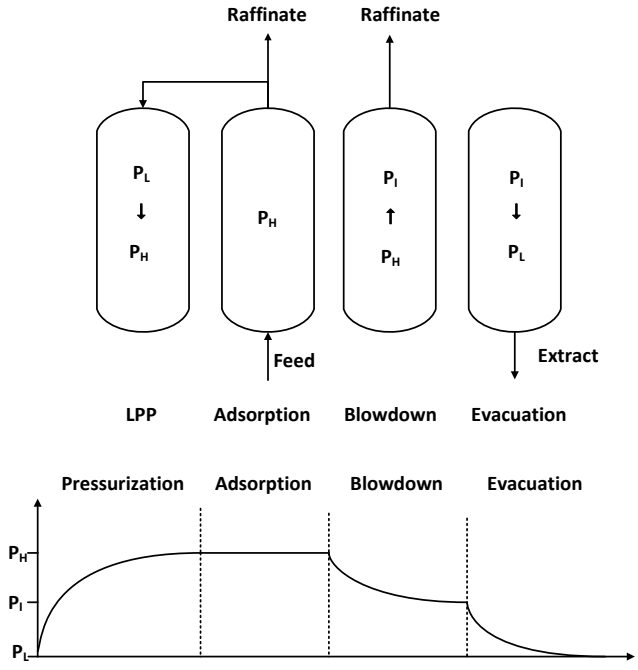

Figure 2.7: Basic 4-Step Cycle with Light Product Pressurization (LPP)

Several other cycle configurations are available in literature for PSA processes, involving

the addition of the light reflux (LR), heavy reflux (HR) and pressure equalization (PE) steps [24]. The light reflux step occurs directly after the evacuation step and feeds a portion of the light component from the adsorption step output to increase the amount of the heavy component that is removed from the column. The heavy reflux step takes the outlet stream from the evacuation step and feeds it back into the blowdown step of the P/VSA cycle. This step concentrates the heavily adsorbed component at the feed end of the column while removing the light component. The light and heavy reflux steps are shown in Figure 2.8, which is a 6-step cycle incorporating both of these steps. In pressure equalization, a high pressure or donor column after the adsorption step is connected to a low pressure or receiver column after the evacuation step. Eventually, both columns reach an intermediate pressure. This means that a PE step can effectively be used as a blowdown step without need for an additional vacuum pump, potentially saving energy at the cost of adding one column. The addition of LR, HR and PE steps to PSA cycle configurations do improve performance of PSA cycles, however the energy requirements are also high, especially for those cycles which include the heavy reflux step [24]. The only cycle which was shown to meet the U.S. DOE requirements of 90% purity and recovery at a pilot plant was the four step cycle with light product pressurization.

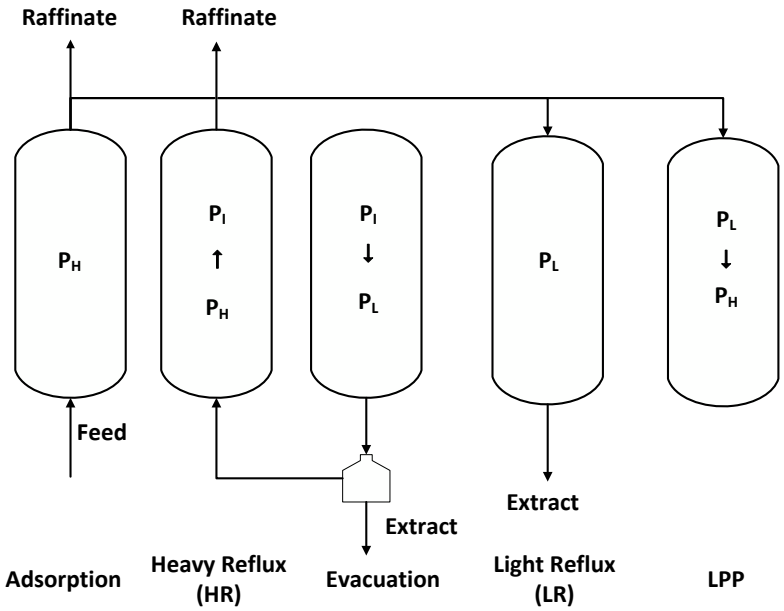

Figure 2.8: 6 Step PSA Cycle with Light Reflux and Heavy Reflux

Table 2.1 summarizes the performance of several PSA cycles found in literature, as well as

the corresponding feed condition and adsorbent material. Based on the data collected, it can be observed that activated carbon does not meet the 90% purity and recovery performance that is required for CO_2 capture. The majority of the other cycles evaluated for their CO_2 capture performance use zeolite 13X as the adsorbent. There are considerably fewer studies which consider metal-organic framework materials for post-combustion CO_2 capture.

Table 2.1: Literature Post-Combustion PSA Cycle Performance Summary

Process	Feed	Adsorbent	Purity [%]	Recovery [%]	Reference
Basic 4 Step PSA	Dry	A.C.	68.4	99	[26]
2 Stage VSA	Dry	13XAPG	96.5	93.4	[8]
2 Stage VSA	Dry	A.C.	96.4	80.4	[27]
2 Stage VSA (exp)	Dry	13XAPG	95.6	90.2	[28]
3 Step VSA	Wet	A.C.	48.23	89.8	[4]
3 Step VSA	Dry	CDX/13X	68.5	78.5	[9]
3 Step VSA	Wet	CDX/13X	67	76.9	[9]
Basic 4 Step PVSA	Dry	13X	90	93.8	[7]
Basic 4 Step VSA	Dry	13X	95	90	[25]
6 Step VSA LR+HR	Dry	13X	>95	>90	[24]
Dual Adsorbent LPP	Wet	Silica Gel/13X	95	90	[10]
Basic 4 Step LPP	Wet	13X	95	90	[10]
9 Step PVSA	Dry	13X	90-95	60-70	[29]
6 Step PVSA	Dry	13X	82-83	60-80	[29]

2.3 Effect of Water on Post-combustion CO_2 Capture by PSA

The majority of studies on post-combustion CO_2 capture by VSA in literature consider a dry flue gas mixture of 10-15% CO_2 and 80-85% N_2 by volume. However, flue gas is usually saturated with water vapour at 3-10% by volume depending on temperature. Despite being present in relatively low concentrations in post-combustion flue gas, water is very strongly adsorbed onto most adsorbents. Several studies [9,10,20,30] have shown that in the presence of water, the adsorption capacity of 13X is greatly reduced. Figure 2.9 shows the single component isotherms of water on Zeolite 13X,from the publication of Yang and LeVan [31]. At a typical feed temperature of 25°C, water is shown to have a loading greater than 12 mmol/g at a very low partial pressure of 0.01 bar. This indicates that water has a very high affinity for adsorption on Zeolite 13X.

Figure 2.10 shows the sharp reduction in the equilibrium loading of CO_2 on Zeolite 13X in a ternary mixture with water vapour and N_2 at at temperature of 25°C, using data from LeVan [20]. In each case shown, water vapour is added to a mixture of 15% CO_2 and 85%

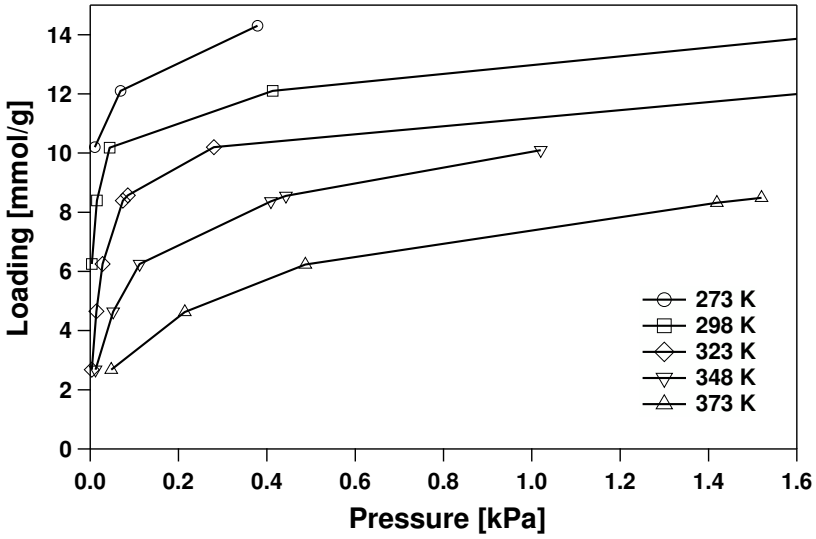

Figure 2.9: Single component H_2O isotherm on Zeolite 13X

N_2, and a competitive Langmuir isotherm model used to calculate the loading of CO_2

The effect of wet feed on PSA simulations and experiments using Zeolite 13X and other adsorbents has also been the focus of several publications [9, 10, 30]. Webley has published several papers which consider the effect of water vapour on a simple, 3 step VSA cycle shown in Figure 2.11 with 13X, activated carbon and other adsorbents. The papers involving Zeolite 13X involves a simple three step VSA cycle, with a two layered bed, with the first third of the column being a pre-layer and the rest of the bed being a main layer. The purpose of the pre-layer is the adsorption of H_2O. This pre-layer is an adsorbent which adsorbs H_2O strongly, but not CO_2, such as silica gel or activated alumina. This particular solution to humid feed in CO_2 capture by VSA is based on the observation that the water only occupies a small zone at the front of the column at cyclic steady state. The main adsorbent layer of 13X is then used for the CO_2 and N_2 separation. Using an adsorbent column of 13X with a pre-layer of alumina CDX, Webley has reported results from an experimental VSA separation of a CO_2 and N_2 feed at 97% relative humidity with a purity and recovery of 67% and 76.9% respectively [9]. For another corresponding experiment using the simple 3-step VSA cycle with dry CO_2 and N_2, 68.5% purity and 78.5% recovery is reported.

Krishnamurthy et al [10] have addressed the issue of CO_2 capture by VSA by proposing a two-bed, 4 step cycle with LPP cycle configuration, shown in Figure 2.12. The first column serves as a desiccant column filled with silica gel and the second is the main 13X column. In this proposed 2-bed, dual adsorbent cycle, the two beds undergo the same steps in a 4 step LPP cycle, however the steps are modified slightly for each column.

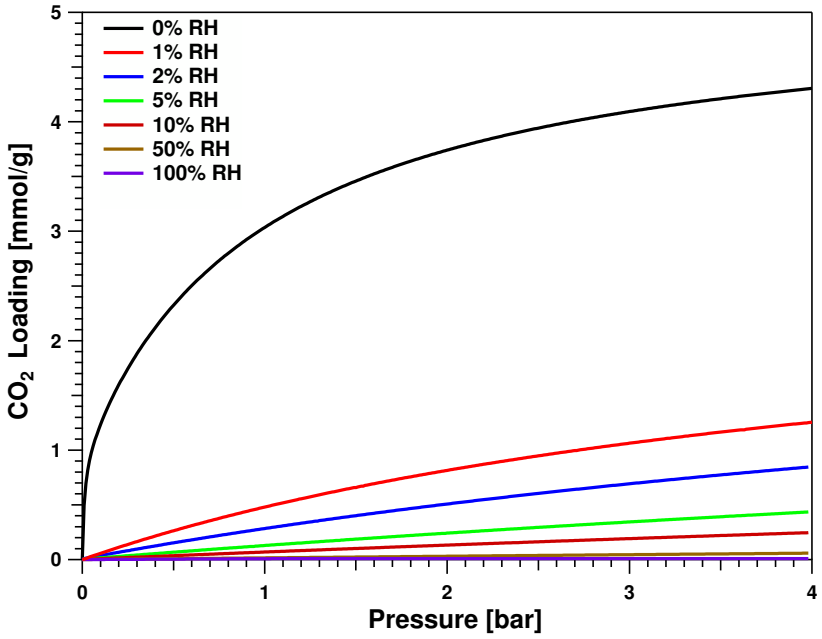

Figure 2.10: CO_2 Loading on Zeolite 13X with increasing Relative Humidity

Based on the results of multiobjective optimization of this cycle, purity and recovery in excess of 95% and 90% respectively are possible. The minimum energy reported was 177 kWh/tonne CO_2 captured with a productivity of 1.29 t CO_2 per m^3 adsorbent per day. In comparison, the minimum energy reported for a 4-step LPP cycle with dry post-combustion flue gas as feed was reported to be 154 kWh/tonne, and the same for a wet feed with a 4-step LPP cycle with 13X as the only adsorbent was 230 kWh/tonne [10]. Based on these results, the most notable effect of water on VSA process for CO_2 capture using 13X is that it significantly increases the energy required to remove the water. Performance in terms of purity and recovery is not as negatively affected because the water is a minor component of the feed at 25°C and occupies only a short mass transfer zone at the start of the column.

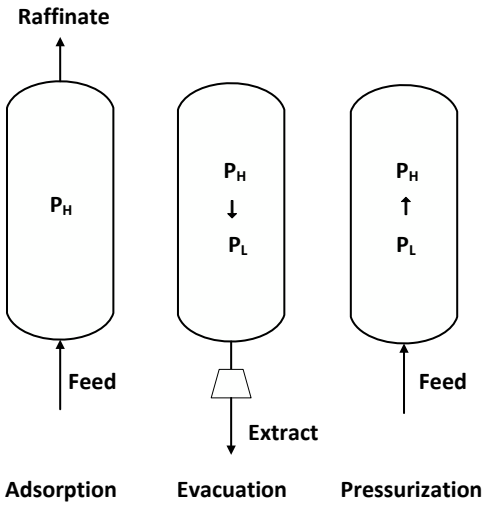

Figure 2.11: Simple 3-step VSA Cycle [9]

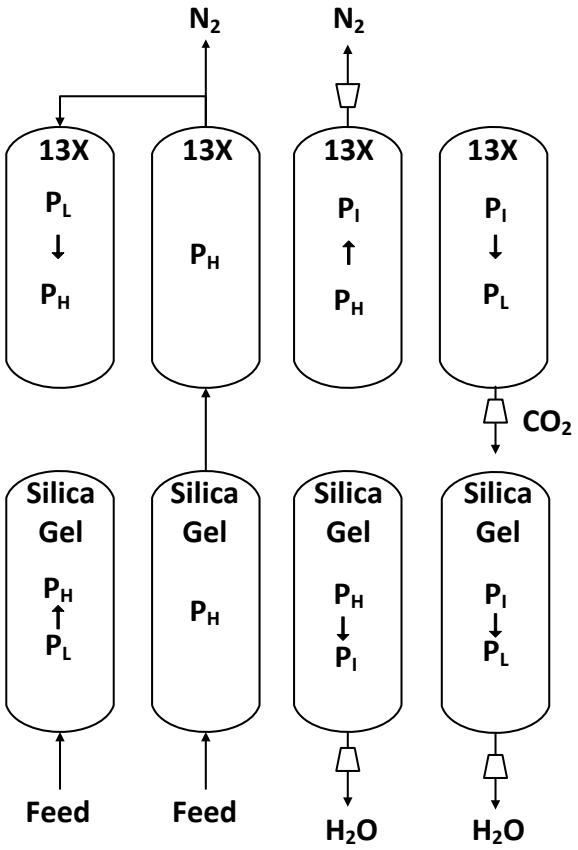

Figure 2.12: Dual-Adsorbent, 2-bed 4-step LPP cycle [10]

Chapter 3

Modeling and optimization of pressure swing adsorption processes

Pressure swing adsorption cycles are simulated using a robust, non-isothermal and non-isobaric model. The model equations are a system of partial differential equations. Using a finite volume method, these partial differential equations are written in MATLAB as a system of ordinary differential equations, discretised in space using a finite volume method and solved in time using a stiff ODE solver.

3.1 Model Equations

The model equations which describe adsorption dynamics were derived using several main assumptions which are as follows:

- An axially dispersed plug flow model is used to represent the bulk fluid flow.
- The gas phase is described by the ideal gas law.
- The solid phase mass transfer rate is described by the linear driving force (LDF) model. Furthermore, mass transfer in the solid phase is assumed to be controlled by molecular diffusion into the macropores of the adsorbent.
- Darcys law is used to account for the frictional pressure drop in the axial direction.
- Thermal equilibrium between the gas and solid phases is established instantaneously.
- No concentration, temperature, and pressure gradients exist in the radial direction. As a rule of thumb, this assumption is valid for a column with L/D ratio greater than or equal to 10.

- Heat transfer occurs across the column wall whose outer surface is maintained at a constant temperature.
- The adsorbent properties and bed voidage are uniform across the column.

The resulting model equations are a component mass balance, an overall mass balance, an energy balance, a wall energy balance and the linear driving force (LDF) equation which describes the rate of mass transfer between the solid and gas phases. The adsorption isotherm model, which is used to calculate the equilibrium loading of each component on the adsorbent at a certain state, is calculated using a competitive model. The nomenclature for all of the equations can be referred to in Appendix A. These model equations have been previously used in literature for modeling PSA processes [18], [25], [10].

Component Mass Balance

$$\frac{\partial y_i}{\partial t} = \frac{T}{P} D_{\mathrm{L}} \frac{\partial}{\partial z}\left(\frac{P}{T}\frac{\partial y_i}{\partial z}\right) - \frac{T}{P}\frac{\partial}{\partial z}\left(\frac{y_i P}{T} v\right) - \frac{y_i}{P}\frac{\partial P}{\partial t} + \frac{y_i}{T}\frac{\partial T}{\partial t} - \frac{RT}{P}\frac{(1-\varepsilon)}{\varepsilon}\frac{\partial q_i}{\partial t} \tag{3.1}$$

The axial dispersion, D_L, is calculated as detailed in Equation 3.2. In this equation, D_M represents the molecular diffusivity of the adsorbate, v_0 is the interstitial velocity and d_p is the diameter of adsorbent particles. The adsorbent particles are all assumed to be spherical.

$$D_L = 0.7 D_M + 0.5 v_0 d_p \tag{3.2}$$

Equation (3.3) is the overall mass balance, which is obtained by the sum of all of the component mass balances for the gas mixture species.

$$\frac{1}{P}\frac{\partial P}{\partial t} = \frac{1}{T}\frac{\partial T}{\partial t} - \frac{T}{P}\frac{\partial}{\partial z}\left(\frac{P}{T} v\right) - \frac{(1-\varepsilon)}{\varepsilon}\frac{RT}{P}\sum_{i=1}^{n_{\mathrm{comp}}}\frac{\partial q_i}{\partial t} \tag{3.3}$$

Two energy balance equations, 3.4 and 3.5 are used for the column and column wall respectively.

$$\begin{aligned}\left[\frac{(1-\varepsilon)}{\varepsilon}\left(\rho_{\mathrm{s}} C_{\mathrm{ps}} + C_{\mathrm{pa}}\sum_{i=1}^{n_{\mathrm{comp}}} q_i\right)\right]\frac{\partial T}{\partial t} &= \frac{K_z}{\varepsilon}\frac{\partial^2 T}{\partial z^2} - \frac{C_{\mathrm{pg}}}{R}\frac{\partial}{\partial z}(vP) - \frac{2h_{\mathrm{in}}}{\varepsilon r_{\mathrm{in}}}(T - T_{\mathrm{w}}) \\ &+ \frac{(1-\varepsilon)}{\varepsilon}\sum_{i=1}^{n_{\mathrm{comp}}}\left((-\Delta H_i)\frac{\partial q_i}{\partial t}\right) - \frac{C_{\mathrm{pg}}}{R}\frac{\partial P}{\partial t} - \frac{(1-\varepsilon)}{\varepsilon} C_{\mathrm{pa}} T \sum_{i=1}^{n_{\mathrm{comp}}}\frac{\partial q_i}{\partial t}\end{aligned} \tag{3.4}$$

$$\rho_w C_{pw}\frac{\partial T_{\mathrm{w}}}{\partial t} = K_w\frac{\partial^2 T_{\mathrm{w}}}{\partial z^2} + \frac{2 r_{\mathrm{in}} h_{\mathrm{in}}}{r_{\mathrm{out}}^2 - r_{\mathrm{in}}^2}(T - T_{\mathrm{w}}) - \frac{2 r_{\mathrm{out}} h_{\mathrm{out}}}{r_{\mathrm{out}}^2 - r_{\mathrm{in}}^2}(T_{\mathrm{w}} - T_{\mathrm{a}}) \tag{3.5}$$

Pressure drop is calculated by Darcy's Law, given by Equation 3.6. This equation is rearranged and implemented for the calculation of the local velocity.

$$-\frac{\partial P}{\partial z} = \frac{150}{4}\frac{1}{r_{\mathrm{p}}^2}\left(\frac{1-\varepsilon}{\varepsilon}\right)^2 \mu v \tag{3.6}$$

Equation 3.7 is the linear driving force or LDF model, and describes the rate of mass transfer of each component between the gas and solid phases.

$$\frac{\partial q_i}{\partial t} = k_i \left(q_i^* - q_i\right) \tag{3.7}$$

In this equation, k_i is a lumped mass transfer coefficient calculated by Equation 3.8, which is derived from the assumption that mass transfer in the solid phase is primarily controlled my molecular diffusion into the macropores [25].

$$k_i = \left(\frac{c_i}{q_i^*}\frac{15\epsilon_p D_p}{r_p^2}\right)\frac{L}{v_0} \tag{3.8}$$

The equilibrium loading of component i at a particular state, q_i^*, is calculated by the chosen isotherm model and q_i is the loading of component i at a particular point in time.

The model equations detailed in Equations 3.1 to 3.8 were coded in MATLAB in their dimensionless forms, by using reference values of the appropriate state variables within the equations.

$$\bar{T} = \frac{T}{T_0},\ \bar{P} = \frac{P}{P_0},\ \bar{T}_w = \frac{T_w}{T_0},\ x_i^* = \frac{q_i^*}{q_s},\ x_i = \frac{q_i}{q_s},\ \bar{v} = \frac{v}{v_0},\ Z = \frac{z}{L},\ \tau = \frac{tu_0}{L}$$

As an example, $\bar{T}$ is the dimensionless temperature, calculated by dividing the absolute temperature, T, by the reference temperature, T_0, which is usually equivalent to the feed temperature in units of Kelvin. The same applies for all the other variables for which the conversion from their dimensional to dimensionless forms are provided. In the other cases, the reference pressure, P_0, is taken as 101,325 Pa and the reference loading, q_s, is the maximum saturation loading for the different adsorbates, which is determined from the adsorption isotherm fitting. Several dimensionless groups are also used in the conversion from the dimensional form of the model partial differential equations to the dimensionless forms, and the corresponding equations for these terms can be found in Table 3.1. The dimensionless forms of the model equations are presented in Equations 3.9 to 3.15.

Component mass balance

$$\frac{\partial y_i}{\partial \tau} = \frac{1}{Pe}\frac{\bar{T}}{\bar{P}}\frac{\partial}{\partial Z}\left(\frac{\bar{P}}{\bar{T}}\frac{\partial y_i}{\partial Z}\right) - \frac{\bar{T}}{\bar{P}}\frac{\partial}{\partial Z}\left(\frac{y_i \bar{P}}{\bar{T}}\bar{v}\right) - \frac{y_i}{\bar{P}}\frac{\partial \bar{P}}{\partial \tau} + \frac{y_i}{\bar{T}}\frac{\partial \bar{T}}{\partial \tau} - \Psi\frac{\bar{T}}{\bar{P}}\frac{\partial x_i}{\partial \tau} \tag{3.9}$$

Table 3.1: Dimensionless groups used in model equations

$$Pe = \frac{v_0 L}{D_L} \qquad Pe_H = \frac{\varepsilon_b v_0 L \rho_g C_{pg}}{K_z} \qquad \Psi = \frac{1-\varepsilon_b}{\varepsilon_b}\frac{RT_0 q_s}{P_0}$$

$$\Pi_1 = \frac{K_w}{\rho_w C_{pw} v_0 L} \qquad \Pi_2 = \frac{2r_{\text{in}} h_{\text{in}} L}{\rho_{\text{w}} C_{pw} v_0 (r_{\text{out}}^2 - r_{\text{in}}^2)} \qquad \Pi_3 = \frac{2r_{\text{out}} h_{\text{out}} L}{\rho_w C_{pw} v_0 (r_{\text{out}}^2 - r_{\text{in}}^2)}$$

$$\Omega_1 = \frac{K_z}{(\frac{1-\varepsilon_b}{\varepsilon_b})(\rho_s C_{ps} + C_{pa} q_s \sum_{i=1}^{n} x_i))\varepsilon_b v_0 L} \qquad \Omega_2 = \frac{C_{pg}}{(\frac{1-\varepsilon_b}{\varepsilon_b})(\rho_s C_{ps} + C_{pa} q_s \sum_{i=1}^{n} x_i))}\frac{P_0}{RT_0}$$

$$\sigma_i = \frac{(-\triangle H_i) q_s}{T_0(1-\varepsilon_b)(\rho_s c_{ps} + C_{pa} q_s \sum_{i=1}^{n} x_i))} \qquad \Omega_3 = \frac{(C_{pa} q_s)}{(\rho_s C_{ps} + c_{pa} q_s \sum_{i=1}^{n} x_i)}$$

$$\Omega_4 = \frac{2h_{\text{in}} L}{\varepsilon_b r_{\text{in}} v_0 (\frac{1-\varepsilon_b}{\varepsilon_b}(\rho_s C_{ps} + C_{pa} q_s \sum_{i=1}^{n} x_i))}$$

Overall mass balance

$$\frac{\partial \bar{P}}{\partial \tau} = \frac{\bar{P}}{\bar{T}}\frac{\partial \bar{T}}{\partial \tau} - \bar{T}\frac{\partial}{\partial Z}\left(\frac{\bar{P}}{\bar{T}}\bar{v}\right) - \Psi \bar{T} \sum_{i=1}^{n_{\text{comp}}} \frac{\partial x_i}{\partial \tau} \tag{3.10}$$

Column energy balance

$$\frac{\partial \bar{T}}{\partial \tau} = \Omega_1 \frac{\partial^2 \bar{T}}{\partial Z^2} - \Omega_2 \frac{\partial}{\partial Z}(\bar{v}\bar{P}) - \Omega_3 \bar{T} \sum_{i=1}^{n_{\text{comp}}} \frac{\partial x_i}{\partial \tau} + \sum_{i=1}^{n_{\text{comp}}} \left(\sigma_i \frac{\partial x_i}{\partial \tau}\right) - \Omega_4(\bar{T} - \bar{T_w}) - \Omega_2 \frac{\partial \bar{P}}{\partial \tau} \tag{3.11}$$

Wall energy balance

$$\frac{\partial \bar{T_w}}{\partial \tau} = \Pi_1 \frac{\partial^2 \bar{T_w}}{\partial Z^2} + \Pi_2(\bar{T} - \bar{T_w}) - \Pi_3(\bar{T_w} - \bar{T_a}) \tag{3.12}$$

LDF model for solid phase mass transfer

$$\frac{\partial x_i}{\partial \tau} = \alpha_i (x_i^* - x_i) \tag{3.13}$$

Pressure drop

$$\bar{v} = \frac{4}{150}\left(\frac{\varepsilon}{1-\varepsilon}\right)^2 r_p^2 \frac{P_0}{\mu v_0 L}\left(-\frac{\partial \bar{P}}{\partial Z}\right) \tag{3.14}$$

Adsorbed phase mass balance

$$\frac{\partial \bar{P}}{\partial \tau} = \frac{\bar{P}}{\bar{T}}\frac{\partial \bar{T}}{\partial \tau} - \bar{T}\frac{\partial}{\partial Z}\left(\frac{\bar{P}}{\bar{T}}\bar{v}\right) - \Psi \bar{T} \sum_{i=1}^{n_{\text{comp}}} \frac{\partial x_i}{\partial \tau} \tag{3.15}$$

3.2 Finite Volume Method

Spatial discretization of the model equations can be done using finite difference, finite element or finite volume methods. The finite volume scheme is used in this case because it

gives high accuracy, can resolve sharp discontinuities and avoids numerical dispersion which can lead to incorrect solutions. Nonlinearities are also common in adsorption dynamics therefore this was the chosen option.

Several finite volume schemes can be used for the calculation of the state variables. These include the upwind difference scheme (UDS), high resolution total variation diminishing (TVD) schemes such as van Leer and Superbee, and the weighted essentially nonoscillatory (WENO) method. The UDS approximates to a finite difference scheme and is susceptible to numerical dispersion therefore was not chosen. The WENO, van Leer and Superbee methods have previously been shown to accurately simulate adsorption processes [25]. Haghpanah et al. have demonstrated in this publication that the van Leer TVD scheme can both accurately and efficiently be implemented in order to simulate adsorption dynamics in PSA cycles [25]. This scheme involves the general finite volume equations, as well as a flux limiter, the purpose of which is to mitigate numerical errors and reduce oscillations in the solution near the sharp adsorption fronts

In the finite volume scheme, the adsorption column is considered to be composed of a number of cells, N, each with a volume of ΔV. Higher values of N result in a higher degree of accuracy in the solution, at the cost of additional computational time. Haghpanah et al. performed a systematic study of the effect of N on the results of a four-step PSA cycle, using N=2000 as a reference case [25]. It was shown that 30 volume elements using the Van Leer scheme was both efficient in terms of computational time and accurate with respect to the reference solution. In the chosen finite volume method, all state variables are approximated using an average for each cell, given in Equation 3.16.

$$f_j(t) = \frac{1}{\Delta V} \int_{V_j} f(t) dV \tag{3.16}$$

Integration over each cell with respect to boundaries (j-0.5) and (j+0.5) allows for conversion of spatial derivatives to algebraic expressions. The general finite volume scheme equations are given by equations 3.17 to 3.20:

$$f_{j+0.5} = f_j + \frac{1}{2}\phi(r_{j+0.5})(f_{j+1} - f_i) \tag{3.17}$$

$$r_{j+0.5} = \frac{f_j - f_{j-1} + \delta}{f_{j+1} - f_j + \delta} \tag{3.18}$$

The van leer flux limiter can be expressed as

$$\phi(r_{j+0.5}) = \frac{r_{j+0.5} + |r_{j+0.5}|}{1 + |r_{j+0.5}|} \tag{3.19}$$

And at the boundary condition for the first and N^{th} cells:

$$r_{1+0.5} = \frac{2(f_1 - f_{0.5} + \delta)}{f_2 - f_1 + \delta} \tag{3.20}$$

These equations were used to discretize the dimensionless model equations in space with 30 finite volumes. The spatial discretization at the boundaries, however, requires that the appropriate initial conditions and boundary conditions be applied. For PSA cycles, the initial condition is assumed to be a column that is saturated with the weakly adsorbed component, which is nitrogen in this case. That is, the simulation begins with a column that is filled with pure nitrogen gas at 1 bar and a specified temperature. For the four step PSA cycle, from pressurization to evacuation, the initial condition of each step is taken as the final condition of the previous step. The relevant boundary conditions used for the modeling of a four step PSA cycle are evoked from Danckwert's boundary conditions for dispersed plug flow, as well as the model equations previously discussed. The boundary conditions for a basic four step cycle are fully detailed in Appendix B. The implementation of the boundary conditions with the finite volume scheme results in a system of ordinary differential equations (ODE's) which are then solved by using a stiff ODE solver in MATLAB, such as ode15s or ode23s.

3.3 Basic 4-Step Cycle with LPP

The cycle configuration which is simulated is the 4-step adsorption cycle with LPP, due to it being shown to meet the target purity and recovery performance for post-combustion CO_2 capture, as well as having relatively low energy requirements when compared to other cycle configurations in literature [24]. For clarity, this cycle is shown in Figure 3.1. The cycle is simulated as a single adsorption column sequentially undergoing the pressurization, adsorption, co-current blowdown and evacuation steps. All boundary conditions stated previously apply, however, for pressurization with the light product, the direction of pressurization is countercurrent to that for feed pressurization so the inlet and outlet boundary conditions specified previously can be simply interchanged. There are six input parameters directly related to the 4-step LPP VSA process, which are the time of the adsorption, blowdown and

evacuation steps, the intermediate or blowdown pressure, the low or evacuation pressure and inlet velocity. For the first ten cycles, feed pressurization is performed in which the bed is pressurized using the feed mixture which is usually 15% CO_2 and 85% N_2. After these initial cycles, the pressurization is done with the light product of the previous adsorption step, which is primarily composed of nitrogen assuming there is no breakthrough of the CO_2 front through the column.

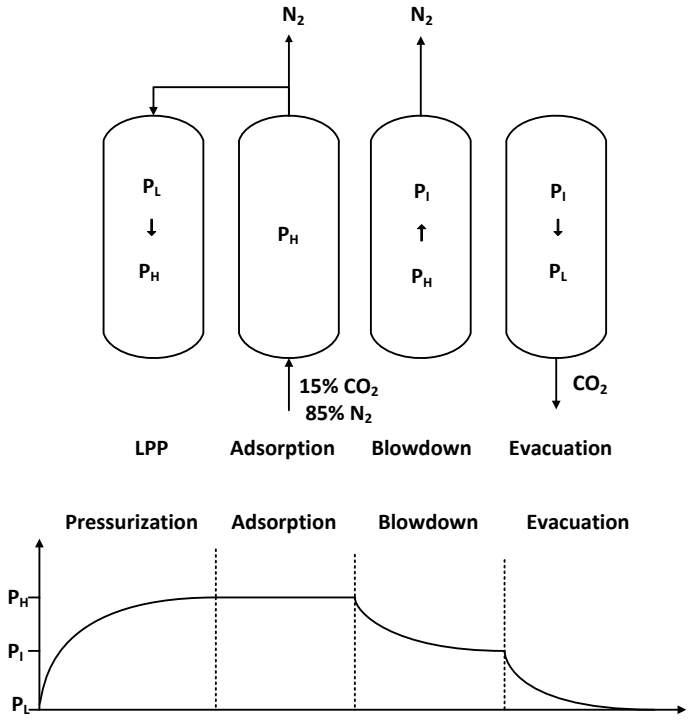

Figure 3.1: 4-Step LPP Cycle used in Simulations

The performance indicators for PSA cycles are purity, recovery, energy and recovery. These are given by Equations 3.21 to 3.27.

Purity is the ratio of the moles of CO_2 coming out of the evacuation step to the total number of moles coming out of the evacuation step.

$$\text{Purity} = \frac{\text{mol CO}_2\ \text{out}_{\text{evac}}}{\text{mol CO}_2\ \text{out}_{\text{evac}} + \text{mol N}_2\ \text{out}_{\text{evac}}} \times 100 \tag{3.21}$$

Recovery is the ratio of the moles of CO_2 coming out of the evacuation step to the total number of moles of CO_2 fed into the adsorption step (and the feed pressurization step, if used).

$$\text{Recovery} = \frac{\text{mol CO}_2\ \text{out}_{\text{evac}}}{\text{mol CO}_2\ \text{in}_{\text{ads}} + \text{mol CO}_2\ \text{in}_{\text{press}}} \times 100 \tag{3.22}$$

The energy is calculated for each step of the VSA cycle, by Equations 3.23 to 3.25.

$$\mathrm{E_{ads}} = \frac{1}{\eta}\epsilon\pi r_{\mathrm{in}}^2 v_0 P_0 \frac{\gamma}{\gamma-1}\int_{t=0}^{t=t_{ads}} (\bar{v}\bar{P})\left[(\frac{P_0\bar{P}}{P_f})^{\frac{(\gamma-1)}{\gamma}} - 1\right] dt \tag{3.23}$$

$$\mathrm{E_{bd}} = \frac{1}{\eta}\epsilon\pi r_{\mathrm{in}}^2 v_0 P_0 \frac{\gamma}{\gamma-1}\int_{t=0}^{t=t_{bd}} (\bar{v}\bar{P})\left[(\frac{P_{\mathrm{atm}}}{P_0\bar{P}})^{\frac{(\gamma-1)}{\gamma}} - 1\right] dt \tag{3.24}$$

$$\mathrm{E_{evac}} = \frac{1}{\eta}\epsilon\pi r_{\mathrm{in}}^2 v_0 P_0 \frac{\gamma}{\gamma-1}\int_{t=0}^{t=t_{ads}} (\bar{v}\bar{P})\left[(\frac{P_0\bar{P}}{P_f})^{\frac{\gamma-1}{\gamma}} - 1\right] dt \tag{3.25}$$

The pressurization step energy = 0 in the case of VSA, where $\mathrm{P_H}$ = 1 bar. In these equations, η represents the efficiency of the vacuum pumps, which is assumed to be 72%. The symbol γ represents the adiabatic constant, and is assumed to have a value of 1.4. The energy consumption of the cycle is taken as the ratio of the sum of the energy for all of the steps to the mass of CO_2 extracted from the evacuation step per cycle. This is given in Equation 3.26. In order to convert the mass unit to tonnes, the relevant conversion factors are applied.

$$\mathrm{Energy} = \frac{\mathrm{E_{press}} + \mathrm{E_{ads}} + \mathrm{E_{blow}} + \mathrm{E_{evac}}}{\text{mass of } CO_2 \text{ evac per cycle}} \tag{3.26}$$

The productivity is the amount of CO_2 extracted per volume of adsorbent per cycle time. This performance indicator gives an idea of the efficiency of the adsorption cycle in terms of the volume of adsorbent required and the time required per cycle. i.e. Less volume of adsorbent required and lower cycle times to recover CO_2 on a molar basis means higher productivity.

$$\mathrm{Productivity} = \frac{\text{mol } CO_2 \text{ extracted per cycle}}{AL(\mathrm{t_{LPP}} + \mathrm{t_{ads}} + \mathrm{t_{blow}} + \mathrm{t_{evac}})} \tag{3.27}$$

3.4 Cyclic Steady State

At every step in the four-step VSA cycle, the pressure is changed and the boundary conditions are altered in the simulation based on whether the column inlet or outlet is open or closed. Each step is allowed to run for a specific time, and the bed is not completely purged or cleaned at the end of each cycle. The repercussion of all of these conditions changing as the cycle progresses through the four steps is that the process is running in an unsteady

state. Assuming a binary feed of carbon dioxide and nitrogen, there will be two separate fronts of CO_2 and N_2 within the column, each of which will continuously move between steps, as well as at the same step between subsequent cycles. The performance indicators of purity and recovery therefore change from cycle to cycle and are not constant. When cycles are run repeatedly, there is a point at which the state variables of temperature, gas and solid phase composition and pressure for the same step remains constant for subsequent cycles. At this point, the VSA cycle has attained cyclic steady state (CSS) condition, and the performance of subsequent cycles in terms of purity and recovery is constant. This is very important for simulations as the criterion for CSS must be implemented in order to determine whether or not the results in terms of purity and recovery are valid.

Cyclic steady state attainment is determined by the convergence of the mass balance of carbon dioxide over the entire cycle. For a simulation with a feed of 15% CO_2 and 85% N_2, the mass balance error for CO_2 is plotted against the number of cycles simulated. The number of cycles which must be run to cyclic steady state varies from less than 100 cycles to over 2000 cycles based on several factors, including but not limited to the initial conditions, the operating parameters of the cycle and the shape of the isotherms that are considered. The criterion for CSS that is used in this study is the convergence of the mass balance for the heavily adsorbed component, assuming a binary mixture as the feed. The mass balance error for the four step PSA cycle, calculated by Equation 3.28, must be less than 0.5% for five successive cycles for simulations to cease.

$$\text{Mass Balance Error} = \frac{\text{molCO}_2\text{out}_{\text{evac}} + \text{molCO}_2\text{out}_{\text{ads}} + \text{molCO}_2\text{out}_{\text{blow}}}{\text{molCO}_2\text{in}_{\text{ads}} + \text{molCO}_2\text{in}_{\text{press}}} \times 100 \quad (3.28)$$

Figure 3.2 illustrates the mass balance convergence for two simulations of a 4-step cycle simulation using SIFSIX-3-Zn, with the only difference between the two simulations being the component the bed is initially saturated with. Additionally, Figure 3.3 shows how the two performance indicators of purity and recovery converge with the mass balance. The solid lines indicating a simulation which is initiated with a CO_2 loaded bed comes to cyclic steady state with significantly fewer simulated cycles, and the N_2 loaded bed, indicated by the dotted lines fluctuates and eventually converges to the same purity and recovery values over several thousand cycles simulated. As previously mentioned, the default starting condition for simulations is that the bed is saturated with N_2 at 1 bar. However, in this case the mass balance criterion is satisfied for over 500 cycles before increasing once again. Simulating 5000 cycles is very time consuming for the purpose of optimization, therefore

this issue of mass balance criterion is addressed in two ways. The first is by allowing all simulations to run to a maximum of 2000 cycles in order to achieve the aforementioned CSS criterion. Furthermore, for CO_2 isotherms such as SIFSIX-3-Zn that display a sharp gradient at very low pressures, the initial condition is changed to a bed which is loaded with CO_2.

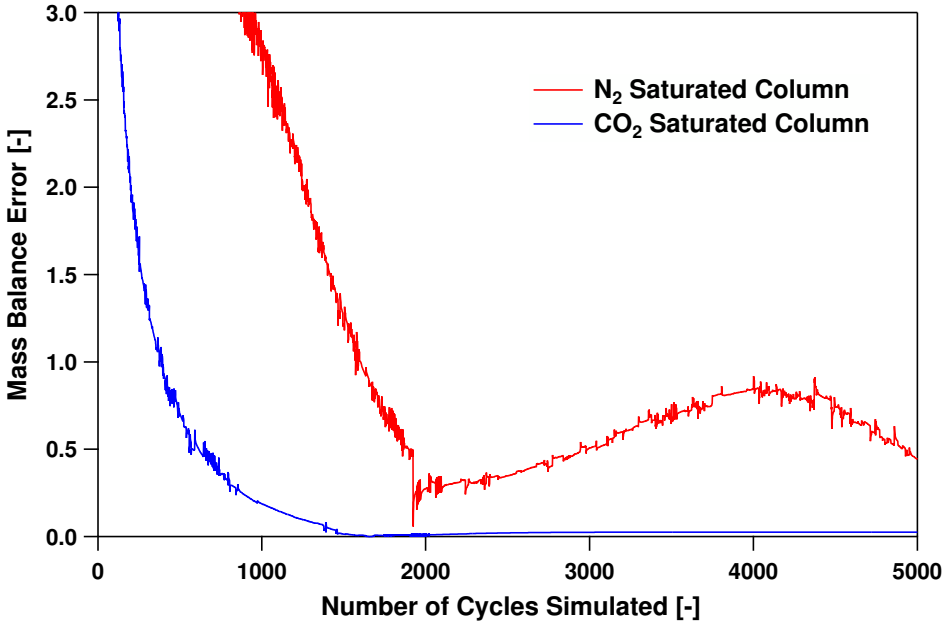

Figure 3.2: Convergence of mass balance for a 4 step LPP cycle with SIFSIX-3-Zn adsorbent

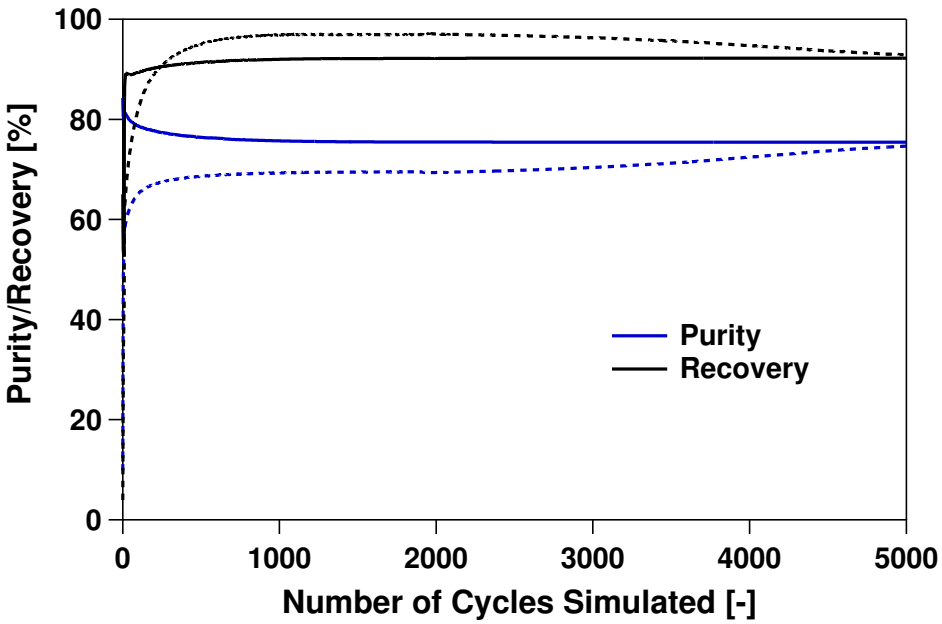

Figure 3.3: Convergence of purity and recovery for a 4 step LPP cycle with SIFSIX-3-Zn adsorbent. Dotted lines indicate a simulation with a bed initially saturated with N_2 and solid lines indicate a simulation with a bed initially saturated with CO_2.

3.5 Optimization Procedure and Methodology

As mentioned previously, there are six parameters in an adsorption cycle which are taken as the inputs. These are the times for the adsorption, blowdown and evacuation steps, the inlet or feed velocity, the intermediate or blowdown pressure and the evacuation pressure. All of these operating parameters individually affect the VSA cycle performance by the four performance indicators mentioned. The time of adsorption step, inlet velocity, intermediate pressure and low pressure affect the purity and recovery of the cycle. All of the operating parameters listed affect the Energy and Productivity. Because there are six operating parameters for a given VSA cycle, parametric studies cannot be used to determine the optimal combination of parameters for which a four-step LPP VSA process can perform. An optimizer is needed which will select the values of the six operating parameters which will result in maximum Purity and Recovery, while maximizing productivity and minimizing the energy costs of the process.

A genetic algorithm (GA) optimization routine included in the MATLAB optimization toolbox, gamultiobj, is employed to perform optimization problems in this study. The genetic algorithm is non-gradient based and selects values of the decision variables within a specified range. These decision variables are passed to the full model as input parameters and the

simulation is carried out until cyclic steady state is achieved. Once this has happened, the model passes results back to the optimizer in the form of objective functions. The ultimate goal of the genetic algorithm is to minimize these objective functions. This is done for a population of 144 sets of decision variables. The optimizer then proceeds in a manner similar to genetic evolution. Based on the values of the objective functions obtained for the first generation, the optimizer generates a subsequent population of 144 sets of decision variables subsequent generation using either crossover or mutation functions. Crossover refers to when the optimizer narrows the search region to generate decision variables which result in lower values of the objective functions. Mutations are more random values of decision variables passed to a subsequent generation which serve the purpose of searching for more combinations of decision variables in the specified range and avoiding local minima.

The genetic algorithm searches for a minimum value of the objective functions that are specified in the full PSA model. These are related to the performance indicators specified earlier. For purity-recovery optimization the objective functions are given in Equations 3.29 and 3.30. These are the inverse of the purity and recovery obtained from the full model, so purity and recovery are maximized when both of these objective functions are minimized.

$$\mathrm{J}_1 = \frac{1}{\mathrm{Purity}} \tag{3.29}$$

$$\mathrm{J}_2 = \frac{1}{\mathrm{Recovery}} \tag{3.30}$$

Energy and productivity optimization, however, must be constrained to ensure that the performance of the PSA cycle is satisfactory, that is, at least 90% purity and recovery. This is done by penalizing the objective functions for energy and productivity such that the magnitude of the values of the objective functions increase significantly when the purity or recovery drops below the performance threshold of 90%. The objective functions for energy and productivity optimization are given in Equations 3.31 and 3.32. The results of both types of multiobjective optimization are analyzed by observing the trade-offs between purity and recovery and energy and productivity, respectively.

$$\mathrm{J}_3 = \frac{\mathrm{Energy}}{165} + 10000(\max[0, \mathrm{TolPu} - \mathrm{Pu}])^2 + 10000(\max[0, \mathrm{TolRe} - \mathrm{Re}])^2 \tag{3.31}$$

$$\mathrm{J}_4 = \frac{1}{\mathrm{Productivity}} + 10000(\max[0, \mathrm{TolPu} - \mathrm{Pu}])^2 + 10000(\max[0, \mathrm{TolRe} - \mathrm{Re}])^2 \tag{3.32}$$

Chapter 4

Evaluation of SiF_6 Metal-Organic Frameworks for Post-Combustion CO_2 Capture

4.1 Properties of SiF_6 Adsorbents

Relatively recently, a family of metal-organic frameworks consisting two dimensional nets based on linked metal ions which are pillared via silicon hexafluoride (SiF_6) anions in the third dimension to form a three-dimensional net with cubic morphology. These 'SIFSIX' materials have been reported to show very selective uptake of carbon dioxide in the presence of other gases, such as nitrogen and methane [5]. The original SIFSIX metal-organic framework material, SIFSIX-1-Cu, has square pore channels of size 13.05 Å. Nugent et al. have drawn attention to several variants of this material, namely SIFSIX-2-Cu-i ($[Cu(dpa)_2(SiF_6)]_n \bullet 2.5CH_3OH$) and SIFSIX-3-Zn ($[Zn(pyr)_2(SiF_6)]_n$), which are also layered 3-dimensional cubic nets, with pore sizes of 5.15 Åand 3.84 Å, respectively. The dominating adsorption mechanism which is reported to result in the high CO_2 selectivity over N_2, H_2 and H_2O is the equilibrium effect due to the electrostatic interactions with the SIFSIX pillered anions [32]. Faster adsorption kinetics for CO_2 on SIFSIX-3-Zn compared to N_2, H_2 and CH_4 have also been shown for SIFSIX-3-Zn [5]. An additional feature of the SIFSIX MOFs, particularly SIFSIX-2-Cu-i, is that samples have been reported to retain crystal structure after being immersed in water for weeks, [5], [32] unlike other MOFs proposed for CO_2 capture such as Mg_2DOBDC, which is only stable under low humidity conditions [33]. This means that in practical usage, Mg_2DOBDC is only able to be used with pre-dried feed gas, a constraint which is not present with SIFSIX-2-Cu-i.

Nugent et al. experimentally measured measured single component adsorption isotherms at low pressure and temperatures varying from 273 to 338K for CO_2, and at 298K for N_2

on both SIFSIX-2-Cu-i and SIFSIX-3-Zn. The isotherm data was reported to have been measured using a Micromeritics ASAP2020 Surface Area and Porosity Analyzer [5]. Prior to these adsorption measurements, the adsorbent samples were activated and degassed under high vacuum for 16 hours. The isosteric heats at several loadings were then estimated by the Clausius-Clapeyron Equation, by considering the adsorption isotherms at different temperatures and constant loading. Carbon dioxide and nitrogen selectivity on the two SIFSIX adsorbents were predicted by using the ideal adsorbed solution theory (IAST) and fitted single component isotherm models, for a mixture of 10% carbon dioxide and 90% nitrogen. The IAST predictions were then compared to breakthrough results for verification. Literature reports CO_2/N_2 IAST selectivity for a 25°C mixture of 10% CO_2 and 90% N_2 of 1818 for SIFSIX-3-Zn and 140 for SIFSIX-2-Cu-i respectively.

4.2 Modeling of adsorption equilibrium data for SiF_6 adsorbents

The adsorption isotherms of CO_2 and N_2 on the SIFSIX MOFs have a favorable shape and are classified as a type I isotherm. The model which is selected for modeling these adsorption isotherms is a single site Langmuir model. For the single site Langmuir model, the key assumptions are that adsorption occurs on a monolayer, hence there is a maximum loading or saturation capacity, q_s, of gas on the adsorbent and secondly, that the adsorption sites are energetically homogeneous and all have the same heat of adsorption. Equation 4.1 is the single Langmuir isotherm model for a single component, i. q_s is the saturation loading, b_0 is the adsorption affinity term and $\triangle U$ is the internal energy of adsorption. These three variables are treated as fitted parameters to fit to the experimental data.

$$q_i^* = q_{si}\frac{b_{0i}\exp(\frac{\triangle U_i}{RT})C_i}{1 + b_{0i}\exp(\frac{\triangle U_i}{RT})C_i} \tag{4.1}$$

Fitting of experimental data to the Langmuir isotherm model was done by a nonlinear regression method. The multiple fitted isotherm parameters are selected such that the model fits the experimental adsorption equilibrium data at all temperatures. This is done by minimizing an objective function, given by the Equation 4.2.

$$\text{Min J} = \sum_{T}\sum_{P}\frac{|q_{exp} - q_{model}|}{q_{exp}} \tag{4.2}$$

The objective function was minimized in MATLAB, using a constrained non-linear optimization routine, fmincon. The goal of this is to minimize the difference between the total

set of experimental points over all temperatures and pressures, giving equal weighting in the fitting to pressures in both the high and low pressure range. The inputs to the fmincon routine are the experimental adsorption data [5], the isotherm model equation, upper and lower bounds for each of the fitted parameters and an initial guess for these parameters, x_0. This fitting procedure was repeated for nitrogen, for which isotherms were only available at temperatures of 77 and 298K. Multiple temperature fits for SIFSIX-2-Cu-i and SIFSIX-3-Zn are shown in Figures 4.1 and 4.2 respectively and the corresponding fitted parameters are presented in Table 4.1. The fitted values of $\triangle U$ agrees fairly well with the isosteric heats determined by Nugent et al., which is 31-40 kJ/mol for CO_2 on SIFSIX-2-Cu-i and 46 kJ/mol on SIFSIX-3-Zn.

Table 4.1: SIFSIX CO_2 and N_2 Langmuir model fitted parameters

Parameter	CO_2 Fitted Parameters		N_2 Fitted Parameters	
	SIFSIX-2-Cu-i	SIFSIX-3-Zn	SIFSIX-2-Cu-i	SIFSIX-3-Zn
q_s [mmol g^{-1}]	7.17	2.64	7.18	3.15
b_0 [m^3 mol^{-1}]	8.3 x 10^{-8}	1.72 x 10^{-8}	3.21 x 10^{-5}	6.89 x 10^{-5}
$\triangle U$ [kJ mol^{-1}]	-33.85	-48.56	-8.372	-8.372

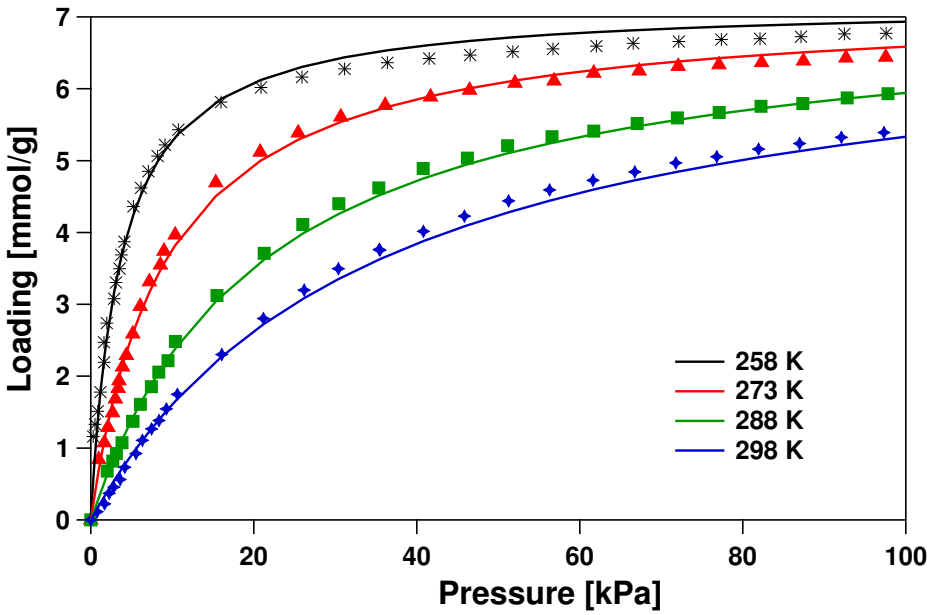

Figure 4.1: SIFSIX-2-Cu-i carbon dioxide single component isotherm fits. The lines represent Langmuir model fits and the symbols represent experimental isotherm data extracted from literature [5].

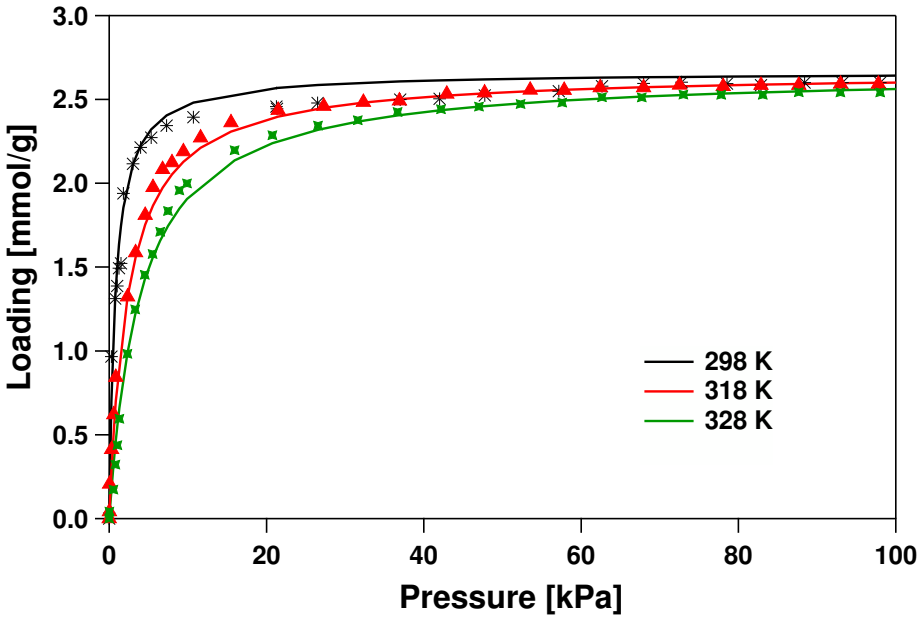

Figure 4.2: SIFSIX-3-Zn carbon dioxide single component isotherm fits. The lines represent Langmuir model fits and the symbols represent experimental isotherm data extracted from literature [5].

4.2.1 Modeling competitive adsorption

In order to accurately model the dynamics and understand the process of the VSA separation of CO_2 from N_2, the competitive effects must be modeled. In the mechanism of adsorption in a binary gas mixture, both components will compete for adsorption on the same sites. The loading of each component will change based on the composition of the gas stream, as well as the relative strength of adsorption of each component. Multiple component adsorption isotherms were not provided in the literature, however the Langmuir model can be explicitly extended to account for competitive adsorption when the saturation capacities of different components are similar. The extended Langmuir model used for the calculation of multiple component adsorption equilibrium data is derived from the ideal adsorbed solution theory (IAST). A detailed description of the IAST, including the equations and assumptions involved, is provided in the Appendix. Equation 4.3 is an explicit extended Langmuir equation for multiple components.

$$q_i^* = \frac{q_{sbi} b_i C_i}{1 + \sum b_i C_i} \tag{4.3}$$

.

4.3 Effect of water on SIFSIX Adsorbents - Experimental Breakthrough

Experimental breakthrough experiments were reported by Nugent et al. for SIFSIX-2-Cu-i and SIFSIX-3-Zn using a stainless steel column of length 27mm, with 4mm inner diameter and 6.7mm outer diameter [5]. The gas mixtures used in these breakthrough experiments were CO_2/N_2 and CO_2/H_2, with feed composition of 10%/90% and 30%/70% respectively. The effect of water on breakthrough was also investigated for both of these cases by adding water to 74% relative humidity for both of the gas mixtures. All of these breakthrough experiments reported were carried out at a temperature of 25°C and 1 bar. Prior to each breakthrough experiment, the column was regenerated under a helium flow of 5 mL/min overnight at 25°C. The helium flow was then switched to the breakthrough gas mixture at the same flowrate when the breakthrough experiment began.

The experimental breakthrough curves obtained by Nugent et al. are reproduced in Figure 4.3. In this plot, the concentration of each component in the gas mixture at the outlet of the breakthrough column is plotted as a ratio of its initial concentration in the feed mixture. Therefore, when this ratio is equal to 1, the outlet concentration is equal to the feed concentration of the component, indicating that breakthrough is complete. A scenario where the ratio of the outlet to the inlet concentration of a species is greater than 1, is called an overshoot. This occurs when the front of a weakly adsorbed or light component is followed by that of a more strongly adsorbed or heavy component in the column. The light component moves from the solid phase to the gas phase, therefore a higher concentration of that species is present at the outlet than in the feed, until breakthrough of both the light and heavy components is complete.

With a feed mixture of dry 10% CO_2 and 90% N_2, as in Figure 4.3(a) and 4.3(b), N_2 displays an overshoot indicating that it is more weakly adsorbed, as expected. When water is added to the feed, the CO_2 breakthrough occurs sooner in SIFSIX-2-Cu-i and later in SIFSIX-3-Zn, indicating an apparent slight reduction in capacity of CO_2 in SIFSIX-2 and an increase of capacity of CO_2 in SIFSIX-3. Interestingly, in both of these cases the breakthrough of water is not shown, but an overshoot is not present for CO_2, which indicates that it is not displaced by any other species in both cases. The corresponding breakthrough curves for a 30% CO_2 and 70% N_2 feed are presented in Figures 4.3(c) and 4.3(d). For both SIFSIX adsorbents, it is observed that at higher CO_2 inlet concentrations, both H_2 and water vapor breakthroughs occur before CO_2, with water overshoot for both SIFSIX-2-Cu-i

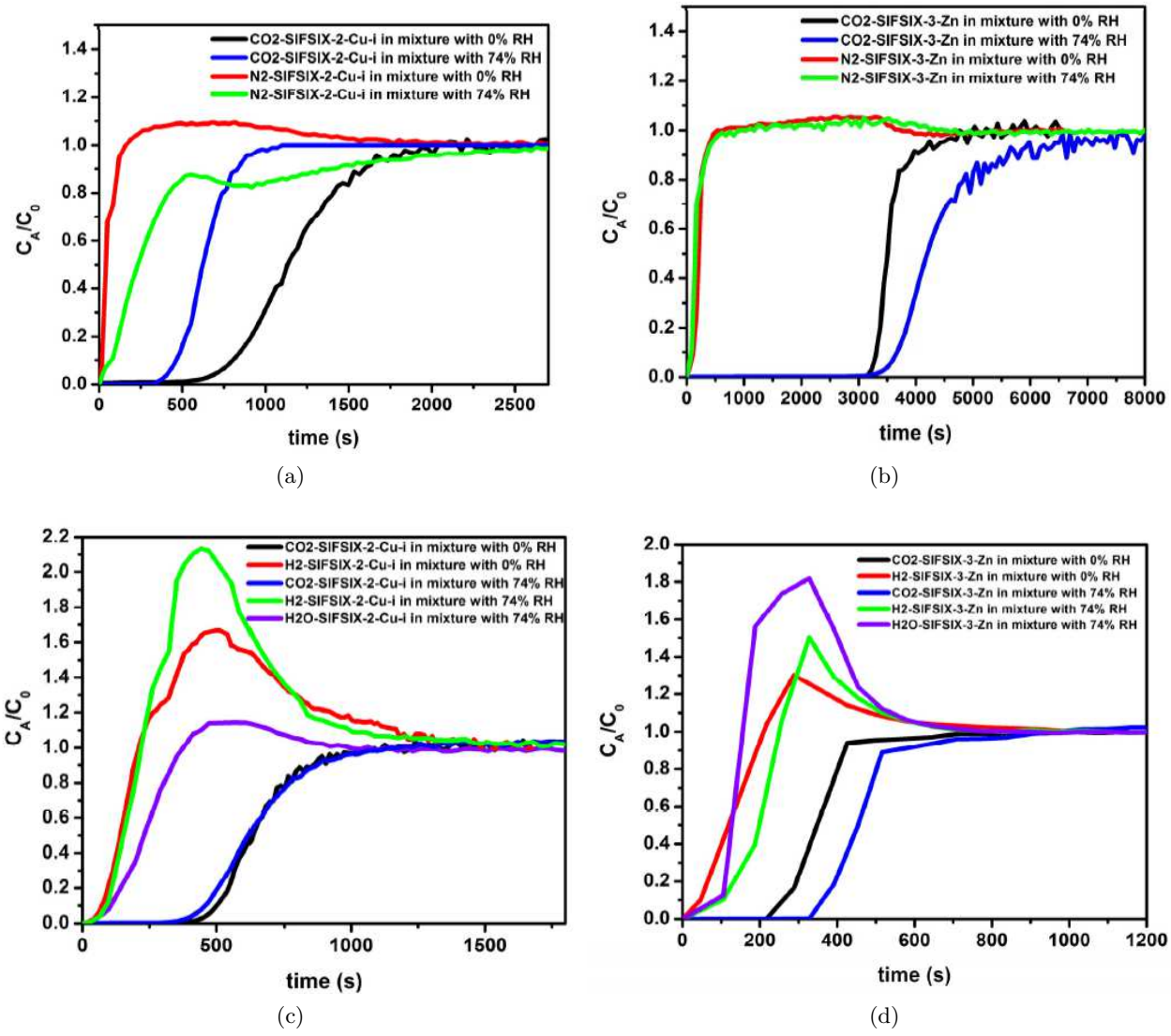

Figure 4.3: Experimental breakthrough curves presented by Nugent et al. for 10% CO_2, 90% N_2 at 0% and 74% R.H. for (a) SIFSIX-2-Cu-i and (b) SIFSIX-3-Zn and for 30% CO_2, 70% H_2 at 0% and 74% R.H. for (c) SIFSIX-2-Cu-i and (d) SIFSIX-3-Zn [5] - Supplementary Information. Reprinted by permission from Macmillan Publishers Ltd: Nature, [5],Copyright 2013

and SIFSIX-3-Zn. Additionally, the CO_2 breakthrough occurs at the same time for the dry and wet cases for SIFSIX-2 and for SIFSIX-3 the wet CO_2 breakthrough occurs later than the dry CO_2 breakthrough, perhaps indicating that the adsorbent has more CO_2 adsorption capacity in the presence of water. In summary, the experimental breakthrough results of Nugent et al. show that CO_2 adsorption is not harshly affected by the presence of water vapor for SIFSIX-2-Cu-i and SIFSIX-3-Zn.

4.4 SIFSIX Model Validation - Breakthrough Simulations

In order to validate that the model parameters are correct, breakthrough simulations were performed based on the dimensions of the column reported in the literature and with the fitted isotherm parameters. The relevant column and adsorbent parameters used for these breakthrough simulations are presented in Table 4.2. All known details of the experimental system provided in the supplementary information of the literature is maintained in the simulation, specifically the column dimensions, temperature, pressure and inlet velocity of gas mixture [5]. The specific heat capacity, as well as the heat transfer coefficient inside the column was assumed to be similar to that of Zeolite 13X, in the absence of literature data.

Table 4.2: SIFSIX-2-Cu-i and SIFSIX-3-Zn column and adsorbent parameters

Property	Value
Bed Length, L [m]	0.027
Column inside radius, r_i [m]	0.004
Column outside radius, r_o [m]	0.0067
Bed voidage ε	0.37
Particle voidage ε_p	0.35
Molecular diffusivity at 1 atm and 298 K, D_M [m^2/s]	1.2955 x 10^{-5}
Specific heat capacity of the gas mixture, C_{pg} [J/kgK]	1010.6
Specific heat capacity of the adsorbent, C_{ps} [J/kgK]	1070.0
Specific heat capacity of the adsorbed phase, C_{pa} [J/kgK]	1070.0
Specific heat of the column wall, C_{pw} [J/kgK]	502.0
Viscosity of gas mixture, μ [kg/m/s]	1.72 x 10^{-5}
Inside heat transfer coefficient, h_i [W/m^2K]	8.6
Outside heat transfer coefficient, h_o [W/m^2K]	2.5
Thermal conductivity of gas mixture, k_z [W/m K]	0.0903
Thermal conductivity of column wall, k_w [W/m K]	16
Adsorbent particle density, ρ_s [kg/m^3]	1423
Column wall density, ρ_w [kg/m^3]	7800
Universal gas constant. R [m^3Pa/K mol]	8.314

The experimental and simulated breakthrough curves of carbon dioxide in a 10% CO_2 and 90% N_2 mixture on SIFSIX-2-Cu-i and SIFSIX-3-Zn are presented in Figures 4.4 and 4.5,

respectively. Both breakthrough simulations correspond to a 0.1 bar partial pressure of CO_2, which by the single component isotherm corresponds to a CO_2 loading of 1.5 mmol/g for SIFSIX-2-Cu-i and 2.3 mmol/g for SIFSIX-3-Zn. This difference in loading is also present in the breakthrough which is why the area behind the breakthrough curve in Figure 4.5 is larger than that in Figure 4.4. The breakthrough curves incorporating a wet feed were not able to be simulated, due to the lack of multicomponent adsorption isotherms, particularly for water vapor and CO_2 mixtures. In the absence of such data, it is not be possible to quantify and model the effect of water on the adsorption of CO_2 and N_2. Hence, all simulations in this chapter were performed under dry conditions.

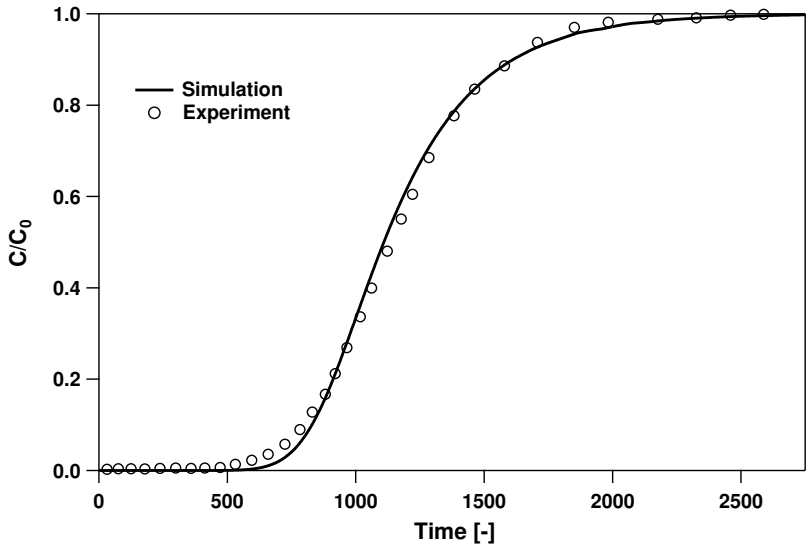

Figure 4.4: Simulation and Experimental CO_2 Breakthrough curves on SIFSIX-2-Cu-i MOF, for a breakthrough experiment carried out with 10% CO_2 and 90% N_2 in the absence of water. Experimental data obtained from the supplementary data of Nugent et al. [5]

4.5 Multiobjective Optimization - SIFSIX Adsorbents

VSA cycle simulations were carried out with the adsorbent and column properties listed in Table 4.2, except for the column dimensions, which are changed to a 1 m long adsorption column, with an inside radius of 0.162 m and an outside radius of 0.199 m. The cycle configuration used is the 4 step VSA cycle with LPP.

In all optimizations, the decision variables are the same. These are the cycle step times (t_{ads},t_{blow},t_{evac}), P_{INT}, P_L, and the inlet velocity, v_0. The time of the pressurization step is kept constant at 20 s. The range of decision variables used for optimizations is presented in Table 4.3. An inequality constraint is imposed on the values of the blowdown and evacuation

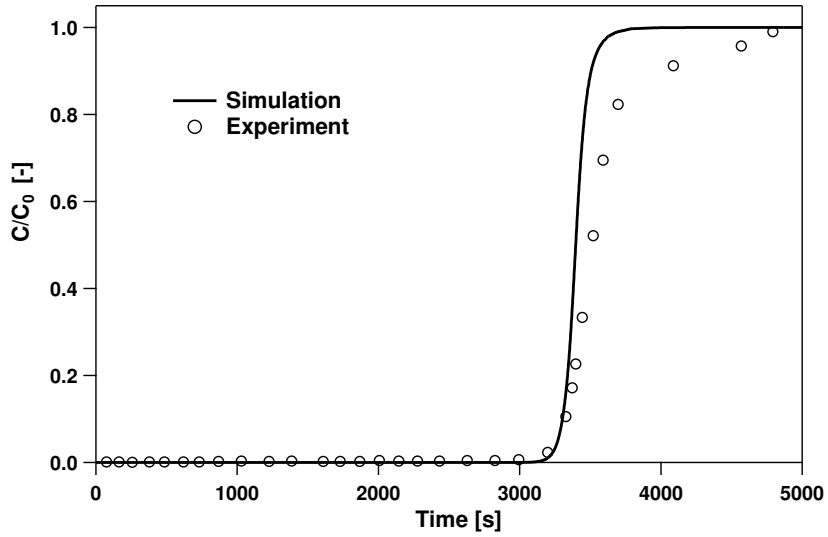

Figure 4.5: Simulation and Experimental CO_2 Breakthrough curves on SIFSIX-3-Zn MOF, for a breakthrough experiment carried out with 10% CO_2 and 90% N_2 in the absence of water. Experimental data obtained from the supplementary data of Nugent et al. [5]

pressures, such that the evacuation pressure is always lower than the blowdown pressure. This constraint is given in Equation 4.4 .

$$P_{INT} \geq P_L + 0.01 \tag{4.4}$$

The decision variable range is supplied to the genetic algorithm optimization routine in MATLAB, with a population of 144 sets of decision variables per generation. A generation is the population of combinations of the decision variables which the genetic algorithm supplies to the model in order to evaluate the values of the objective functions.

Table 4.3: Range of decision variables used in optimization

Decision Variable	t_{ads}[s]	t_{blow}[s]	t_{evac}[s]	P_{INT}[bar]	P_{L}[bar]	$v0$[m/s]
Lower Bound	20	30	30	0.03	0.03	0.1
Upper Bound	100	200	200	0.5	0.5	2

4.5.1 Purity and Recovery Optimization

Purity and Recovery optimization is performed to determine whether there is any advantage in the raw performance of SIFSIX MOFs compared to zeolite 13X in terms of these two performance indicators. The target performance set for post-combustion CO_2 capture in this case is 90% purity and 90% recovery. The genetic algorithm was initiated with decision variable bounds specified in Table 4.3. The results obtained from the genetic algorithm

contains the decision variables, values of purity, recovery, energy and productivity, as well as the mass balance which is used to verify whether CSS has been achieved for all of the simulations. Based on this data, a scatter plot of all of the purity and recovery values obtained from simulations can be done, as shown in Figure 4.6. Each of the grey points represents the purity and recovery of a simulation ran to CSS through the optimization procedure described. The black points represent conditions where neither the purity nor the recovery can be further increased without negatively impacting the other. That is, each point represents a simulation where the decision variables have resulted in maximum purity or recovery. This is called a pareto curve, and it follows that the ideal operating conditions for the maximization of purity and recovery are those corresponding to the points in the upper right of this curve.

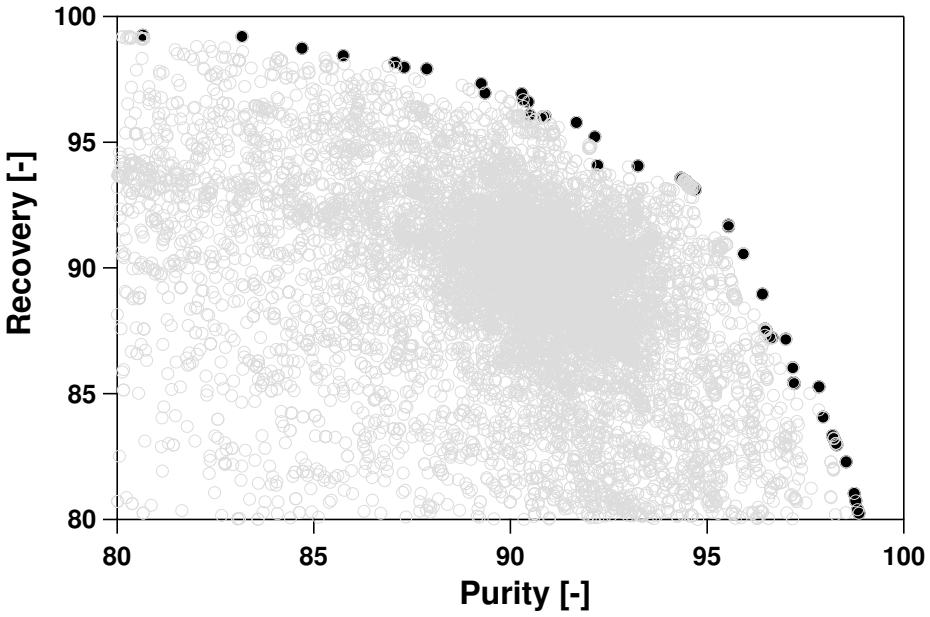

Figure 4.6: Illustration of a Pareto Curve. All points on the plot are purity and recovery values obtained for a PSA cycle with specific operating conditions. Grey markers indicate suboptimal points and black markers indicate the optimal pareto points.

The pareto curve obtained from the purity-recovery optimization of the SIFSIX adsorbents are presented and compared to the same found in literature [10], [25] in Figure 4.7. Based on this optimization, there is not much distinction between the performance of zeolite 13X, SIFSIX-2-Cu-i and SIFSIX-3-Zn. At a constant recovery of 90% for example, the difference in performance is marginal, within a range of approximately 1-2% purity. It is clear from the plot, however, that the SIFSIX MOFs are capable of achieving performance in excess of 90% purity and recovery.

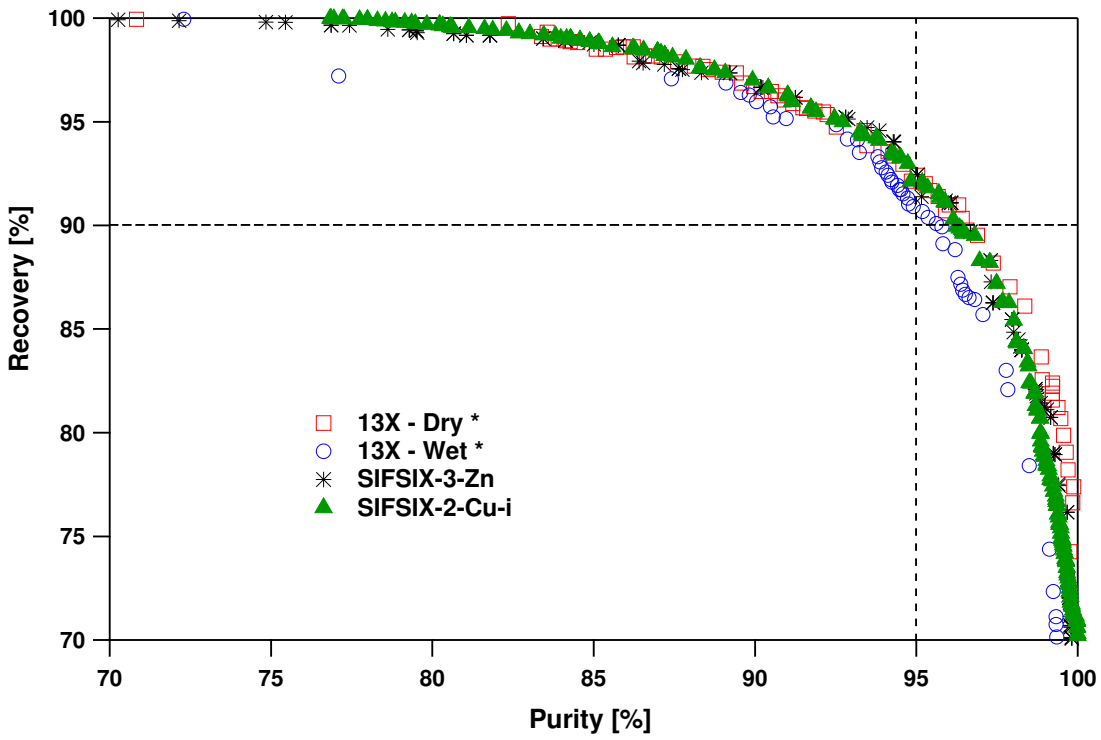

Figure 4.7: Purity-Recovery Paretos of SIFSIX-2-Cu-i, SIFSIX-3-Zn and Zeolite 13X

The values of the blowdown and evacuation pressures corresponding to the purity and recovery pareto points are shown in Figure 4.8. For both adsorbents, as P_{INT} increases the general trend is that purity decreases while recovery increases. Purity decreases due to more N_2 remaining in the bed at higher intermediate pressures, while recovery increases because less CO_2 is lost from the blowdown step at a higher blowdown pressure. With this information, however, an evaluation of the effectiveness of these MOFs for CO_2 separation from flue gas cannot be complete. Therefore, an energy productivity optimization should follow, which allows for the ranking of the adsorbents based on the minimum energy requirements and maximum productivity of each, provided that the performance of the VSA cycle is satisfactory.

4.5.2 Energy-Productivity Optimization

Energy and Productivity optimization is performed in order to estimate the minimum energy required for 90% purity and recovery of the adsorbent being evaluated as well as the maximum possible productivity. Since it is determined that the SIFSIX adsorbents can meet the DOE purity and recovery performance for CO_2 capture systems, it is also important now to estimate the cost of a 4-step VSA cycle with these adsorbents. The energy

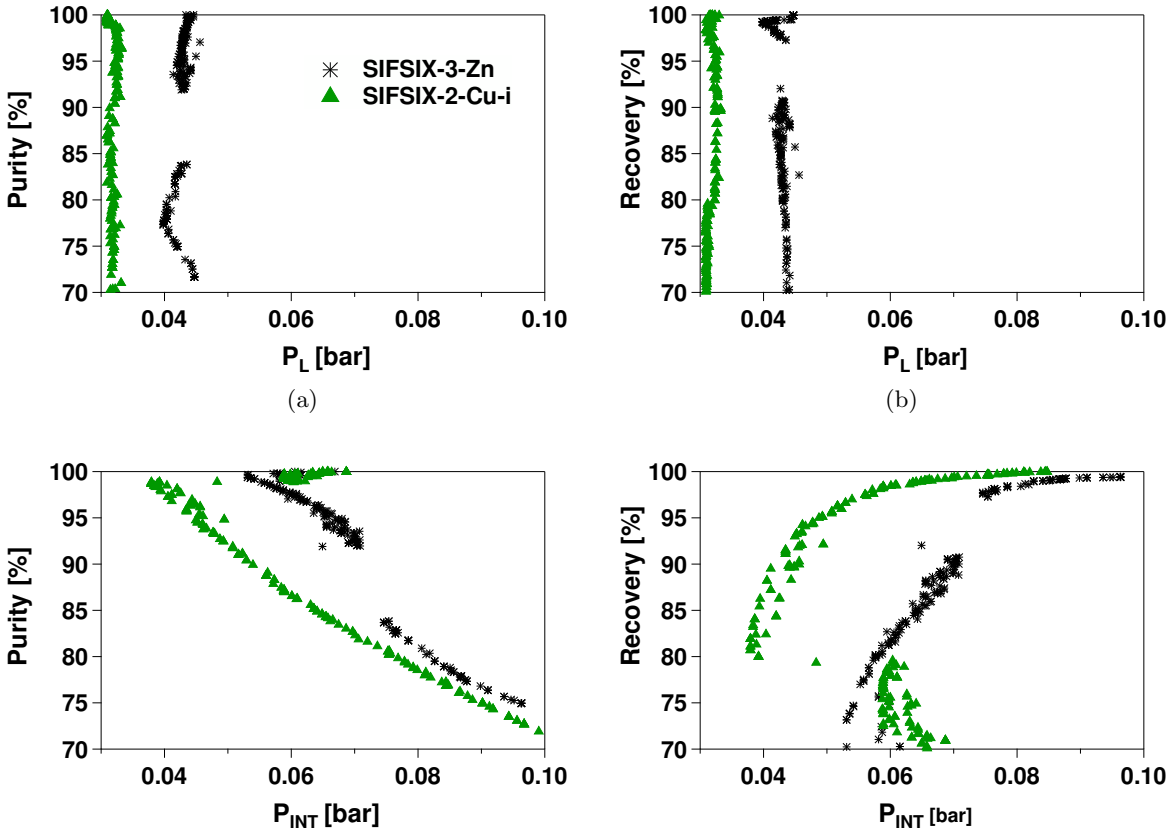

Figure 4.8: Pressures of the evacuation steps corresponding to (a)Purity and (b)Recovery and pressures of the blowdown steps corresponding to (c)Purity and (d)Recovery for the pareto curve presented in Figure 4.7.

performance of the VSA cycle is of importance because the energy requirement is directly related to the operating cost of the CO_2 capture process. The productivity is a measure of the amount of CO_2 which can be extracted for a given volume of adsorbent per unit time, which is effectively can be used to estimate the sizing and capital costs of the VSA cycle. An energy and productivity optimization with the SIFSIX MOFs will therefore be useful in determining whether these MOFs are economically more or less viable than Zeolite 13X for post-combustion capture.

The optimization is performed with the same bounds on the decision variables as described in the previous section, however, the objective functions are constrained such that the 90% purity and recovery constraint is met. In addition to these details, it was also important to ensure that every region of the decision variables, particularly the step times for adsorption, blowdown and evacuation, were thoroughly searched by the GA optimizer. This was done by splitting the search region of these three step times in two, a high time region and a low time region, and running optimization routines with different combinations of these high and low routines for the step times, t_{ads},t_{blow} and t_{evac}. The decision variables resulting in an energy and productivity pareto were then used as a seed for a final optimization, using the entire search region for step times.

The energy productivity pareto for the SIFSIX adsorbents compared to that of zeolite 13X is presented in Figure 4.9. The energy consumption for the SIFSIX-2-Cu-i adsorbent is comparable to that of Zeolite 13X, with a slightly higher productivity. SIFSIX-3-Zn has a notably lower productivity, however, which is comparable to that of Zeolite 13X with wet flue gas. The reason for this significant decrease in productivity is due to the very sharp isotherm of CO_2 on SIFSIX-3-Zn. The isotherm at 25°C results in a very low working capacity, as a pressure swing from 0.15 bar at the adsorption step to 0.027 bar (assuming an evacuation step with P_L=0.03 bar and 90% pure CO_2) corresponds to a change in loading from 2.4 mmol/g to 2.1 mmol/g. Productivity is determined by the ratio of the moles of CO_2 extracted per cycle to the product of the volume of adsorbent required and the cycle time. Therefore, the small working capacity for CO_2 is detrimental for the productivity of the process, even if the selectivity reported for the adsorbent is very high.

The blowdown and evacuation pressures for each pareto point in Figure 4.9 is plotted with the corresponding energy requirement for the cycle in Figure 4.10. The general trend is that energy decreases with increasing blowdown and evacuation pressures for both adsorbents. In the case of SIFSIX-3-Zn, a minimum energy of 140 kWh/t CO_2 was attainable, with a P_{INT} of 0.12 bar. For SIFSIX-2-Cu-i, a minimum energy of 155 kWh/t CO_2 was possible

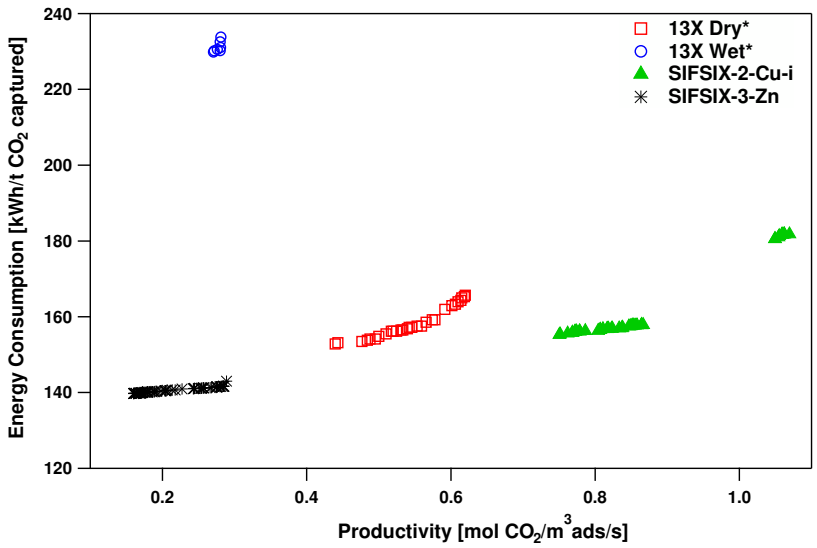

Figure 4.9: Energy-Productivity Paretos SIFSIX-2-Cu-i and SIFSIX-3-Zn compared to Zeolite 13X [10] satisfying 90% purity and recovery

with a lower P_{INT} at 0.11 bar. For both adsorbents, the same trend is observed with the evacuation pressure, P_{L}, however the value of this decision variable must be close to the lower bound of 0.03 bar to maintain a purity and recovery of 90%. For both SIFSIX adsorbents, the operating conditions corresponding to the minimum energy observed are given in Table 4.4.

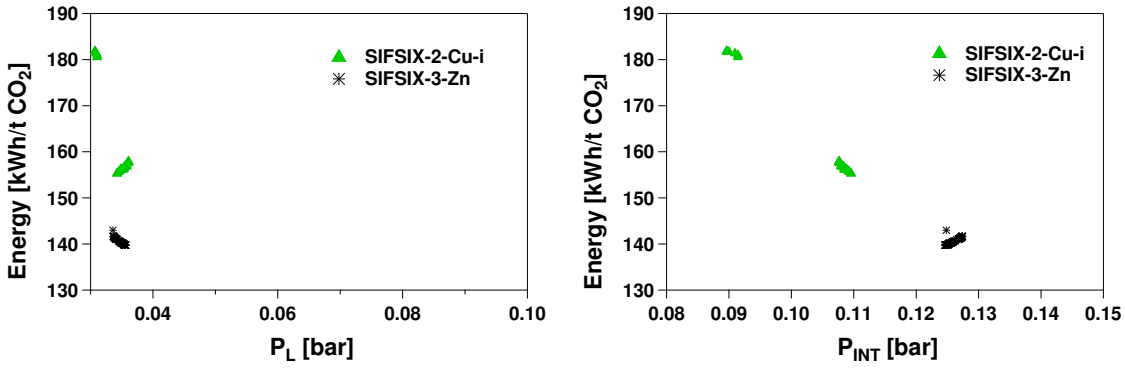

(a) (b)

Figure 4.10: Pressures of (a)evacuation and (b)blowdown steps corresponding to the pareto curves in Figure 4.9

For further clarification and analysis, the detailed simulation results for the optimized cycle, the operating conditions for which are provided in Table 4.4 will also be discussed. Solid and gas phase CO_2 profiles obtained from the simulation at cyclic steady state are plotted

Table 4.4: Operating parameters of 4 step cycle with LPP corresponding to minimum energy for SIFSIX adsorbents

Adsorbent	t_{ads}[s]	t_{blow}[s]	t_{evac}[s]	P_{INT}[bar]	P_{L}[bar]	$v0$[m/s]	Energy[kWh/t]
SIFSIX-2-Cu-i	81.05	67.02	89.56	0.11	0.034	0.73	155.2
SIFSIX-3-Zn	87.72	80.34	148.53	0.12	0.036	0.19	139.7

axially along the length of the column. These profiles are plotted in Figure 4.11. The dimensionless bed length represents the length along the column, with 0 being the inlet and 1 being the outlet. Both simulations result in 90% purity and recovery, supported by the fact that in the adsorption and blowdown steps the CO_2 mole fractions at the outlet end are very low. The CO_2 front is retained in the column and loss in both of these steps is minimal. Furthermore, the composition of CO_2 at the beginning and end of the evacuation step is 0.9 for SIFSIX-2-Cu-i and SIFSIX-3-Zn, indicating the high purity. In the solid phase, there is a significant difference between the profiles of SIFSIX-2-Cu-i and SIFSIX-3-Zn. The CO_2 extract is withdrawn from the inlet of the column during the evacuation step, therefore the difference between the CO_2 loading at the end of the blowdown and evacuation steps in Figure 4.11(b) and 4.11(d) is the amount of CO_2 extracted in the evacuation step. Qualitative inspection of these two figures show that the quantity of CO_2 extracted from the SIFSIX-3-Zn simulation is much less than that of the SIFSIX-2-Cu-i. In addition, the cycle time for minimum energy for the SIFSIX-3-Zn adsorbent is higher than that for SIFSIX-2-Cu-i, particularly in the evacuation step. Therefore, the most important factors in determining productivity are the moles of CO_2 extracted in the evacuation step and the cycle time. Based on the profiles in Figure 4.11 and the data in Table 4.4, the productivity of SIFSIX-3-Zn will be lower because of the higher cycle time and the lower working capacity.

4.6 Summary

The experimental adsorption equilibrium data reported by Nugent et al. [5] was incorporated into a full PSA model in order to evaluate their potential for adsorptive post combustion CO_2 capture. In summary, SIFSIX metal-organic frameworks have been shown to meet the CO_2 capture performance, with purity and recovery exceeding 90% with a 4-step VSA cycle with LPP. Furthermore, there was no distinguishable difference between these MOFs and Zeolite 13X by performance in terms of the purity and recovery obtained. When a constrained energy-productivity optimization was performed, the results indicated that

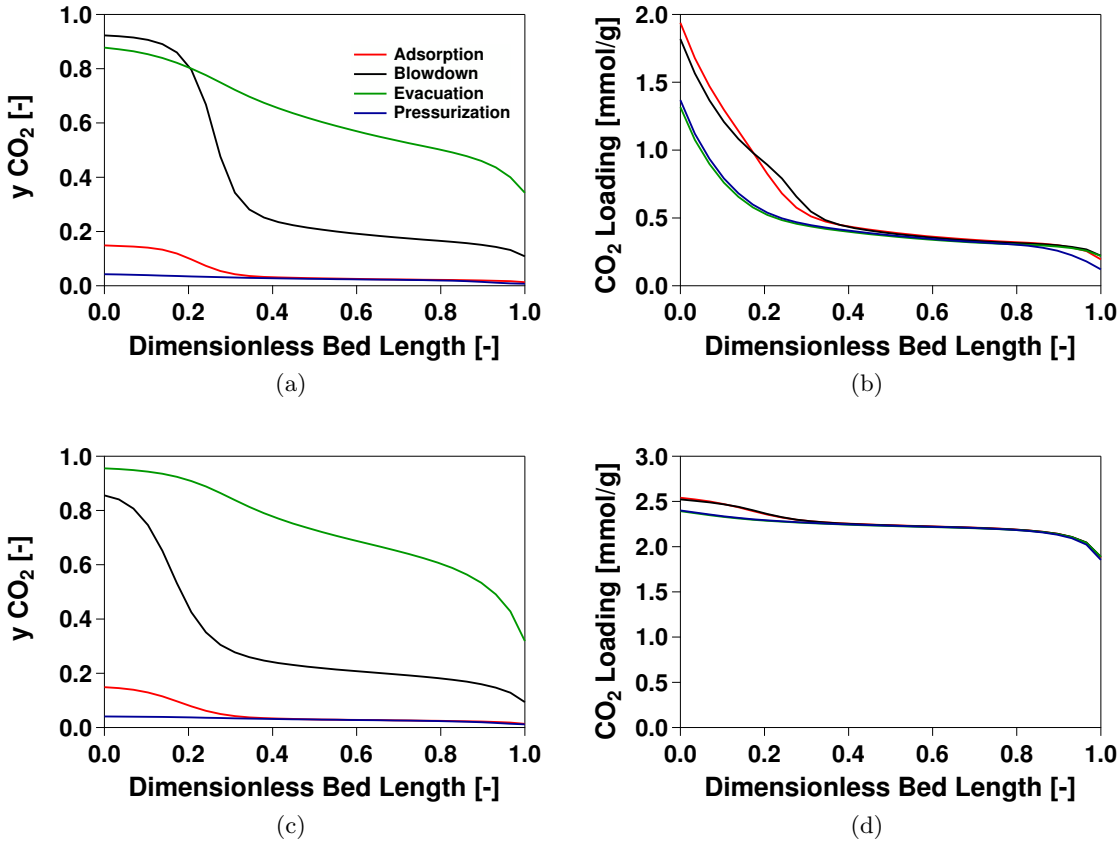

Figure 4.11: Axial profiles of CO_2 for a 4-step LPP cycle corresponding to minimal energy for SIFSIX-2-Cu-i in a.)gas phase and b.)solid phase and for SIFSIX-3-Zn in a.)gas phase and b.)solid phase

SIFSIX-2-Cu-i offers no substantial advantage in terms of energy compared to 13X but has a slightly higher productivity. SIFSIX-3-Zn had significantly lower productivity, with energy slightly lower than that of SIFSIX-2-Cu-i. The effect of moisture on an adsorption cycle was not able to be studied due to the lack of experimental multiple component data. However, based on the dry feed of carbon dioxide and nitrogen, it is clear that SIFSIX-2-Cu-i is the only viable alternative to 13X, having similar performance in terms of energy and productivity. SIFSIX-3-Zn is not viable due to having significantly lower productivity than both Zeolite 13X and SIFSIX-2-Cu-i. An additional fact to take into consideration is that crystal properties of the SIFSIX MOFs were used for this study in the absence of data. A reduction in the density of the SIFSIX MOFs in simulations is expected to result in reduced productivity and vice-versa. Therefore, considering that there is only a marginal improvement in SIFSIX-2-Cu-i performance over Zeolite 13X in an ideal case, and that SIFSIX-3-Zn is ruled out due to significantly lower productivity, the SIFSIX MOFs are not expected to be a practically feasible alternative to Zeolite 13X.

Chapter 5

Evaluation of Diamine-Appended Metal-Organic Frameworks for Post-Combustion CO_2 Capture

5.1 Properties of Diamine-Appended MOFs

Very recently, several publications have shown metal-organic frameworks with high selectivity and capacity for carbon dioxide at low partial pressures. The first of these metal-organic frameworks is Mg_2(dobpdc), functionalized with N,N' - dimethylethylenediamine (mmen). The resulting adsorbent displayed a previously unexplained step-shaped CO_2 adsorption isotherm, meaning that there is a sudden rise in adsorption capacity after a threshold or step pressure, at a given temperature. McDonald et al. have synthesized several variants of the mmen-Mg_2(dobpdc) adsorbent, by replacing the Mg^{2+} ions with other divalent metal ions, specifically Mn_2,Fe_2,Co_2, Ni_2 and Zn_2, with the intention of changing the strength of the metal-amine bond in the MOF structure [6]. The adsorption mechanism responsible for the step-change or S-shaped CO_2 isotherm is referred to as a cooperative insertion. Adsorption of a small number of CO_2 atoms is reported to destabilize the metal-amine bonds, with the CO_2 atom being inserted between the M-N bond. Destabilization of subsequent M-N bonds makes CO_2 insertion into the metal-amine bond easier, resulting in the sharp or sudden increase in the adsorption capacityof CO_2 observed once sufficient CO_2 atoms are present, i.e. once the CO_2 partial pressure is greater than or equal to the threshold/step pressure [6], [22].

The adsorption isotherms of the different metal-exchanged forms of the mmen-MOFs were measured experimentally by McDonald et al. at temperatures of 25, 40, 50 and 75°C [6]. These isotherms are presented in Figure 5.1. For post-combustion CO_2 capture, the feed composition of CO_2 is assumed to be 15%, corresponding to a pressure of 150mbar on the

plot. This means that in consideration of one or more of these adsorbents for VSA, the step change at 25°C must occur before 150mbar on the isotherm. An additional consideration is that the step change must happen after 3kPa or 30mbar, as this is practically the lower end of vacuum pressure that can be used industrially. Based on these considerations, mmen-Fe_2 and mmen-Zn_2 are able to be used for the purpose of VSA. The potential advantage that this MOF may have with respect to VSA separation of CO_2 and N_2 is the accessible working capacity with potentially higher P_L. The nitrogen isotherm at 25°C was the only one available in literature, and is linear.

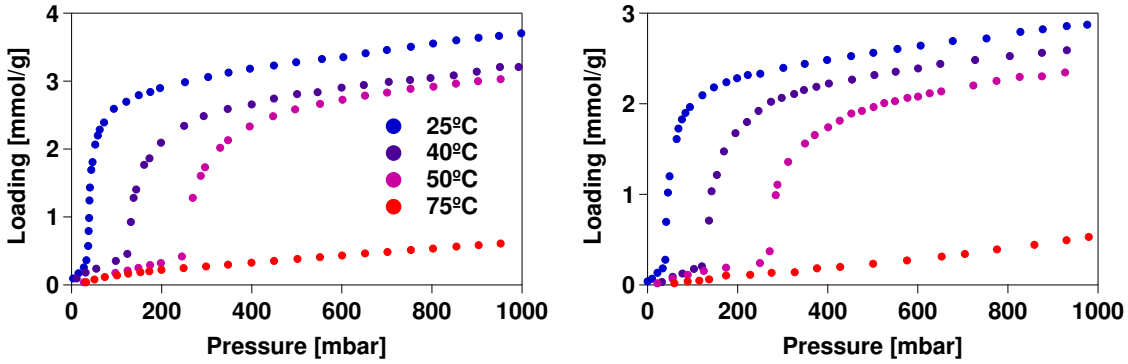

(a) (b)

Figure 5.1: Experimental adsorption isotherms of CO_2 on diamine-appended MOFs (a)mmen-Fe_2 and (b)mmen-Zn_2 [6]. blue-25°C, purple-40°C,violet-50°C,red-75°C

5.2 Modeling S-shaped Isotherms

5.2.1 General Features of Isotherm

All of the adsorption isotherms previously discussed are classified as type I isotherms. This means that as pressure increases the adsorption capacity increases monotonically until it reaches a saturation capacity. Depending on the nonlinearity of the isotherm, the first derivative of a type I isotherm is positive and constantly decreasing until it approaches the saturation capacity. The second derivative is therefore negative and constantly increasing, approaching zero. The S-shaped isotherms shown in Figure 5.1 are classified as type V. These isotherms have one or more inflection points, where the second derivative goes from positive to negative or vice versa. In the case of the diamine-appended mmen-MOFs the isotherms have one inflection point which occurs at the middle of the step change, where the first derivative of the adsorption isotherm hits a local maxima.

5.2.2 Selection of an Isotherm Model

The equation used to model an adsorption isotherm should reflect most of its features, which includes matching the experimental loading at the corresponding partial pressure, and the inflection points in the case of the S-shaped isotherms. For a type I isotherm, the simplest model aside from a linear model is a single-site Langmuir model. As mentioned previously, the first derivative of a type I isotherm is positive and decreasing, approaching zero and the second derivative, negative and increasing approaching zero. The Langmuir equation is presented in Equation 5.1.

$$q_i^* = \frac{q_{si} b_i C_i}{1 + b_i C_i} \tag{5.1}$$

The first derivative of the Langmuir model equation is given in Equation 5.2. It is clear based on this equation that as concentration increases the value of dq/dC becomes closer to zero.

$$\frac{dq_i}{dC} = \frac{q_{si} b_i}{1 + b_i {C_i}^2} \tag{5.2}$$

The second derivative has a negative term in the numerator, therefore it is constantly negative and as C increases, it approaches zero, similar to the first derivative. The value of the second derivative is never positive, therefore it is a model which is unable to capture the inflection point which is the key feature of the diamine-appended MOFs.

$$\frac{dq_i}{dC} = \frac{-2 q_{si} b_i^2 (1 + C_i)}{(1 + b_i C_i)^4} \tag{5.3}$$

The adsorption isotherms of carbon dioxide on the diamine-appended metal organic frameworks are S-shaped, having an anti-Langmurian shape at low partial pressures, followed by an almost vertical step increase in loading, then ends with a favorable shape. For this type of isotherm shape, it is recommended to use a second-order isotherm, such as the quadratic isotherm [34]. The general form of this isotherm is presented in Equation 5.4. The isotherm consists of three fitted parameters, compared to the two for a single site Langmuir isotherm model.

$$q_i^* = \frac{q_{s1i} (b_{1i} C_i + 2 b_{2i} C_i^2)}{1 + b_{1i} C_i + b_{2i} C_i^2} \tag{5.4}$$

The second derivative of the quadratic isotherm model is given in Equation 5.5. A second derivative of the third order indicates that there are 3 potential solutions to the equation, so the quadratic isotherm can have 0-3 inflection points, based on the values of the fitted

isotherm parameters.

$$\frac{d^2q}{dC_i^2} = \frac{2(2b_{2i} - b_{1i}^2) - 6b_{1i}b_{2i}C_i - 12b_{2i}^2C_i^2 - 2b_{1i}b_{2i}^2C_i^3}{(1 + b_{1i}C_i + b_{2i}C_i^2)^3} \tag{5.5}$$

Another model considered is the Rutherford cooperative multimolecular sorption (CMMS) model, used to describe type V isotherms such as water on microporous carbon molecular sieves and activated carbon [35], [4]. The model considers a cooperative effect in which adsorbed molecules promotes the adsorption of additional molecules onto adjacent adsorption sites, comparable to the proposed mechanism by McDonald et al. Other adsorption isotherm models tested are several variants of the quadratic isotherm model. All of the equations of the isotherm models considered for modeling PSA with the mmen-Fe_2 adsorbent can be found in Table 5.1. Temperature dependence for each of these models is incorporated using an Arrhenius correlation for the adsorption affinity term, given in Equation 5.6.

$$b_i = b_{0i}\exp\frac{\triangle U}{RT} \tag{5.6}$$

Table 5.1: Type V Adsorption Isotherm Models

Model	Equation
Quadratic Isotherm	$q_i^* = \frac{q_{s1i}(b_{1i}C_i + 2b_{2i}C_i^2)}{1 + b_{1i}C_i + b_{2i}C_i^2}$
Quadratic-Langmuir	$q_i^* = \frac{q_{s1i}(b_{1i}C_i + 2b_{2i}C_i^2)}{1 + b_{1i}C_i + b_{2i}C_i^2} + \frac{q_{s2i}d_iC_i}{1 + d_iC_i}$
Rutherford CMMS	$q_i^* = \frac{q_{s1i}b_{0i}C_i}{b_{0i}C_i + w^2} + \frac{q_{s2i}b_{2i}C_i}{1 + b_{2i}C_i}$
Rutherford CMMS	$w = \frac{1}{2}\left(1 - b_{1i}C_i + \sqrt{[1 - b_{1i}C_i]^2 + 4b_{0i}C_i}\right)$
Freundlich-Langmuir	$q_i^* = \frac{q_{s1i}b_{1i}C_i^n}{1 + b_{1i}C_i^n}$
Modified Freundlich-Langmuir (2 terms)	$q_i^* = \frac{q_{s1i}(b_{1i}C_i + b_{2i}C_i^n)}{1 + b_{1i}C_i + b_{2i}C_i^n}$

Several criteria were considered for the selection of a model. The first is the CO_2 fit in the low and high pressure regions, as it is essential that model calculation of CO_2 loading in the 0 to 0.15 bar range is accurate. This includes the presence of the inflection point in the model. Another factor is the fitting of isotherms at multiple temperatures. Experimental multiple component adsorption equilibrium data is unavailable in literature, so it is important to estimate multiple component adsorption by the ideal adsorbed solution theory (IAST) and

estimate if each model can be modified to take into account the effects of competitive adsorption of CO_2 and N_2. Assuming that the single component loading calculated by the model for CO_2 and N_2 fit the experimental data well, the competitive adsorption is the most important factor in deciding the model that is to be chosen, due to it affecting the process performance based on purity and recovery.

Fitting of single component experimental data to the various models presented in Table 5.1 was in principle similar to the procedure used to fit the previous isotherms. First, each model was fitted to the experimental data for a temperature of 25°C, by using the fmincon routine in matlab to minimize the objective function presented in Equation 5.7.

$$\text{MinJ1} = \sum_{\text{P}} \frac{|\text{q}_{\text{exp}} - \text{q}_{\text{model}}|}{\text{q}_{\text{exp}}} \tag{5.7}$$

The starting guess provided to the fmincon routine was generated using a different procedure. A latin hypercube sampling (LHS) method was used to generate 5×10^4 sets of isotherm parameters, with the objective function in Equation 5.7 being evaluated for each. The set of LHS-generated isotherm parameters corresponding to the minimum value of this objective function is then used as an initial guess in fmincon. Once the first temperature is fitted, the temperature dependence is then considered by implementation of the temperature dependence term, and changing the objective function to Equation 5.8.

$$\text{MinJ2} = \sum_{\text{T}} \sum_{\text{P}} \frac{|\text{q}_{\text{exp}} - \text{q}_{\text{model}}|}{\text{q}_{\text{exp}}} \tag{5.8}$$

The Rutherford CMMS was the only model which could satisfactorily fit the experimental data with a common set of isotherm parameters for multiple temperatures. All the other models were fitted for each temperature, with the same value of the saturation loading q_s, but different values of the adsorption affinity parameter, b_i. For each of the models considered, the fitted isotherm and the corresponding experimental data points are presented in Figure 5.2. Based on the model fitting to the experimental data, only the quadratic-langmuir and Rutherford CMMS models can accurately model the loading over the entire range of experimental data. The remaining two models cannot accurately model the high pressure isotherm data because these approach the saturation loading, or q_s, value and do not increase afterward. Additionally, the Langmuir-Freundlich isotherm cannot accurately model data at low pressures due to the $b_i C_i^n$ term in the numerator of the model equation. Isotherm parameters for each of the models is presented in Table 5.2, for the fittings at 298K. Based on the CO_2 single component isotherm fits, only the Quadratic-Langmuir and

Rutherford CMMS models will be considered further.

Table 5.2: Fitted isotherm parameters for CO_2 on mmen-Fe_2 at 298K. The Rutherford CMMS model fitted parameters are valid for multiple temperatures.

Parameter	Quad. Lang	CMMS	Lang.-Freundlich	Mod. Lang.-Freundlich
qs_1 [mmol/g]	0.2972	1.855	2.6979	2.7097
qs_2 [mmol/g]	3.275	2.343	-	-
b_1 [m^3/mol]	-1.124	1.09×10^{-13}	1.83×10^{-2}	6.29×10^{-3}
b_2 [m^3/mol]	0.374	5.39×10^{-12}	-	8.34×10^{-2}
d_1 [m^3/mol]	0.252	9.43×10^{-8}	-	-
$\triangle Ub_1$ [kJ/mol]	-	-58.867	-	-
$\triangle Ub_2$ [kJ/mol]	-	-63.140	-	-
$\triangle Ud_1$ [kJ/mol]	-	-33.702	-	-
n	-	-	7.4657	9.052

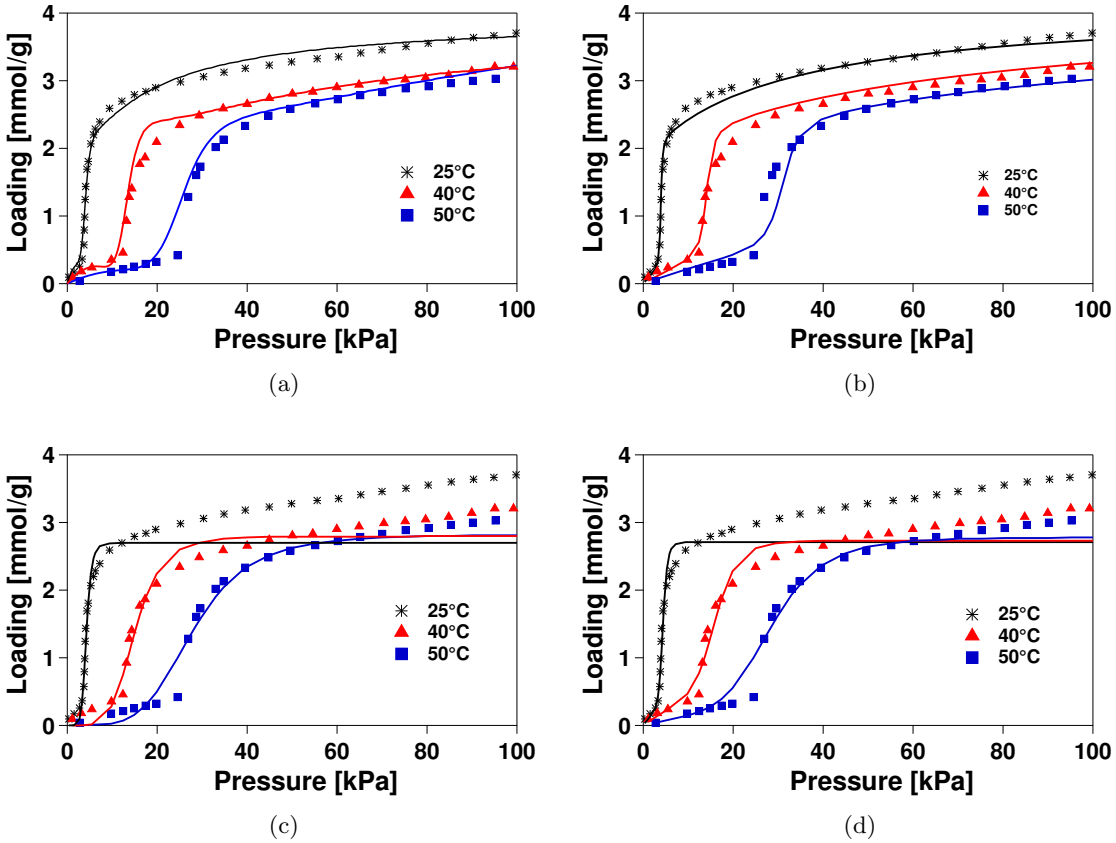

Figure 5.2: CO_2 adsorption isotherm experimental data of McDonald et al. [6] fit to: a.)Quadratic-Langmuir b.)Rutherford CMMS c.)Langmuir-Freundlich and d.)Modified Langmuir-Freundlich isotherm models

Multiple component adsorption is also important in model selection. In this case, a CO_2 and N_2 binary gas mixture is being considered as a flue gas mixture. There are limited competitive isotherm models which are explicit and also applicable to type V isotherms

in literature. Ilic et al present an ideal adsorbed solution theory (IAST) derived explicit competitive isotherm model for a binary system but this is only applicable to second-order models [36]. This is only applicable to the quadratic-langmuir isotherm. Due to the nature of PSA simulations being cyclic and requiring the solution of a system of PDEs many times in optimization, a direct implementation of the IAST equations is impractical. Therefore, the quadratic-langmuir isotherm model will be the only model considered for further analysis, due to the Rutherford CMMS model having no extended form to account for multiple component adsorption. To evaluate the accuracy of the extended quadratic langmuir model, the calculated loadings of different mixtures of CO_2 and N_2 will be compared to the solution using the IAST. The carbon dioxide isotherm at 25°C is modeled by the quadratic-langmuir equation, and nitrogen is modeled using a single-site langmuir equation, fitted to the experimental data of McDonald et al. [22]. Fitting was done by the same procedure as described for previous type I isotherms, such as CO_2 on SIFSIX adsorbents. In the absence of multiple temperature data, the free energy of adsorption, $\triangle U$, is assumed to be equivalent to that of SIFSIX-2-Cu-i. The fitted parameters for N_2 can be found in Table 5.3. The experimental data points and the Langmuir fitted model for N_2 at 25°C are presented in Figure 5.3.

Table 5.3: Langmuir isotherm model parameters fitted for N_2 on mmen-Fe_2

Isotherm Model Parameter	Value
q_s [mmol g^{-1}]	3.65
b_0 [m^3 mol^{-1}]	2.69 $\times 10^{-5}$
$\triangle U$ [kJ mol^{-1}]	8.374

The extended forms of the quadratic-Langmuir and Langmuir equations used to the model CO_2 and N_2 binary loadings respectively, are provided in Equations 5.9 and 5.10.

$$q_{CO_2} = \frac{q_{s1CO_2}(b_{1CO_2}C_{CO_2} + 2b_{2CO_2}C_{CO_2}^2)}{1 + b_{1CO_2}C_{CO_2} + b_{2CO_2}C_{CO_2}^2} + \frac{q_{s2CO_2}d_{CO_2}C_{CO_2}}{1 + d_{CO_2}C_{CO_2} + b_{N_2}C_{N_2}} \tag{5.9}$$

$$q_{N_2} = \frac{q_{sN_2}b_{N_2}C_{N_2}}{1 + b_{N_2}C_{N_2} + d_{CO_2}C_{CO_2}} \tag{5.10}$$

A mixture of 15% CO_2 and 85% N_2 was considered at various pressures of the mixture, ranging from 0 to 1 bar. At these pressures and the initial composition, the IAST detailed in Appendix C and proposed extended model were used to determine the binary CO_2 and N_2 loadings. The results of this comparison are summarized in Figure 5.4.

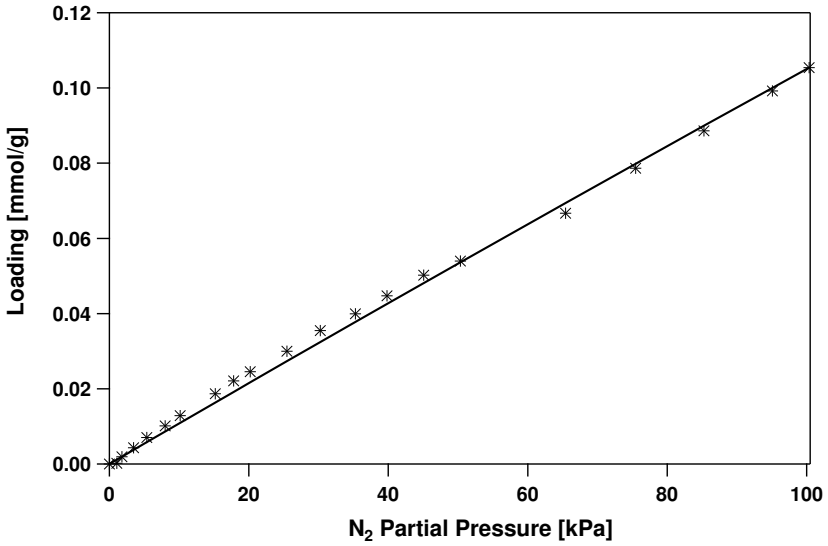

Figure 5.3: Adsorption Isotherm of Nitrogen on mmen-Fe_2 at 25°C. Markers represent experimental data points and lines represent the model fit.

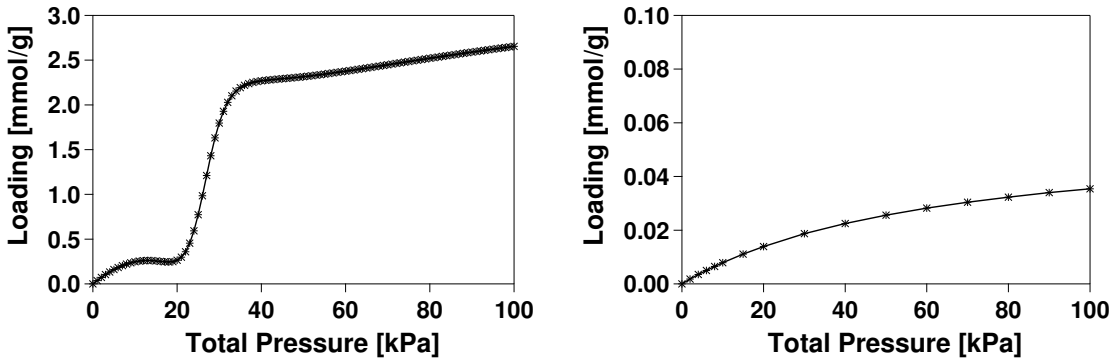

(a) (b)

Figure 5.4: Comparison of the binary loadings of (a)CO_2 and (b)N_2 calculated by the IAST and the extended quadratic-langmuir isotherm. Markers represent the IAST calculations, and lines represent the extended isotherm model calculations.

Table 5.4: Criteria used in selecting adsorption isotherm model for S-shaped isotherm. X indicates that the model does not satisfy the criterion and ✓indicates that the model satisfies the criterion.

Model	Multiple T Fit	Low P Fit	High P fit	Multi. Comp.
Quadratic	X	X	X	✓
Quadratic-Langmuir	X	✓	✓	✓
Rutherford CMMS	✓	✓	✓	X
Langmuir-Freundlich	X	X	X	✓
Modified Langmuir-Freundlich	X	✓	X	X

The selected quadratic-langmuir isotherm model can only be used to fit a single temperature using the same set of isotherm parameters. Therefore, in order to compare the performance of this metal-organic framework to the benchmark material, zeolite 13X, all further simulations performed will be done at isothermal conditions. An additional aspect of the mmen-Fe_2 MOF is that the step change pressure is dependent on the temperature. This changes from 0.035 bar at 25°C to 0.12 bar at 40°C based on the data in Figure 5.2.

5.2.3 Breakthrough Simulations

Several breakthrough simulations were performed using the isotherm parameters fitted for mmen-Fe_2 at 25°C. These simulations were performed for the purpose of understanding the difference between the adsorption and desorption of carbon dioxide on the S-shaped isotherm as opposed to the favourable type I isotherms which have been previously considered. For the adsorbent, all properties available were taken into consideration in the simulation, and the unknown propertes were taken to be similar to zeolite 13X. The column dimensions used are similar to those described for SIFSIX optimization and LPP cycle simulations. All properties other than the column dimensions are presented in Table 4.2. The particle density of the mmen-Fe_2 adsorbent was also assumed similar to that of zeolite 13X, at 1130 kg/m^3, as this data was unavailable in the literature.

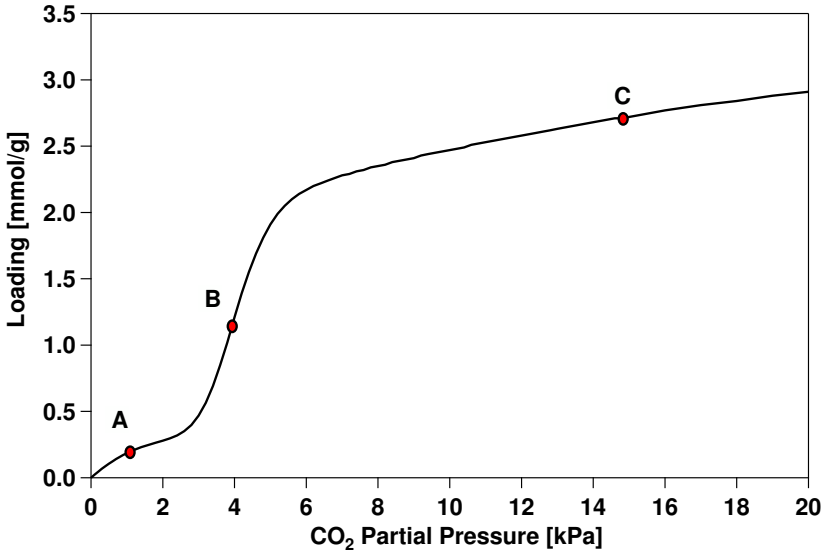

Figure 5.5: Quadratic-langmuir fitted isotherm for CO_2 on mmen-Fe_2 at 25°C, illustrating the points of interest being studied for breakthrough. A occurs before the step change in CO_2 loading, B during and C after the step change.

Breakthrough was performed by running the adsorption step of a simulation with a bed

initially saturated with nitrogen, with a feed of CO_2 and N_2 at 1 bar and 25°C, corresponding to different points on the isotherm. Figure 5.5 illustrates the points on the single component CO_2 isotherm on the mmen-Fe2 adsorbent corresponding to the composition of CO_2 in the breakthrough mixtures which will be considered. The three points, A, B and C, are specifically chosen to be before, during and after the step change in the CO_2 isotherm. The equivalent CO_2 mole fractions in the feed will be 0.01, 0.04 and 0.15, with the remainder being N_2 in each case. Desorption simulations were performed by running the adsorption step with a bed initially saturated with CO_2 at the three specified conditions for breakthrough, with a feed gas of pure N_2. As mentioned previously, these simulations are all isothermal, therefore heat transfer effects are absent.

The simulated breakthrough and desorption curves, done at point A, are presented in Figure 5.6. The breakthrough is a single shock wave, due to the species being able to move directly from the initial state at 0 to the feed concentration at 1 kPa on the isotherm by a single line connecting the two points. The desorption is a simple wave as the species must go through all the states prior to point A in order to get to the final state at 0. As a consequence, the desorption wave has a longer front than the breakthrough wave. These characteristics are typical for favorable isotherms, which is how the quadratic-langmuir model represents the low pressure region of the isotherm, before the step change.

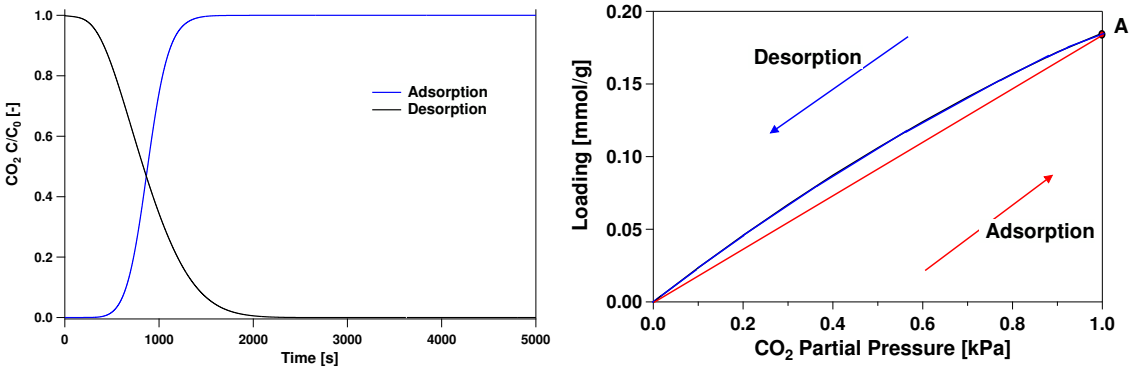

(a) (b)

Figure 5.6: (a)Breakthrough and desorption curves of a feed mixture of 1% CO_2 and 99% N_2 at 25°C and 1 bar (b)Single component CO_2 isotherm showing the transitions in adsorption and desorption.

The simulated breakthrough and desorption curves, done at point B, are presented in Figure 5.7. The breakthrough curve is a single shock wave, followed by a simple wave which gradually increases as the outlet concentration approaches the feed concentration of CO_2.

On the isotherm in Figure 5.7(b), a single line connects the initial state at 0 to a partial pressure of 2.4 kPa, which is representative of the shock wave seen on the breakthrough curve. Afterwards, the species must move through all the states from 2.4 kPa up until the feed concentration, which results in a very long simple wave. The desorption curve is a single shock front, followed by a very short, simple wave. Observation of the isotherm shows that the sharp increase in pressure at the point of the step change allows for a single line to connect the state at 4kPa to a point which is near the origin. This corresponds to the shock wave, after which a short simple wave is observed as the remaining CO_2 in the bed is eluted.

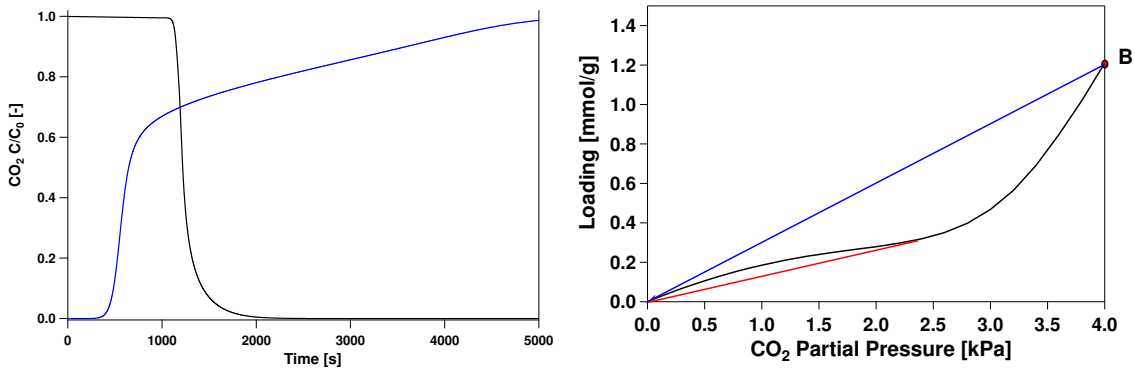

(a) (b)

Figure 5.7: (a)Breakthrough and desorption curves of a feed mixture of 4% CO_2 and 96% N_2 at 25°C and 1 bar (b)Single component CO_2 isotherm showing the transitions in adsorption and desorption.

The final breakthrough and desorption curves simulated at point C, are presented in Figure 5.8. This point was chosen as it is the feed composition of flue gas, and occurs well after the step change in CO_2. The breakthrough exhibits two distinct shock transitions, with a simple wave between them. On the isotherm, a single shockwave is represented by the transition from the initial state at the origin to 3 kPa on the isotherm. A short duration simple wave is observed as all the states from 3 kPa to 3.5kPa on the isotherm are passed through by CO_2. The second shock from 3.5 kPa up to the feed partial pressure at 15 kPa is then observed as a straight line can connect these two points, as in Figure 5.8(b). The desorption wave from point C to the origin, propagates as a shock wave followed by a long, simple wave, then another shock wave and a short simple wave. The first shock corresponds to the transition from 15 kPa to 8 kPa on the isotherm, the wave from 8 kPa to 6 kPa, and the second shock from 6 kPa to the origin. In the S shaped isotherm, the presence

of shock waves in the desorption simulation shows that there may be some advantage in lower evacuation times, as the pressure is reduced from P_{INT} to P_{L}. In comparison, the desorption in type I isotherms, such as CO_2 on Zeolite 13X is a simple wave.

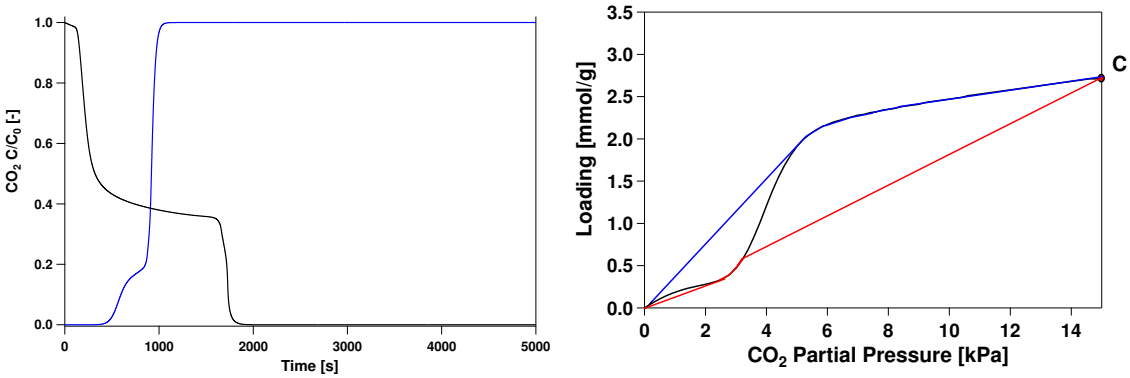

(a) (b)

Figure 5.8: (a)Breakthrough and desorption curves of a feed mixture of 15% CO_2 and 85% N_2 at 25°C and 1 bar (b)Single component CO_2 isotherm showing the transitions in adsorption and desorption.

5.3 4-Step LPP Cycle Simulations with Diamine-Appended MOFs

A comparison of the performance of the Zeolite 13X and mmen-Fe_2 isotherms was first done by considering a 4-step LPP cycle with a common set of operating parameters. These base operating parameters were t_{ads}= 94.89 s, t_{blow}= 122.84 s, t_{evac} = 189.46 s, P_{INT}= 0.18 bar, P_{L}= 0.02 bar and $v0$=0.58 m/s. Both simulations were run under isothermal conditions, for both 25°C and 40°C. The base simulation at 25°C resulted in 90.5% purity and 94.9% recovery for mmen-Fe_2 and 86% purity and 95% recovery for Zeolite 13X. The results of this simulation showed similar results for both adsorbents, therefore it was decided to perform parametric study, varying only one operating parameter, while keeping all of the other base parameters the same. In order to investigate the effect of the blowdown and evacuation pressures, P_{INT} and P_{L}, on the purity and recovery of both adsorbents, two parametric studies were done, using the operating parameters specified previously as base values. The P_{INT} and P_{L} values were then increased separately, keeping other base operating parameters constant.

The results of the parametric study of the effect of increasing P_{INT} for zeolite 13X and mmen-Fe_2 is presented in Figure 5.9. The intermediate pressure was increased from the

base value of 0.18 bar incrementally, up to 0.5 bar. For both adsorbents, the recovery is above 90% in all cases, and the recovery increases slightly as P_{INT} increases. The effect on purity, however, is that increasing P_{INT} decreases purity due to more N_2 remaining in the adsorption column. Additionally, at a both temperatures, the purity of the mmen-Fe_2 MOF is higher than that of 13X at the highest value of intermediate pressure of 0.5 bar. The recovery, however, at 40°C is much lower for mmen-Fe_2 than zeolite 13X, while at 25°C, both adsorbents had similar recovery.

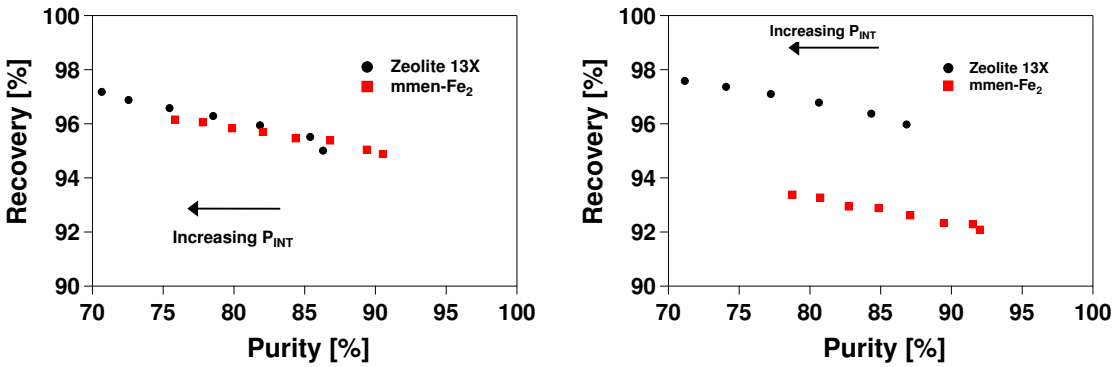

Figure 5.9: Purity and recovery of 4-step LPP cycle with zeolite 13X and mmen-Fe_2 at temperatures of (a)25°C and (b)40°C, with operating parameters t_{ads}= 94.89 s, t_{blow}= 122.84 s, t_{evac} = 189.46 s, P_{INT}= 0.18 bar, P_{L}= 0.02 bar and $v0$=0.58 m/s and increasing P_{INT} from 0.18 to 0.5 bar

A second parametric study was performed by using the base operating parameters and increasing the evacuation step pressure, P_{L}, from 0.02 to 0.05 bar for 25°C and 0.02 to 0.08 bar for 40°C, for both of the adsorbents. The results of this parametric study are presented in Figure 5.10. At a temperature of 25°C, the general trend for both adsorbents is that increasing the evacuation step pressure increases recovery and decreases purity. The absolute recovery for both adsorbents at 25°C are almost similar, however Zeolite 13X can achieve better purity at all the values of P_{L} simulated. At 40°C, a similar trend is observed for zeolite 13X, but the mmen-Fe_2 adsorbent shows a very different trend. In Figure 5.11, the variation of purity and recovery with increasing P_{L} is plotted for clarification. Increasing P_{L} results in a small increase in purity for 13X, while that for the mmen-Fe_2 MOF remains fairly constant. It can be also observed in Figure 5.11(b) that for both adsorbents, increasing the evacuation pressure decreases the recovery of CO_2 in the evacuation step. Additionally, a very sharp decrease in recovery is observed for mmen-Fe_2 at a P_{L} of 0.05 bar, after which the decrease of recovery with increasing P_{L} appears to reduce.

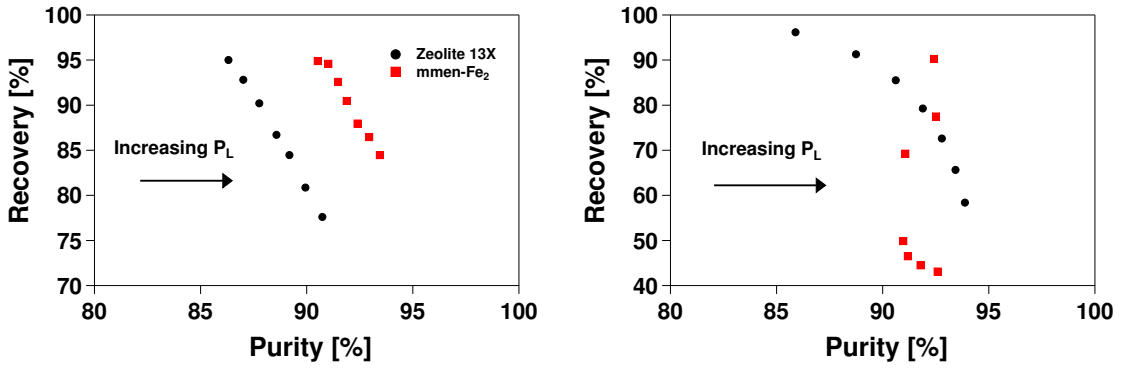

(a) (b)

Figure 5.10: Purity and recovery of 4-step LPP cycle with zeolite 13X and mmen-Fe_2 at temperatures of (a)25°C and (b)40°C with operating parameters t_{ads}= 94.89 s, t_{blow}= 122.84 s, t_{evac} = 189.46 s, P_{INT}= 0.18 bar, P_L= 0.02 bar and $v0$=0.58 m/s and increasing P_L

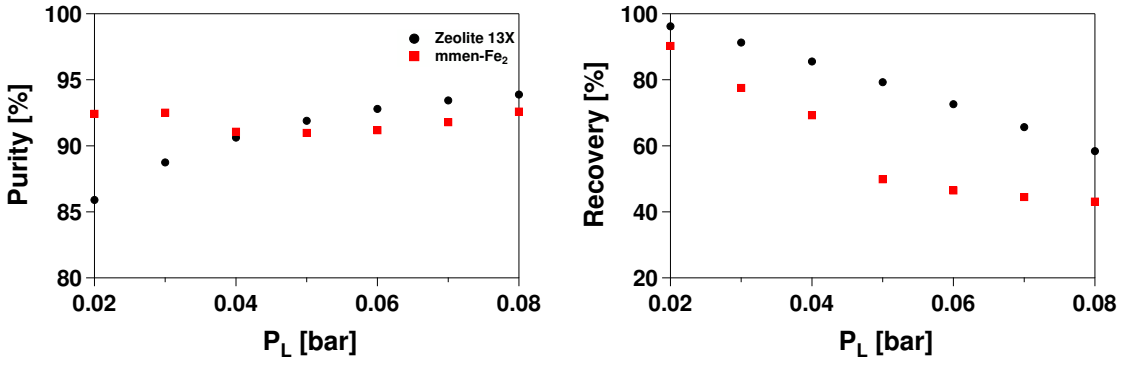

(a) (b)

Figure 5.11: (a)Purity and (b)Recovery of a 4-step LPP cycle with zeolite 13X and mmen-Fe_2 at 25°C and 40°C

The general trend of the parametric study performed using one base set of operating parameters, and changing the blowdown and evacuation step pressures, is that the mmen-Fe_2 adsorbent can potentially achieve better purities at a higher blowdown pressure. An increase in the evacuation pressures is not beneficial to the performance of the mmen-Fe_2 MOF, particularly at the higher temperature of 40°C. However, it must be noted that the operating parameters chosen were not optimized for either adsorbent in an isothermal case. The next step is therefore the comparison of the optimal performance of both adsorbents by multiobjective optimization.

5.4 Optimization - Maximization of Purity and Recovery

In order to compare the best performance of the metal-organic framework mmen-Fe_2 and Zeolite 13X, a set of purity-recovery optimization simulations were performed. The Rutherford CMMS model was used to generate a single component CO_2 isotherm at 30°C, since no experimental data was present in the literature at this value. This isotherm was then fitted to the Quadratic-Langmuir model. All simulations for optimization including are performed under isothermal conditions at the feed temperature, due to temperature dependence being unable to be described by the chosen isotherm model. The isothermal simulation also applies to 13X, for consistency in the comparison. The adsorption isotherm parameters used to model Zeolite 13X are fitted parameters taken from Haghpanah et al. [25]. The bounds on the decision variables of t_{ads},t_{blow},t_{evac}, P_{INT}, P_L and v_0 are provided in Table 4.3.
The results of the purity and recovery optimization are given in Figure 5.12. Both of the adsorbents are very similar in absolute performance, having a maximum purity of around 97% for 13X and 97.5% for mmen-Fe_2 at a constant recovery of 90%.

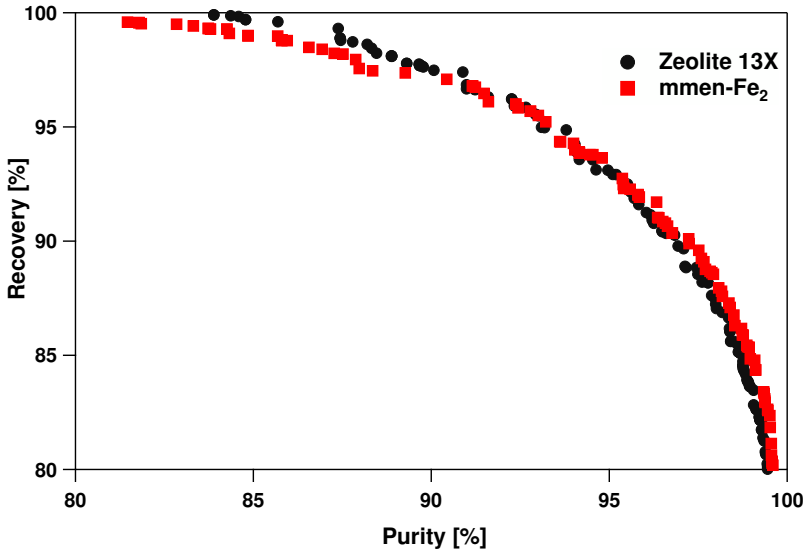

Figure 5.12: Purity-Recovery Paretos of mmen-Fe_2 and Zeolite 13X

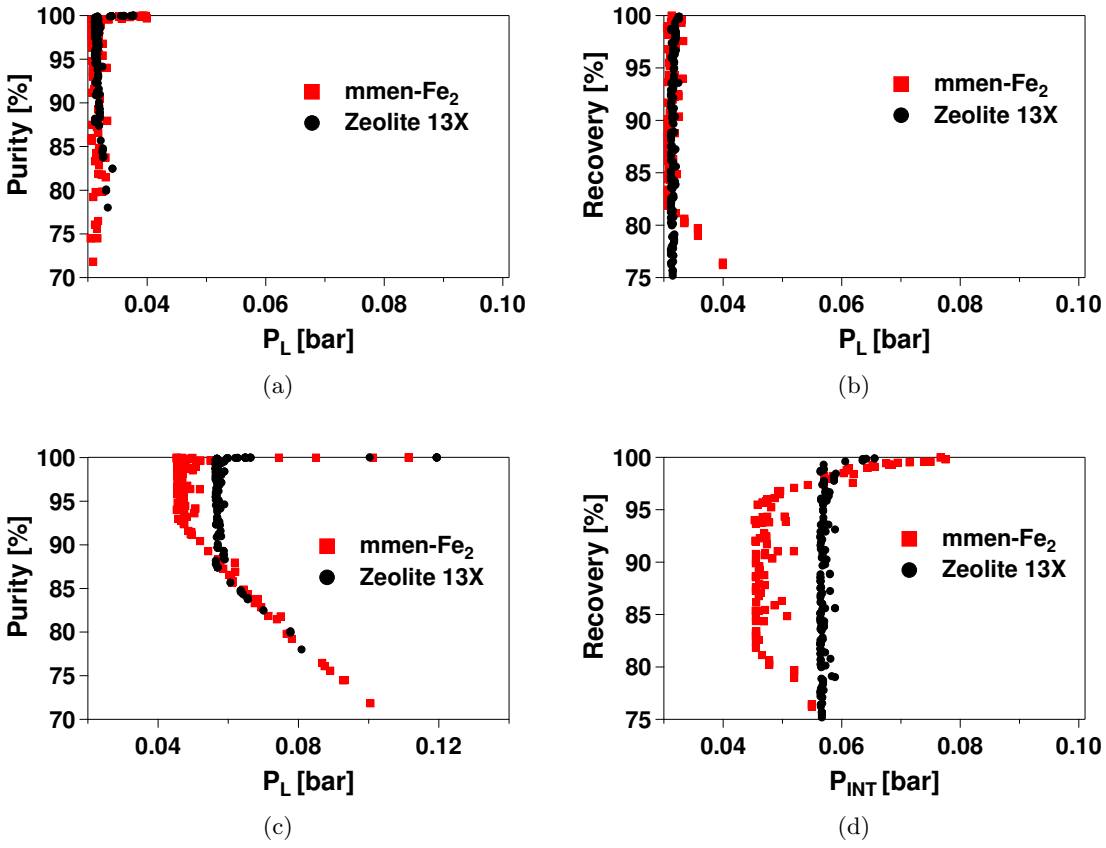

Figure 5.13: Pressures of the evacuation step corresponding to (a) Purity and (b) Recovery, and the blowdown step corresponding to (c) Purity and (d) Recovery for the pareto curve in Figure 5.12

The majority of the energy which is required by the four step VSA cycle with LPP comes from the vacuum pumps needed to maintain subatmospheric pressures in the blowdown and evacuation steps. The expected trend is that as P_{INT} increases, the purity decreases because more nitrogen is retained in the adsorption column hence reducing the purity in the evacuation step. The recovery, however, will increase in this scenario because less carbon dioxide is lost from the adsorption column in the blowdown step. In Figure 5.13, the blowdown and evacuation pressures corresponding to the simulated results displayed in the Figure 5.12 are shown. The main observation for the evacuation pressure, P_L, is that for both of the adsorbents is required to be in the range of 0.03 to 0.04 bar for maintaining both high purity and recovery. This is at the lower bound for this particular decision variable. The value of blowdown pressure shows more variance in both adsorbents, with high purities being achievable at values of P_{INT} greater than 0.1 bar. The MOF also seems to be able to achieve higher recoveries than 13X with P_{INT} greater than 0.065 bar, which may indicate lower energy potential. Therefore, an energy productivity constrained optimization is useful at this point in order to determine the minimum energy required for 90% purity and recovery and the maximum productivity for the SIFSIX adsorbents.

5.5 Optimization - Energy and Productivity

Energy and productivity optimization was performed for both mmen-Fe_2 and zeolite 13X adsorbents, both at an isothermal condition of 30°C. The constraint on the optimization is 90% purity and recovery, and the objective functions as well as the bounds of the decision variables are kept the same as for the SIFSIX optimization. The energy productivity pareto for both of the adsorbents is presented in Figure 5.14. Based on these results mmen-Fe_2 has both a lower energy consumption and higher productivity than zeolite 13X. The minimum energy for zeolite 13X was at 134 kWh/t CO_2 at 0.57 mol CO_2/m^3ads/s. The corresponding minimum energy for mmen-Fe_2 was 110.7 kWh/t CO_2 at a productivity of 1 mol CO_2/m^3ads/s.

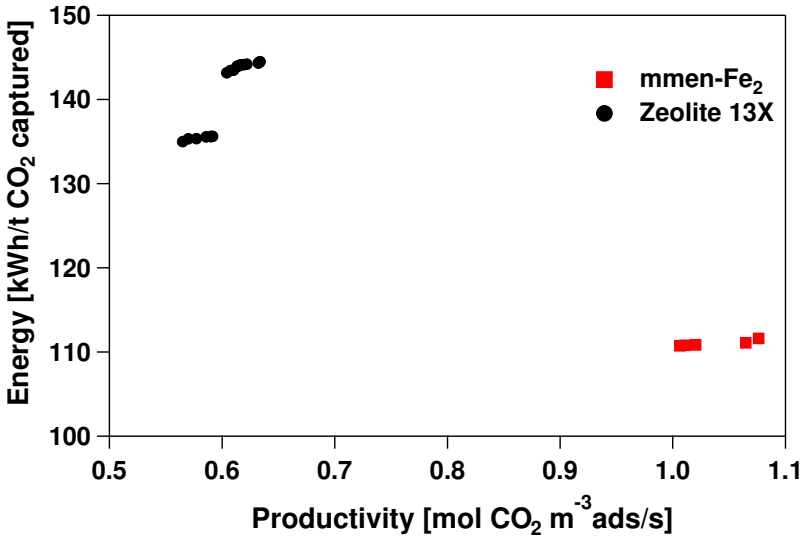

Figure 5.14: Energy-Productivity Paretos of mmen-Fe_2 and Zeolite 13X

The majority of the energy requirements for the 4 step VSA cycle with LPP come from the vacuum pumps for the blowdown and the evacuation steps. Figure 5.15 shows the blowdown and evacuation pressures for the energy and productivity paretos for zeolite 13X and mmen-Fe_2. The evacuation pressure similar to the purity and recovery optimization remained close to the lower bound for both adsorbents. The trend with the blowdown pressure, P_{INT}, is that as it increases, the energy requirement decreases as expected. In this case the optimized VSA cycle with mmen-Fe_2 can achieve 90% purity and recovery with a maximum P_{INT} of 0.2 bar, compared to 13X at 0.16 bar. A major reason why the mmen-Fe_2 adsorbent can achieve better performance than 13X with higher pressures of the blowdown step is due to the N_2 isotherms of both adsorbents. In Figure 5.16, the single component nitrogen isotherms for mmen-Fe_2 and zeolite 13X at 30°C, as calculated by the Langmuir isotherm model, are presented. The capacity for nitrogen in the MOF is much lower than that for 13X, so the removal of nitrogen in the blowdown step can potentially be done at a higher pressure for the MOF, which is observed in the optimization.

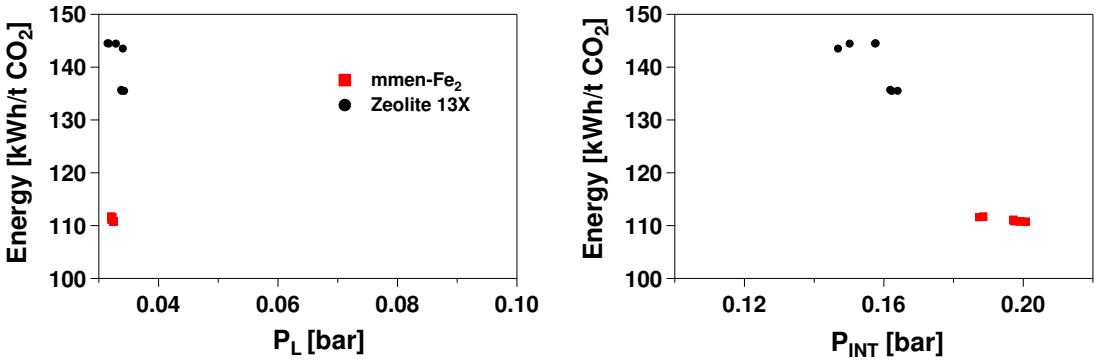

Figure 5.15: Pressures of the a.)evacuation and b.)blowdown steps corresponding to the pareto curves in Figure 5.14, for both Zeolite 13X and mmen-Fe_2 isotherms.

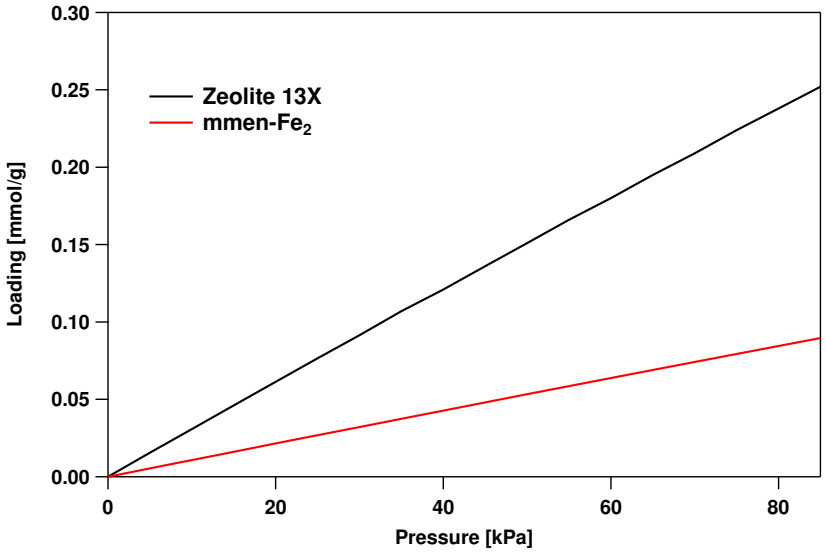

Figure 5.16: Nitrogen isotherms of Zeolite 13X and mmen-Fe_2 at 30°C

The operating parameters for the mmen-Fe_2 adsorbent which resulted in the minimum energy of 110 kWh/t are t_{ads}= 60.51 s,t_{blow}= 54.67 s,t_{evac}= 39.16 s,P_{INT}= 0.188 bar,P_L= 0.032 bar and $v0$ = 0.91 ms^{-1}. For Zeolite 13X, the corresponding operating parameters resulting in the minimum energy of 135 kWh/t are t_{ads}= 91.16 s,t_{blow}= 100.87 s,t_{evac}= 77.91 s,P_{INT}= 0.16 bar,P_L= 0.034 bar and $v0$ = 0.53 ms^{-1}. The column CO_2 axial profiles for both of these optimized conditions, both in the gas and solid phase, are presented in Figure 5.17. The gas and solid phase profiles plotted are taken at the end of each step of the 4 step LPP cycle, after CSS has been attained. In the solid phase, the CO_2 occupies a small zone equivalent to a tenth of the length of the column. In Figure 5.18, the binary carbon dioxide

loading is plotted for each step of the cycle at the CSS condition. Between the adsorption and blowdown steps, the CO_2 loading has not significantly reduced, indicating that a small amount of CO_2 is desorbed from the transition from P_H to P_{INT}. Going from the blowdown to the evacuation steps, however, the CO_2 loading reduces from approximately 2.4 mmol/g to 0.1 mmol/g. This is also accompanied by an increase in the mole fraction of CO_2 in the column. The CO_2 axial profile in the solid phase for zeolite 13X shows a comparatively smaller working capacity of approximately 0.9 mol/g, by the difference between the loadings at the blowdown and evacuation steps.

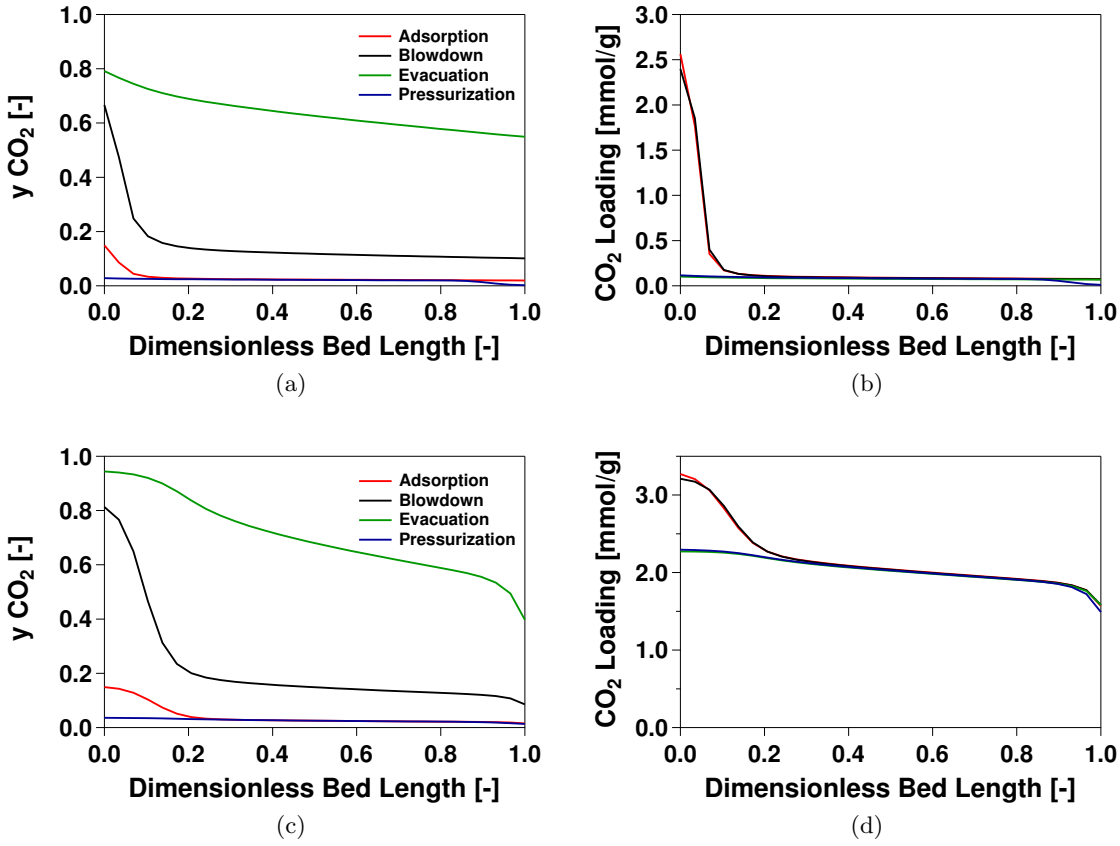

Figure 5.17: Axial CO_2 profiles for simulations corresponding to minimum energy for mmen-Fe_2 in a.)gas phase and b.)solid phase and zeolite 13X in c.) the gas phase and d.)the solid phase

The assumption of an isothermal condition with a feed temperature of 30°C is an issue which must be addressed. For Zeolite 13X, the operating conditions resulting in minimum energy were simulated for a non-isothermal case. The values of the performance indicators in the isothermal and nonisothermal cases are shown in Table 5.5. The purity increases by 1.5%, and recovery decreases by 3% for the nonisothermal case. Both the energy and

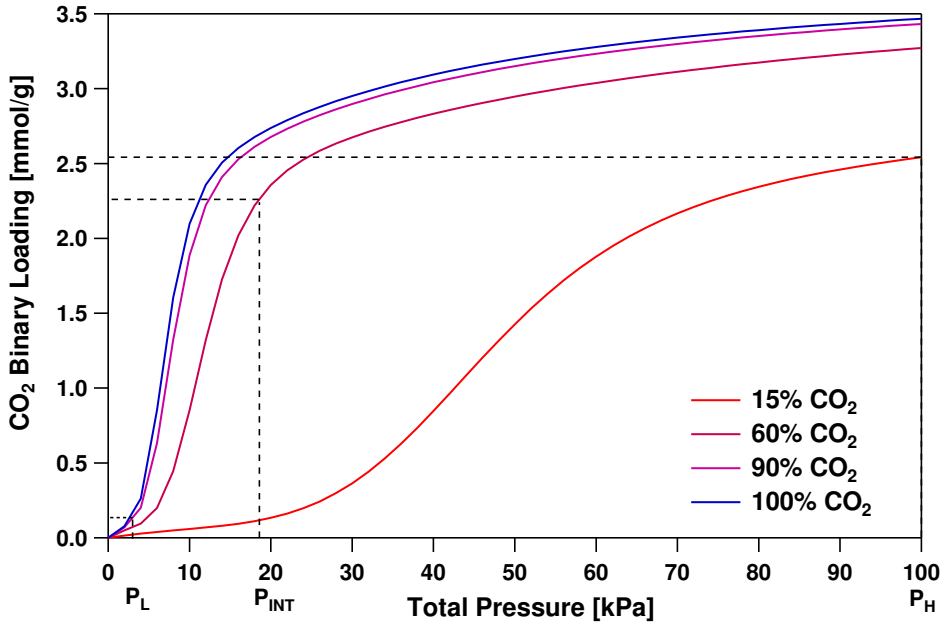

Figure 5.18: CO_2 binary isotherms for 4 step LPP cycle corresponding to minimum energy

productivity decrease for the non-isothermal case, but in both cases the difference between the isothermal and non-isothermal cases is less than 10%. The assumption results in an optimized condition where the recovery does not meet the performance requirement of 90%.

Table 5.5: Performance indicators for the isothermal and non-isothermal simulations using zeolite 13X

Simulation Condition	Purity[%]	Recovery[%]	Energy [kWh/t]	Prod.[mol/m^{3}s]
Isothermal	90.19	90.05	135.5	0.57
Non-Isothermal	91.56	87.02	128.2	0.54

Another assumption made in the simulations due to the absence of data from the literature is that the density of the mmen-Fe_2 adsorbent is equivalent to that of zeolite 13X. The simulations consider an adsorption column packed with equal volumes of adsorbent, and the loading of the different components are calculated in terms of volume of adsorbent. Therefore, the productivity will be directly proportional to the density of the adsorbent. If the density of the mmen-Fe_2 material is actually less than that of zeolite 13X, then the productivity is expected to reduce accordingly, and vice-versa.

An isothermal case study at $30°C$ shows that the diamine appended MOF, mmen-Fe_2 can meet the required performance of 90% purity and recovery of the CO_2 extract. Furhermore, an energy and productivity analysis shows that its performance is better than zeolite 13X for post-combustion CO_2 capture using a feed of 15% CO_2 and 85% N_2. Assuming simi-

lar particle density, step change in the carbon dioxide isotherm results in higher working capacity than the favorable isotherm observed with CO_2 on zeolite 13X and by extension, higher productivity is observed. The minimum energy observed for the mmen-Fe_2 adsorbent was 110 kWh/t, which was better than zeolite 13X at 135 kWh/t. The reason for this was a higher blowdown pressure for mmen-Fe_2 at 0.188 bar, compared to zeolite 13X at 0.16 bar. Therefore, the diamine-appended MOFs displaying an S-shaped CO_2 isotherm are very promising for CO_2 capture by adsorption.

Chapter 6

Conclusion and Recommendations

6.1 Conclusions

The primary aim of this thesis is the evaluation of several novel metal-organic framework (MOF) materials for CO_2 capture from post-combustion flue gas. This was performed by extraction of the experimental adsorption equilibrium data from literature, fitting this data to an isotherm model and implementing the isotherm data as well as any additional adsorbent parameters. The first type of MOFs evaluated were the SIFSIX MOFs published by Nugent et al. [6]. These MOFs are particularly interesting because they are reported to be relatively unaffected by the presence of water, which has been shown to increase the energy requirements of a PSA cycle in which the adsorbent is Zeolite 13X.

The experimental isotherm data from the publication of Nugent et al. was fitted for the SIFSIX metal-organic framework materials with a single site Langmuir model. Multicomponent adsorption data for water vapor, CO_2 and N_2 was unavailable in the literature and the IAST does not predict water loading correctly based on breakthrough results presented by Nugent et al., therefore only dry conditions will be considered in this simulation. Using the fitted adsorption equilibrium data and additional adsorbent parameters provided, a multi-objective optimization was then performed in order to evaluate the performance of the SIFSIX MOFs compared to the benchmark Zeolite 13X. The results showed that the SIFSIX MOFs have similar performance to 13X in terms of purity and recovery. An energy and productivity optimization was also performed, revealing that with dry flue gas, SIFSIX-2-Cu-i has similar energy requirements as zeolite 13X at 155 kWh/t CO_2 captured, and SIFSIX-3-Zn has slightly lower energy requirement at 140 kWh/t CO_2 captured. It was also observed that the productivity of SIFSIX-3-Zn, at 0.18 mol CO_2/m^3 adsorbent/s, was significantly lower than that of Zeolite 13X (0.5 mol CO_2/m^3 adsorbent/s and SIFSIX-2-Cu-i (0.7 mol CO_2/m^3 adsorbent/s) due to its lower working capacity, and higher optimized

cycle time. Therefore, SIFSIX-3-Zn cannot be considered as an alternative to 13X due to its significantly lower productivity and SIFSIX-2-Cu-i has marginally better performance over Zeolite 13X in terms of productivity which would not justify the additional cost of manufacturing a new adsorbent material.

The second type of metal-organic framework material evaluated is the diamine-appended MOF, which was published by McDonald et al. [6], [22]. These novel MOFs display a step change in the CO_2 isotherm, meaning that the loading is very low at low partial pressures and increases significantly at a certain step pressure. Assuming that the step change occurs in the post-combustion range for CO_2 concentration, these adsorbents will have a large working capacity. Of the different metal-organic frameworks presented, it was determined that mmen-Fe_2 was the only ones which have a step change for 25°C and 40°C within the post-combustion CO_2 partial pressure range of 0.03 to 0.15 bar. Therefore, the mmen-Fe_2 was the adsorbent chosen for further study and analysis.

Isotherms with a step change, or an S shape have an inflection point, and are classified as type V isotherms. Therefore, a Langmuir model, which was used to calculate SIFSIX and 13X loadings, is unable to model the CO_2 adsorption on mmen-Fe_2. A quadratic-langmuir isotherm model was shown to satisfactorily fit the experimental adsorption isotherm data of CO_2 on mmen-Fe_2 at a single temperature, while being easily extended to account for multiple component adsorption.

A comparison of the performance of the benchmark zeolite 13X and the diamine-appended MOF, mmen-Fe_2, was then done using multiobjective optimization as a basis. In order to draw a fair comparison between the two adsorbents, both were kept isothermal at 30°C. It was found that in terms of purity and recovery, both zeolite 13X and mmen-Fe_2 had similar performance. An energy and productivity analysis, however, reveals that mmen-Fe_2 can achieve 90% purity and recovery at a minimum energy of 110 kWh/t CO_2 captured, compared to Zeolite 13X at 135 kWh/t CO_2 captured. This is because the blowdown pressure of mmen-Fe_2 can be increased to 0.2 bar, compared to 13X at 0.16 bar, due to the lower capacity for N_2 in mmen-Fe_2. Additionally, the productivity of mmen-Fe_2 corresponding to minimal energy was 1.02 mol CO_2/m^3 adsorbent/s, compared to Zeolite 13X at 0.59 molCO_2/m^3 adsorbent/s. This means that the diamine-appended MOFs can achieve satisfactory post-combustion CO_2 capture with noticeably less energy penalty than Zeolite 13X, and is a good alternative adsorbent to Zeolite 13X for CO_2 capture.

6.2 Recommendations and Future Work

In this study, SIFSIX materials were evaluated under an ideal scenario, i.e. dry post-combustion flue gas. Realistically, post-combustion flue gas contains water as an additional component, as well as several trace impurities, among them, SO_x and NO_x gases. The effect of water on the adsorption of CO_2 and N_2 has been studied in literature, as well as its effect on VSA processes. However, experimental mulicomponent isotherms of CO_2, N_2 and water vapor on the SIFSIX and other MOF adsorbents is currently unavailable. Future work can include the experimental measurement of this multicomponent data, as well as further modeling and optimization to determine how water affects the SIFSIX adsorbents. As for trace impurities, the stability of MOFs and other adsorbents over many adsorption and desorption cycles with SO_x and NO_x gases is another area for potential research work. Effects of the trace impurities on adsorption of CO_2 is expected to be minor, due to the low concentration in post-combustion flue gas.

Modeling and optimization of the mmen-Fe_2 diamine-appended metal-organic framework material was done isothermally in this study, due to limitations of the selected isotherm model. Further study can be conducted by using a model which can fit multiple temperature mmen-Fe_2 CO_2 adsorption data, while also being easily extended to take into account the competitive adsorption of N_2 and any other components of interest. Performing non-isothermal optimization of the mmen-Fe_2 in comparison to 13X will give a more realistic comparison of the two adsorbents, particularly because the pressure at which the isotherm displays a step change is dependent on the temperature.

The performance indicators,energy and productivity, are used to estimate roughly the operating cost and capital cost of a PSA process. For the metal-organic frameworks, crystal density is reported in the literature. Packing of adsorbents into a column usually involves the addition of a binder to form a pellet from the crystalline adsorbent powder. Experimental determination of the actual pellet size and density of the adsorbent is another area for research work. This data can then be incorporated into a full PSA model in order to evaluate adsorbent performance more accurately.

Bibliography

[1] C. D. Keeling, S. C. Piper, R. B. Bacastow, M. Wahlen, T. P. Whorf, M. Heimann, and H. A. Meijer, "Exchanges of atmospheric CO_2 and $^{13}CO_2$ with the terrestrial biosphere and oceans from 1978 to 2000.," tech. rep., Scripps Institution of Oceanography, San Diego, 2001.

[2] B. Metz, O. Davidson, H. de Coninck, M. Loos, and L. Meyer, *Carbon Dioxide Capture and Storage*. Cambridge University Press, 2005.

[3] S. Cavenati, C. A. Grade, and A. E. Rodrigues, "Adsorption equilibrium of methane, carbon dioxide, and nitrogen on zeolite 13x at high pressures," *Journal of Chemical and Engineering Data*, 2004.

[4] D. Xu, P. Xiao, J. Zhang, G. Li, G. Xiao, P. A. Webley, and Y. Zhai, "Effects of water vapour on CO_2 capture with vacuum swing adsorption using activated carbon," *Chemical Engineering Journal*, vol. 230, pp. 64 – 72, 2013.

[5] P. Nugent, Y. Belmabkhout, S. D. Burd, A. J. Cairns, R. Luebke, K. Forrest, T. Pham, S. Ma, B. Space, L. Wojtas, M. Eddaoudi, and M. J. Zaworotko, "Porous materials with optimal adsorption thermodynamics and kinetics for CO_2 separation.," *Nature*, vol. 495, pp. 80 – 84, 2013.

[6] T. M. McDonald, F. A. Mason, X. Kong, E. D. Bloch, D. Gygi, A. Dani, V. Crocella, F. Giordanino, S. O. Odoh, W. S. Drisdell, B. Vlaisavljevich, A. L. Dzubak, R. Poloni, S. K. Schnell, N. Planas, K. Lee, T. Pascal, L. F. Wan, D. Prendergast, J. B. Neaton, B. Smit, J. B. Kortright, L. Gagliardi, S. Bordiga, J. A. Reimer, and J. R. Long, "Co-operative insertion of CO_2 in diamine-appended metal-organic frameworks," *Nature*, vol. 14327, 2015.

[7] D. Ko, R. Siriwardane, and L. T. Biegler, "Optimization of pressure swing adsorption and fractionated vacuum pressure swing adsorption processes for CO_2 capture," *Industrial & Engineering Chemistry Research*, no. 44, pp. 8084–8094, 2005.

[8] L. Wang, Z. Liu, P. Li, J. Wang, and J. Yu, "CO_2 capture from flue gas by two successive vpsa units using 13xapg," *Adsorption*, vol. 18, pp. 445–459, 2012.

[9] G. Li, P. Xiao, J. Zhang, and P. A. Webley, "The role of water on postcombustion CO_2 capture by vacuum swing adsorption: Bed layering and purge to feed ratio," *AIChE Journal*, vol. 60, pp. 673–689, Feb 2014.

[10] S. Krishnamurthy, R. Haghpanah, A. Rajendran, and S. Farooq, "Simulation and optimization of a dual-adsorbent, two-bed vacuum swing adsorption process for CO_2 capture from wet flue gas.," *Industrial and Engineering Chemistry Research*, vol. 53, pp. 14462 – 14473, 2014.

[11] A. S. Bhown and B. C. Freeman, "Analysis and status of post-combustion carbon dioxide capture technologies," *Environ. Sci. Technol.*, vol. 45, pp. 8624–8632, September 2011.

[12] J. Davison and K. Thambimuthu, "An overview of technologies and costs of carbon dioxide capture in power generation," *Institute of Mechanical Engineering*, vol. 223, 2009.

[13] N. E. T. L. NETL, "Carbon capture technology program plan," January 2013.

[14] J. Abanades, B. Arias, T. M. A. Lyngfelt, D. Wiley, H. Li, M. Ho, E. Mangano, and S. Brandani, "Emerging CO_2 capture systems," *International Journal of Greenhouse Gas Control*, April 2015.

[15] A. D. Ebner and J. A. Ritter, "State-of-the-art adsorption and membrane separation processes for carbon dioxide production from carbon dioxide emitting industries," *Separation Science and Technology*, vol. 44, no. 6, pp. 1273 – 1421, 2009.

[16] R. T. Yang, *Adsorbents: Fundamentals and Applications*. Wiley, 2003.

[17] D. W. Breck, *Zeolite Molecular Sieves: structure, chemistry, and use*. Wiley, 1974.

[18] D. M. Ruthven, *Principles of Adsorption and Adsorption Processes*. John Wiley & Sons, 1984.

[19] J. R. L. Li, R. J. Kuppler, and H. C. Zhou, "Selective gas adsorption and separation in metal-organic frameworks," *Chemical Society Reviews*, vol. 38, pp. 1477–1504, 2009.

[20] Y. Wang and M. D. LeVan, "Adsorption equilibrium of binary mixtures of carbon dioxide and water vapor on zeolites 5a and 13x," *J. Chem. Eng. Data*, vol. 55, pp. 3189–3195, June 2010.

[21] S. Choi, J. H. Drese, and C. W. Jones, "Adsorbent material for carbon dioxide capture from large anthropogenic point sources," *ChemSusChem*, vol. 2, pp. 796 – 854, 2009.

[22] T. M. McDonald, W. R. Lee, J. A. Mason, B. M. Wiers, C. S. Hong, and J. R. Long, "Capture of carbon dioxide from air and flue gas in the alkylamine-appended metalorganic framework mmen-mg2(dobpdc)," *Journal of the American Chemical Society*, vol. 134, pp. 7056–7065, April 2012.

[23] C. A. Grande, "Advances in pressure swing adsorption for gas separation," *International Scholarly Research Network Chemical Engineering*, vol. 2012, no. 982934, 2012.

[24] R. Haghpanah, R. Nilam, A. Rajendran, S. Farooq, and I. A. Karimi, "Cycle synthesis and optimization of a vsa process for postcombustion CO_2 capture," *AIChE Journal*, vol. 59, pp. 4735–4748, August 2013.

[25] R. Haghpanah, A. Majumder, R. Nilam, A. Rajendran, S. Farooq, I. A. Karimi, and M. Amanullah, "Multiobjective optimization of a four-step adsorption process for post-combustion CO_2 capture via finite volume simulation," *Industrial & Engineering Chemistry Research*, vol. 52, pp. 4249–4265, 2013.

[26] E. Kikkinides, R. Yang, and S. Cho, "Concentration and recovery of CO_2 from flue gas by pressure swing adsorption," *Industrial & Engineering Chemistry Research*, no. 32, pp. 2714–2720, 1993.

[27] C. Shen, Z. Liu, P. Li, and J. Yu, "Two-stage vpsa process for CO_2 capture from flue gas using activated carbon beads," *Industrial & Engineering Chemistry Research*, vol. 51, pp. 5011–5021, 2012.

[28] L. Wang, Y. Yang, W. Shen, X. Kong, P. Li, J. Yu, and A. E. Rodrigues, "CO_2 capture from flue gas in an existing coal-fired power plant by two successive pilot-scale vpsa units," *Industrial & Engineering Chemistry Research*, vol. 52, pp. 7947–7955, 2013.

[29] J. Zhang, P. A. Webley, and P. Xiao, "Effect of process parameters on power requirements of vacuum swing adsorption technology for CO_2 capture from flue gas," *Energy Conversion and Management*, vol. 49, no. 2, pp. 346–356, 2008.

[30] G. Li, P. Xiao, P. A. Webley, J. Zhang, and R. Singh, "Competition of CO_2/H_2O in adsorption based CO_2 capture," *Energy Procedia*, vol. 1, pp. 1123–1130, 2009.

[31] Y. Wang and M. D. LeVan, "Adsorption equilibrium of carbon dioxide and water vapor on zeolites 5a and 13x and silica gel: Pure components," *J. Chem. Eng. Data*, vol. 54, pp. 2839–2844, June 2009.

[32] T. Pham, K. A. Forrest, K. McLaughlin, B. Tudor, P. Nugent, A. Hogan, A. Mullen, C. R. Cioce, M. J. Zaworotko, and B. Space, "Theoretical investigations of CO_2 and H_2 sorption in an interpenetrated square-pillared metalorganic material," *J. Phys. Chem.*, vol. 117, pp. 9970 – 9982, 2013.

[33] N. C. Burch, H. Jasuja, and K. S. Walton, "Water stability and adsorption in metal-organic frameworks," *Chemical Reviews*, no. 114, pp. 10575–10612, 2014.

[34] G. Guiochon, A. Felinger, D. G. Shirazi, and A. M. Katti, *Fundamentals of Preparative and Nonlinear Chromatography (2nd edition)*. Elsevier, Inc., 2006.

[35] S. W. Rutherford, "Modeling water adsorption in carbon micropores: Study of water in carbon molecular sieves," *Langmuir*, no. 22, pp. 702–708, 2006.

[36] M. Ilic, D. Flockerzi, and A. Seidel-Morgenstern, "A thermodynamically consistent explicit competitive adsorption isotherm model based on second-order single component behaviour," *Journal of Chromatography A*, vol. 1217, pp. 2132–2137, 2010.

[37] E. Magano, D. Friedrich, and S. Brandani, "Robust algorithms for the solution of the ideal adsorbed solution theory," *AIChE Journal*, 2014.

[38] H. O. R. Landa, D. Flockerzi, and A. Seidel-Morgenstern, "A method for efficiently solving the iast equations with an application to adsorber dynamics," *AIChE Journal*, vol. 59, no. 4, pp. 1263–1273, 2013.

Appendix A

Nomenclature

A	Cross sectional area of column [m]
c	Gas phase concentration [m^3mol^{-1}]
C_{pa}	Adsorbed phase specific heat capacity [$Jkg^{-1}K^{-1}$]
C_{pg}	Gas phase specific heat capacity [$Jkg^{-1}K^{-1}$]
C_{ps}	Adsorbent specific heat capacity [$Jkg^{-1}K^{-1}$]
C_{pw}	Column wall specific heat capacity [$Jkg^{-1}K^{-1}$]
D_M	Molecular diffusivity at 1 atm and 298 K [m^2s^{-1}]
D_L	Axial dispersion coefficient [m^2s^{-1}]
f	State variable
f_j	Cell average of the state variable
h_i	Inside heat transfer coefficient [$Wm^{-2}K^{-1}$]
h_o	Outside heat transfer coefficient [$Wm^{-2}K^{-1}$]
H	Enthalpy [$Jmol^{-1}$]
k	mass transfer coefficient [s^{-1}]
K_w	Wall thermal conductivity [$Wm^{-1}K^{-1}$]
K_Z	Effective gas thermal conductivity [$Wm^{-1}K^{-1}$]
L	Column length [m]
P	Pressure [Pa]
$\bar{P}$	Dimensionless pressure
Pe	Peclet Number
Pe_h	Heat transfer peclet number
q	Solid phase concentration [$molm^{-3}$]
q_s	Reference saturation loading [$molm^{-3}$]
r_i	Column inner radius [m]
r_o	Column outer radius [m]
r_p	Particle radius [m]
R	Universal gas constant [$Jmol^{-1}K^{-1}$]
t	Time [s]
T	Temperature [K]
$\bar{T}$	Dimensionless temperature
$\bar{T_a}$	Dimensionless ambient temperature
$\bar{T_w}$	Dimensionless wall temperature
v_o	Interstitial velocity [ms^{-1}]
$\bar{v}$	Dimensionless velcoity

x	Dimensionless solid phase composition
x^*	Dimensionless equilibrium solid phase composition
y	Gas phase mole fraction
Z	Dimensionless axial position
α	Dimensionless mass transfer coefficient
ε_b	Bed voidage
ε_p	Particle voidage
μ	Fluid viscosity [$\mathrm{kgm^{-1}s^{-1}}$]
ρ_b	Bulk density of fluid [$\mathrm{gcm^{-3}}$]
ρ_g	Density of fluid [$\mathrm{kgm^{-3}}$]
ρ_s	Density of adsorbent [$\mathrm{kgm^{-3}}$]
ρ_w	Density of column wall [$\mathrm{kgm^{-3}}$]
Π	Dimensionless group in wall energy balance
τ	Dimensionless time
τ'	Tortuosity
Ω	Dimensionless group in column energy balance
Ψ	Dimensionless group in mass balance

Appendix B

Boundary Conditions for Basic 4-Step VSA Cycle

Pressurization

$$\left.\frac{\partial y_i}{\partial Z}\right|_{Z=0} = -\bar{v}\Big|_{Z=0} Pe(y_{i,feed} - y_i\Big|_{Z=0})$$

$$\left.\frac{\partial y_i}{\partial Z}\right|_{Z=1} = 0$$

$$\left.\frac{\partial \bar{T}}{\partial Z}\right|_{Z=0} = -\bar{v}\Big|_{Z=0} Pe_h(\bar{T_{feed}} - \bar{T}\Big|_{Z=0})$$

$$\left.\frac{\partial \bar{T}}{\partial Z}\right|_{Z=1} = 0$$

$$\bar{T_w}\Big|_{Z=0} = \bar{T_w}\Big|_{Z=1} = \bar{T_a}$$

$$\bar{P}\Big|_{Z=0} = \frac{P_H}{P_0} + \left(\frac{P_H}{P_0} - \frac{P_L}{P_0}\right) e^{-a_1 \tau \frac{L}{v_0}}$$

$$\bar{v}\Big|_{Z=1} = 0$$

Adsorption

$$\left.\frac{\partial y_i}{\partial Z}\right|_{Z=0} = -\bar{v}\Big|_{Z=0} Pe(y_{i,feed} - y_i\Big|_{Z=0})$$

$$\left.\frac{\partial y_i}{\partial Z}\right|_{Z=1} = 0$$

$$\left.\frac{\partial \bar{T}}{\partial Z}\right|_{Z=0} = -\bar{v}\Big|_{Z=0} Pe_h(\bar{T_{feed}} - \bar{T}\Big|_{Z=0})$$

$$\left.\frac{\partial \bar{T}}{\partial Z}\right|_{Z=1} = 0$$

$$\bar{T_w}\Big|_{Z=0} = \bar{T_w}\Big|_{Z=1} = \bar{T_a}$$

$$\bar{P}\Big|_{Z=1} = 1$$

$$\bar{v}\Big|_{Z=0} = 1$$

Blowdown

$$\left.\frac{\partial y_i}{\partial Z}\right|_{Z=0} = 0$$

$$\left.\frac{\partial y_i}{\partial Z}\right|_{Z=1} = 0$$

$$\left.\frac{\partial \bar{T}}{\partial Z}\right|_{Z=0} = 0$$

$$\left.\frac{\partial \bar{T}}{\partial Z}\right|_{Z=1} = 0$$

$$\bar{T_w}\Big|_{Z=0} = \bar{T_w}\Big|_{Z=1} = \bar{T_a}$$

$$\bar{v}\Big|_{Z=0} = 0$$

$$\bar{P}\Big|_{Z=1} = \frac{P_I}{P_0} + \left(\frac{P_H}{P_0} - \frac{P_I}{P_0}\right) e^{-a_1 \tau \frac{L}{v_0}}$$

Evacuation

$$\left.\frac{\partial y_i}{\partial Z}\right|_{Z=1} = 0$$

$$\left.\frac{\partial y_i}{\partial Z}\right|_{Z=0} = 0$$

$$\left.\frac{\partial \bar{T}}{\partial Z}\right|_{Z=1} = 0$$

$$\left.\frac{\partial \bar{T}}{\partial Z}\right|_{Z=0} = 0$$

$$\left.\bar{T_w}\right|_{Z=0} = \left.\bar{T_w}\right|_{Z=1} = \bar{T_a}$$

$$\left.\bar{v}\right|_{Z=1} = 0$$

$$\left.\bar{P}\right|_{Z=1} = \frac{P_L}{P_0} + \left(\frac{P_I}{P_0} - \frac{P_L}{P_0}\right) e^{-a_1 \tau \frac{L}{v_0}}$$

Appendix C

Ideal Adsorbed Solution Theory (IAST)

The experimental determination of binary and ternary isotherms is often a very tedious and time-consuming task, however in order to evaluate the performance of adsorption processes this information is critical. The ideal adsorbed solution theory is a set of equations proposed by Myers and Prausnitz with which multicomponent adsorption equilibrium data can be calculated. The only data required is a single component isotherm model for each of the component gases in the mixture. The IAS theorem has been widely used and reviewed in adsorption literature for the prediction of multicomponent adsorption data in the absence of experimental data [37], [38].

The key assumptions in the IAS theorem define the mathematical expressions which result from it. The gas phase is assumed to be ideal. The first IAST equation is derived from the assumption of a Raoult's law type of relationship between the solid and gas phases. It is also assumed that there is no adsorbate-adsorbate interaction occurring in either the solid or the gas phases:

$$P_i y_i = P_i^0 x_i \tag{C.1}$$

The second equation is derived from the Gibbs isotherm and the assumption that in an ideal mixture, the surface potential or reduced spreading pressure of the mixture, $\frac{\pi A}{RT}$, is the same as the surface potential of every component in the mixture.

$$\frac{\pi A}{RT} = \int_0^{P_i^0} \frac{n_i}{P_i} dP_i \tag{C.2}$$

The total solid phase loading of all components of the mixture is then given by:

$$\frac{1}{n_T} = \sum_{i=1}^{N} \frac{x_i}{n_i^0} \tag{C.3}$$

The loading, n_i, of each component,i is then calculated:

$$n_i = x_i n_T \tag{C.4}$$

When there is no analytical solution to equation C.2, the IAST equations must be solved numerically. The solution of the IAST is solved by specifying the temperature, total pressure and gas phase composition of the mixture. An initial estimate or guess of the reduced spreading pressure for the adsorbed phase is estimated. Equation C.2 is then solved iteratively for different guesses of the hypothetical solid phase partial pressure, P_i^0, until all spreading pressures for the different components are equal. The guess of the reduced spreading pressure is then updated based on whether or not the sum of the solid mole fractions, x_i, of each component equals unity. When this sum equals unity, the IAS solution is complete.

The advantage of using the IAS theorem is that it has been widely validated for ideal mixtures in the adsorbed phase in literature. Additionally, the IAS solution agrees with experimental data at lower pressures. The disadvantage is that ideal behavior of adsorbates in the adsorbed phase is not guaranteed, such as in the case of CO_2 and water vapour on Zeolite 13X, even in the low pressure region [20]. However, the solution is computationally costly due to its iterative nature when the solution is not analytical. This means that implementation in a full PSA model is not possible in the latter case, however, the IAS solution can be compared to that of an extended model.

The solution to the IAST equation can be used to derive explicit multiple component extensions to single component isotherm models such as the Single- or Dual-site Langmuir isotherm equation, which is applicable when all components have similar saturation capacities. This form is directly applicable to Zeolite 13X and SIFSIX MOFs which are discussed in this thesis.